Universidade do Minho
Escola de Engenharia

Tânia Sofia Araújo Figueiras Ferreira

Microinjection moulding of polymeric composites with functionalized carbon nanotubes

novembro de 2013

Universidade do Minho
Escola de Engenharia

Tânia Sofia Araújo Figueiras Ferreira

Microinjection moulding of polymeric composites with functionalized carbon nanotubes

Tese de Doutoramento
Ciência e Engenharia de Polímeros e Compósitos

Trabalho efectuado sob a orientação do
Professor Doutor António José Vilela Pontes

e co-orientação
Professora Doutora Maria da Conceição de Jesus Rego Paiva

novembro de 2013

Tânia Sofia A. F. Ferreira

Universidade do Minho, Novembro de 2013

Acknowledgments

The work presented here was carried out between 2007 and 2013 in the Department of Polymer Engineering of the University of Minho.

This thesis represents an important step in achieving a professional stage, and assuredly, a challenge on a personal level as well. Like all challenges, there are always valuable contributions from several people, sometimes directly and others indirectly.

Therefore, the author would like to thank the following individuals and institutions that during this period contributed to the realization of this thesis.

I start by expressing my gratitude to my supervisors, António Pontes and Conceição Paiva for their encouragement, patience, dedication, scientific guidance, support and suggestions!

To my colleagues that worked with me along all this time and to friends with whom I shared good and less good moments. I would like to thank Rui Novais, Fátima Almeida and a childhood friend Catarina Cruz.

As a chemistry and physics teacher, to my professional colleagues and school director for their understanding, collaboration and encouragement.

Thanks also to the academic staff, researchers, technicians and administrative staff of the Department of Polymer Engineering of the University of Minho that helped me along this way, especially to the technician Mauricio Malheiro.

I hereby acknowledge Fundação para a Ciência e Tecnologia (FCT), for awarding me a PhD grant (SFRH/BD/39119/2007).

Most importantly, I want to thank my parents and sister Catarina Ferreira for their endless love, continuous encouragement, support and investment in my academic formation.

To all the people and entities that contributed to my work, but are not directly mentioned here, my sincere gratefulness and appreciation.

Publications

International Journals Publications

This doctoral thesis is based in the following papers:

Paiva MC, Simon F, Novais R, Ferreira T, Proença M, Xu W, Besenbacher F. Controlled functionalization of carbon nanotubes by a solvent-free multicomponent approach. *ASC Nano* 2010, *4* (12), 7379-7386.

Ferreira T, Paiva MC, Pontes A, Dispersion Of Carbon Nanotubes In Polyamide 6 For Microinjection Moulding, *J Polym Res* 2013, 20, 301

Ferreira T, Paiva MC, Pontes A. Microinjection Moulding of Polyamide 6 submitted to the *Journal of Applied Polymer Science*.

Ferreira T, Paiva MC, Pontes A. Crystallization Behavior of Microinjected CNT/PA 6 Nanocomposites. *In preparation*.

International Conference Proceedings Books

Oral communications

Paiva MC, Novais RM, Ferreira T, Proença MF, Simon F, Pötschke P, Besenbacher F, Xu W. Reactive carbon nanotubes for strong interfaces in polymer composites, CARBON 2010, July 10-16, 2010, Clemson, SC, USA.

Ferreira T, Paiva MC, Pontes A Functionalized Carbon Nanotubes-Polyamide Composites Produced By Microinjection Moulding VI International Materials Symposium Materiais, 2011, Guimarães, Portugal.

Ferreira T, Paiva MC, Pontes A. Functionalized Carbon Nanotubes-Polyamide Composites Produced By Microinjection Moulding, Workshop DEP, 16 May 2012, Guimarães, Portugal.

Posters

Novais RM, Ferreira T, Oliveira BA, Paiva MC, Pötschke P, Pleul D, Simon F. Chemical functionalization of carbon nanotubes by the 1,3-dipolar cycloaddition reaction: the effect of temperature. Carbon, June 14-19, 2009, Biarritz, France.

Paiva MC, Novais RM, Oliveira BA, Ferreira T, Covas JA. Polymer composites with chemically modified carbon nanotubes. Carbon, June 14-19, 2009, Biarritz, France.

Paiva MC, Novais RM, Oliveira BA, Ferreira T, Proença MF, Covas JA, Pötschke P, Pleul D, Simon F, Xu W, Besenbacher F. Chemical functionalization of carbon nanotubes for polymer composite formation. 4th International Conference on Carbon Based Nanocomposites, September 20-23, 2009, Hamburg, Germany.

Novais RM, Paiva MC, Ferreira T, Proença MF, Simon F, Pötschke P, Xu W, Besenbacher F. Reactive carbon nanotubes for strong interfaces in polymer composites. ChemonTubes, April 11-15, 2010, Arcachon, France.

Ferreira T, Paiva MC, Pontes A. Microinjection moulding of nanocomposites with modified carbon nanotubes: correlation between dispersion and electrical conductivity Trends in NanoTechnology. September 06-10, 2010, Braga, Portugal.

Ferreira T, Paiva MC, Pontes A. Statistical analysis of interface and its effect on properties of microinjection moulding nanocomposites with functionalized carbon nanotubes. Semana da Escola de Engenharia-Universidade do Minho, 2010, Guimarães, Portugal.

Ferreira T, Paiva MC, Pontes A. Analysis of agglomerate dispersion of modified carbon nanotubes in polyamide 6. III Annual Meeting I3N, February 11-12, 2011, Fátima, Portugal.

Ferreira T, Lopes PE, Pontes A, Paiva MC. Characterization of Microinjection Molded Composites of Polyamide 6 and Carbon Nanotubes, Nanocarbon Composites 2012, Valencia, Espanha.

ABSTRACT

Microinjection moulding of polymeric composites with functionalized carbon nanotubes

The unique electronic, mechanical, and structural properties of carbon nanotubes (CNT) make them suitable for applications in the fields of electronics, sensors, medical devices, aerospace and automotive industries. The preparation of CNT/polymer nanocomposites presents particular interest among the various possible applications. However, the long entangled nanotubes form agglomerates that poses serious obstacles to further development of nanocomposites with the target properties.

One of the approaches to overcome the CNT chemical inertness, enhance the compatibility with the matrix and improve homogeneous dispersion through the matrix is through its covalent functionalization. This is expected to improve the CNT interface with the polymer matrix, thus improving the mechanical properties of the nanocomposites at very low content.

One of the purposes of this thesis was to implement the covalent modification of the CNT surface using a simple functionalization method, to increase the CNT surface reactivity and possibly help their dispersion into the polyamide matrix without inducing structural damage on the CNT.

The functionalization of CNT was carried out through the 1,3-dipolar cycloaddition reaction of azomethine ylides using a solvent-free reaction route. CNT were successful functionalized with pyrrolidine groups through a simple and fast procedure that was scaled up, and may be compatible with current industrial processes.

Another objective was to disperse the CNT in polyamide 6 (PA6) using melt mixing, and to produce PA6/CNT nanocomposites by microinjection molding (μIM). Finally, the morphological and physical properties of the mouldings produced were evaluated.

The μIM process is becoming of greater importance for the manufacturing of polymeric micro-components considering its low cost and short cycle times, useful for mass production.

The as-received and functionalized CNT were dispersed in PA6 at various contents (1, 1.5, 3 and 4.5 w.%) by twin-screw extrusion and then processed by μIM. The same procedure was carried out for PA6 without CNT.

To study the influence of the specific thermo-mechanical conditions generated during μIM, the morphology and structure of PA6 and PA6/CNT samples produced by melt extrusion and μIM

were compared. The specimens of PA6 and PA6/CNT nanocomposites were analyzed by polarized light microscopy, differential scanning calorimetry, and wide-angle X-ray diffraction.

The effect of the processing method upon the development of crystallinity in PA6 and PA6/CNT samples was studied. The contribution of the two crystalline phases, α and γ, on the PA6 with and without CNT was measured. The degree of crystallinity of the μIM PA6 sample was lower compared to the extruded material, and was not affected by the CNT content.

The μIM samples of PA6 presented a considerable molecular orientation at the skin region that decreased towards the sample core, with larger contribution of γ-phase compared to extruded samples. The orientation exhibited by μIM parts of PA6, mainly at the skin region, is not detectable after CNT addition.

The dispersion of the CNT agglomerates was quantified in all PA6/CNT samples using optical microscopy and image analysis. The effect of functionalization on the PA6/CNT interface, the nanocomposite morphology and the mechanical and electrical properties were studied. It was observed that the microinjected composites with functionalized CNT presented improved dispersion, with smaller CNT agglomerate area ratio compared to the composites with pure nanotubes. The functionalized nanotubes showed better adhesion to PA6 compared to pure nanotubes, as observed by scanning electron microscopy. The incorporation of CNT considerably improved the mechanical properties. The effect of high shear rate of the polymer melt on carbon nanotube alignment during μIM was assessed by comparing the electrical resistivity of the composite after extrusion and after μIM, through the thickness and along the flow direction. The experiments showed that the moulding geometry design and processing conditions significantly affected electrical resistivity.

This thesis provides an insight into the joint effect of CNT chemical functionalization and the specific conditions of μIM on PA6 morphology and on CNT dispersion, and its influence on the electrical, mechanical and thermal properties of the resulting composites.

RESUMO

Microinjecção de compósitos poliméricos com nanotubos de carbono funcionalizados

A descoberta dos nanotubos de carbono (CNT) e as perspetivas de desenvolvimento de novos nanomateriais à base de carbono têm entusiasmado a comunidade científica nas últimas décadas. As propriedades eletrónicas, mecânicas e estruturais únicas dos CNT permitem aplicações nas áreas de eletrónica, sensores, indústria médica, aeroespacial e automóvel. Grande parte destas aplicações necessitam da preparação de nanocompósitos de CNT/polímero para as tornar possíveis. No entanto, os longos nanotubos tendem a enrolar e a formar aglomerados que são um obstáculo ao desenvolvimento de nanocompósitos homogéneos e com excelentes propriedades.

Uma das abordagens para superar a inércia química dos CNT, aumentar a compatibilidade com a matriz e possivelmente melhorar a dispersão na matriz é a funcionalização covalente dos CNT. Espera-se desta forma melhorar a dispersão e as propriedades físico-mecânicas e térmicas dos nanocompósitos com baixas quantidades de CNT.

Um dos objetivos desta tese foi implementar um método de funcionalização que aumentasse a reatividade da superfície dos CNT e ajudasse a sua dispersão na matriz de poliamida sem induzir danos estruturais nos CNT. A funcionalização dos CNT foi realizada por meio de reação de cicloadição dipolar 1,3 de iletos de azometina utilizando um método sem utilização de solventes.

Os CNT foram funcionalizados com grupos pirrolidina através de um procedimento simples e rápido, que foi desenvolvido a maior escala, mostrando potencial para ser compatível com processos industriais correntes.

Outro objetivo foi produzir nanocompósitos de poliamida 6 (PA6) com CNT por moldação por microinjeção (μIM) e estudar a morfologia e as propriedades físicas das moldações obtidas.

Este processo tem-se mostrado de grande importância para a fabricação de micro-componentes poliméricos, considerando o baixo custo e os ciclos de tempo curtos que apresentam, úteis para a produção em massa.

Os CNT tal como recebidos e funcionalizados foram dispersos em várias concentrações na PA6, extrudidos e depois processados por μIM. O mesmo procedimento foi realizado para a PA6 sem CNT.

Para estudar a influência das condições termo-mecânicas específicas geradas durante a μIM, comparou-se a morfologia e a estrutura das amostras de PA6 e PA6/CNT produzidas por extrusão e μIM.

Amostras dos provetes de PA6 e PA6/CNT nanocompósitos foram analisados por microscopia de luz polarizada, calorimetria diferencial de varrimento e difração de raios-X a altos ângulos.

Nas amostras de PA6 e PA6/CNT preparadas por ambos os métodos encontraram-se duas fases, α e γ. A cristalinidade dos nanocompósitos de PA6/CNT deve-se maioritariamente à fase α. O grau de cristalinidade das amostras μIM de PA6 é inferior comparado com o das extrudidas e não é afetado pela adição de CNT.

As amostras moldadas por microinjeção apresentavam uma orientação considerável na região da pele que diminui em direção ao núcleo, com maior contribuição da fase γ em comparação com as amostras extrudidas. A orientação exibida pelas amostras de PA6 moldadas por microinjeção, maioritariamente na região da pela, não é detetável após a adição de CNT.

A dispersão dos aglomerados de CNT foi quantificada em todas as amostras de PA6/CNT por microscopia ótica e análise de imagem. O efeito da funcionalização na interface PA6/CNT, a morfologia dos nanocompósitos e as propriedades mecânicas e elétricas foram estudadas. Observou-se que os compósitos microinjectados com CNT funcionalizados apresentam melhor dispersão, com menor proporção de aglomerado de CNT por área em comparação com os compósitos com nanotubos puros. Os nanotubos funcionalizados apresentam melhor adesão à PA6 em comparação com nanotubos puros, como observado por microscopia eletrónica de varrimento. A incorporação de CNT melhorou consideravelmente as propriedades mecânicas. O efeito da elevada taxa de corte do polímero sobre o alinhamento de CNT durante μIM foi avaliado comparando a resistividade elétrica do compósito após a extrusão e depois de μIM, através da espessura e ao longo da direção do fluxo. Os resultados mostraram que o desenho do molde e as condições de processamento afetam significativamente a resistividade elétrica.

Esta tese fornece uma compreensão sobre o efeito conjunto da funcionalização química dos CNT e das condições específicas de μIM na morfologia da PA6, na dispersão dos CNT em PA6, e na sua influência sobre as propriedades elétricas, mecânicas e térmicas dos compósitos resultantes.

Table of Contents

Acknowledgments iii
Publications v
ABSTRACT vii
RESUMO ix
Table of Contents xi
List of Figures xv
List of Tables xxi
List of Abbreviations and Symbols xxiii

1. INTRODUCTION 1
1.1. Context 1
1.2. Motivation 2
1.3. Thesis outline 3

2. STATE OF THE ART 5
2.1. Carbon nanotubes 6
2.1.1. Properties of carbon nanotubes 7
2.1.2. Applications of carbon nanotubes 11
2.2. Chemical functionalization of carbon nanotubes 12
2.2.1. Covalent functionalization 12
2.2.2. Non-Covalent functionalization 15
2.3. Composite processing 17
2.3.1. In-situ polymerization 17
2.3.2. Solution processing of composites 18
2.3.3. Melt mixing 19
2.3.4. Microinjection molding 21
2.3.4.1. μIM process 22
2.3.4.2. Microinjection equipment 24
2.3.4.3. Applications 25
2.4. Physical properties of polymer/carbon nanotubes nanocomposites 27
2.4.1. Electrical properties 27
2.4.2. Mechanical properties 29
2.4.3. Thermal properties 32

2.5. Dispersion of carbon nanotubes in polymers 32
2.5.1. Direct methods 32
2.5.2. Indirect methods 35
2.5.3. CNT dispersion mechanism 36
2.5.4. Influence of processing method 38
2.5.5. Carbon nanotube reaglomeration 39
2.5.6. Influence of injection and microinjection molding on the CNT dispersion 41
2.5.6.1. CNT orientation 41
2.5.6.2. Correlation between μIM and electrical conductivity 42
2.5.7. Influence of nanotube material and polymer type 45
3. CHEMICAL FUNCTIONALIZATION OF CARBON NANOTUBES 47
3.1. Introduction 48
3.2. Experimental section 49
3.2.1. Materials and functionalization method. 49
3.2.2. Carbon nanotube analysis. 49
3.3. Results and discussion 50
3.3.1. The 1,3-dipolar cycloaddition reaction 50
3.3.2. Carbon nanotube surface analysis. 52
3.3.3. Weight loss analysis. 57
3.3.4. Influence of the reaction conditions on surface chemistry. 59
3.4. Conclusions 61
4. MICROINJECTION MOULDING OF POLYAMIDE 6 63
4.1. Introduction 64
4.2. Experimental Section 65
4.2.1. Materials and Sample Preparation 65
4.2.2. Characterization 66
4.2.2.1. Optical Microscopy 66
4.2.2.2. Differential Scanning Calorimetry 66
4.2.2.3. Wide Angle X-ray Diffraction 66
4.3. Results and Discussion 67
4.4. Conclusions 73
5. CRYSTALLIZATION BEHAVIOR OF MICROINJECTED CARBON NANOTUBES/ POLYAMIDE 6 NANOCOMPOSITES 75
5.1. Introduction 76

5.2. Experimental section 77
5.2.1. Materials and sample preparation 77
5.2.2. Composite characterization 78
5.2.2.1. Morphology 78
5.2.2.2. Differential scanning calorimetry 78
5.2.2.3. Wide angle X-ray diffraction 78
5.3. Results and Discussion 79
5.3.1. Dispersion of CNT in PA6 79
5.3.2. Differential scanning calorimetry 79
5.3.3. Wide angle X-ray diffraction 84
5.4. Conclusion 88
6. DISPERSION OF CNT IN PA6 FOR MICROINJECTION MOULDING 89
6.1. Introduction 90
6.2. Experimental section 92
6.2.1. Carbon nanotube functionalization and characterization 92
6.2.2. Preparation of carbon nanotube/polyamide 6 composites 92
6.2.3. Composite characterization 93
6.2.3.1. Morphology 93
6.2.3.2. Electrical resistivity 94
6.2.3.3. Mechanical properties 94
6.3. Results and Discussion 95
6.3.1. CNT functionalization and characterization 95
6.3.2. Study of carbon nanotube dispersion 97
6.3.3. Electrical properties 101
6.3.4. Mechanical properties 103
6.4. Conclusions 105
7. CONCLUSIONS 107
REFERENCES 109

List of Figures

Figure 2.1 - Scanning electron micrographs of (a) aligned CNT and (b) HiPCO CNT produced by CVD methods [2].....6

Figure 2.2 - TEM micrographs of MWNT. A cross-section of each CNT illustrates the different sheets number (n) and outer diameter (d). a) n=5, d=6.7 nm b) n=2, d=5.5 nm and c) n=7, d=6.5 nm [7].....7

Figure 2.3 - Comparison of diameters of various fibrous carbon-based materials [2].....8

Figure 2.4 – TEM micrograph showing the lateral packing of 1.4-nm-diameter SWNT in a bundle where the tube-tube distance is 0,315 nm (A) [10]. Conceptual diagram of SWNT (B) and MWNT (C) showing typical dimensions of length, width and separation distance between graphene layers in MWNT (adapted from [11]).....8

Figure 2.5 - A Stone–Wales defect on the sidewall of a nanotube leads to a local deformation of the graphitic sidewall and thereby introduces an increased curvature in this region [16].....9

Figure 2.6 - A) HREM image of kink structures formed in nanotubes under mechanical duress and B) computer simulation of nanotube buckling [27].....11

Figure 2.7 - 1,3 - Dipolar addition of azomethine ylides to SWNT and MWNT [47].....14

Figure 2.8 - Schematics of CNT functionalization using non-covalent methods (A: polymer wrapping; B: surfactant adsorption; C: endohedral method) [50].....15

Figure 2.9 - MWNT (left) and MWNTCOOH (right) in the master solution of polyamide 6 after stored for 24h. There is no evidence of phase separation or precipitation [91].....18

Figure 2.10 - Schematic representation of the prototype modular co-rotating twin screw extruder [104].....20

Figure 2.11 - Typical stages involved in microinjection molding: (a) mold closing, (b) injection and holding, (c) cooling and plastication, (d) mold opening and part ejection [122].....23

Figure 2.12 – Typical batch of micro structures as it comes from an injection-molding machine [116].....24

Figure 2.13 - Boy 12A [132].....25

Figure 2.14 - Comparison of dimensions between screw and injection plungers for μIM (left) and a screw for conventional injection molding (right) [113].....25

Figure 2.15 - Example of a micro-molded part: A - micro-gear; B - macro-part with a micro-structured region (DVD disc) [113] C - cell chip LILLIPUT made by injection molding [140].....26

Figure 2.16 - Examples of microparts with weight in the range of milligrams [141]. 26
Figure 2.17 - Schematic of percolation phenomenon and conducting network in conducting composites [50].....28
Figure 2.18 – Schematic sketches show the effect of 1D filler on the conductivity of polymer composite [149].....28
Figure 2.19 - (A) Typical stress-strain curves. (B) Tensile stress (at yield) and tensile modulus for PA6 and its nanocomposites as a function of MWNT concentration [163].....31
Figure 2.20 - A - SEM image showing microcracks linked by stretched nanotubes in PA6 nanocomposites. B - CNT sheathed with polymer in PA6 nanocomposites [163].....31
Figure 2.21 – Comparison of length distributions of Nanocyl™ NC7000: before (pristine MWNT) and after processing (as recovered from an extruded PC composite with 2 wt% CNT), including TEM images of processed NC7000 presented on the right-hand side [180].....34
Figure 2.22 - Online conductance, macrodispersion index, at the top OM images and at the bottom AFM-images of CNT-rubber nanocomposites. Samples taken at 13 min (a), 32 min (b) and 90 min (c) [172].....35
Figure 2.23 - Schematic descriptions of MWNT agglomerate dispersion mechanisms [174].....37
Figure 2.24 - Illustration of rupture and erosion mechanism (dotted lines indicates region of crack propagation) [174].....37
Figure 2.25 - Time dependent DC conductivity of CNT/epoxy suspensions containing 0.1 wt % MWNT at 70 °C at a steady shear rate of 0.5 s^{-1} for two samples with initially dispersed (▲) and agglomerated (△) nanotubes. The inserts show optical micrographs of the initially and final states for both samples [199].....40
Figure 2.26 - 2D WAXD patterns for two samples: A - the shear layer of macropart; B - the core layer of macropart; C - the μpart. The flow direction is vertical. The orientation parameter was estimated from azimuthal WAXD pattern of (040) reflection. Adapted from [208].....42
Figure 2.27 - Effect of polymer processing conditions on electrical conductivity and percolation threshold of the PP/MWNT (filled symbols) and PC/MWNT (open symbols) nanocomposites [206].....44
Figure 2.28 - Area ratio of remaining initial CNT agglomerates (A_A) versus interfacial energy between nanotubes and polymer to study the effect of polymer matrix type on dispersion (dashed line is for guiding eyes) [225].....45
Figure 3.1 - Functionalization of the CNT surface by the 1,3-dipolar cycloaddition reaction of azomethine ylides. 51

Figure 3.2 - CNT showing evidence of chemical functionalization of the nanotube wall, obtained by ambient STM, scanning condition: It= -1.21 nA, Vt= -831 mV. 52
Figure 3.3 - Wide-scan, C 1s and N 1s XPS spectra of an untreated CNT sample (a) and CNT samples after carrying out the DCA reaction at 180 °C for 3 h (b) and at 230 °C for 12 h (c). The abbreviation O KLL designates the oxygen Auger peaks. 53
Figure 3.4 - SEM images of CNT functionalized at 230 °C obtained with secondary electrons (a) and backscattered electrons (b). The area Z1 was analyzed by EDAX (c). 54
Figure 3.5 - High-resolution C 1s XPS spectra of an untreated CNT sample (a) and CNT samples functionalized at 180 °C for 3 h (b) and at 230 °C for 12 h (c). The intensities of all spectra were normalized using component peak A as reference. In order to visualize the component and shake-up peaks, component peaks A are shown as cut-out. The abbreviations are explained in the text. 55
Figure 3.6 - High-resolution N 1s XPS spectra of an untreated CNT sample (a) and CNT samples functionalized at 180 °C for 3 h (b), 230 °C for 3 h (c), 230 °C for 9h (d), and 230 °C for 12h (e). ..56
Figure 3.7 - Graphic representation of the weight loss variation with reaction time and temperature, measured by TGA and estimated from XPS results. 58
Figure 3.8 - Variation of the total N bonded to the CNT surface with reaction temperature. 59
Figure 3.9 - Concentration of the CNT functional groups under different reaction conditions. 60
Figure 4.1 - Nominal dimensions of tensile μIM specimens. 66
Figure 4.2 - Schematic representation of the samples prepared for WAXD analysis: samples cut from μIM specimens formed by a) the entire thickness and b) the core region, and c) samples cut from the extruded filament. The arrows represent the direction of the X-ray beam. 67
Figure 4.3 - Optical micrographs obtained by PLM for polymer sections along the flow direction for extruded and μIM parts both with the central region at relative higher magnification. 68
Figure 4.4 - DSC thermograms of extruded (light lines) and μIM (dark lines) PA6; A) first heating and B) cooling and second heating. 69
Figure 4.5 - WAXD patterns of extruded and μIM parts. For the scattering patterns, the flow direction corresponds to the perpendicular direction to the page. 71
Figure 4.6 - Crystallinity and α and γ-phase content data obtained from fitting of WAXD patterns of extruded and μ-parts. 72
Figure 5.1 - SEM micrographs of the composites with 1% and 4,5 wt.% of p-CNT and f-CNT (designed as P1, F1, P4.5 and F4.5) obtained for extruded samples and μIM tensile specimens. All the SEM images have the same scale as the first. 80

Figure 5.2 - DSC first heating curves of PA6 and PA6 with various content of p-CNT and f-CNT for A) - extruded and B) μIM nanocomposites.....82
Figure 5.3 - DSC cooling curves of PA6 and PA6 with p-CNT and f-CNT for A) – extruded and B) - μIM nanocomposites.....83
Figure 5.4 -DSC second heating curves of PA6 and PA6 with p-CNT and f-CNT for A) – extruded and B) - μIM nanocomposites.....83
Figure 5.5 - WAXD patterns of μP. For the scattering patterns, the flow direction corresponds to the perpendicular direction to the page.....84
Figure 5.6 - Integrated intensity profiles of the μIP samples.....85
Figure 5.7 – Crystallinity and α and γ-phase content data obtained from fitting of WAXD patterns of μ-parts. 86
Figure 5.8 - Crystallinity and α and γ-phase content data obtained from fitting of WAXD patterns of core from μparts.....86
Figure 5.9 - Crystallinity and α and γ-phase content data obtained from fitting of WAXD patterns of extruded samples.....87
Figure 6.1 - Nominal dimensions of tensile (A) and parallelepipedic (B) specimens. 93
Figure 6.2 - Functionalization of the CNT surface using the 1,3-dipolar cycloaddition reaction. 95
Figure 6.3 - Thermogravimetric analysis plots for as received and functionalized CNT, and the TGA curve derivative. 96
Figure 6.4 - SEM micrographs of as received (A and C) and functionalized (B and D) CNT. 96
Figure 6.5 - A to D represent the cumulative area ratio for the composites prepared by extrusion (dashed line) and μIM tensile (continuous line); E compares the cumulative area ratio for the composites obtained from μIM tensile (continuous line) and parallelepipedic specimens (dotted line). .98
Figure 6.6 - Total agglomerate area ratios obtained for the composites with different CNT content. 99
Figure 6.7 - OM (left) and SEM (right) micrographs of the composites with 4.5 wt.% CNT, obtained after extrusion and μIM (for tensile and parallelepipedic specimens). OM illustrates the influence of μIM on the CNT agglomerate size and shape. SEM micrographs show the CNT dispersed fraction, presenting an insert with a higher magnification image. All the SEM images have the same scale as the first. ... 100
Figure 6.8 - Electrical resistivity of the composites prepared by the different processing methods and with different μIM molds. 103
Figure 6.9 - Typical stress-strain curves obtained for PA6 and PA6/CNT composites. 103

Figure 6.10 -Tensile strength (A) and strain to failure (B) of μIM tensile-shaped specimens of PA6 and PA6/CNT samples with p-CNT and f-CNT. 104
Figure 6.11 - Young's moduli variation for PA6/CNT composites relative to the neat polymer. 105

List of Tables

Table 2.1 - Typical properties of CNT [26]. 10
Table 2.2 – Properties of the different CNT products. 11
Table 2.3 – Advantages and disvantages of various functionalization methods [50].....16
Table 2.4 - Summary of experimental parameters and conductivity results for polymer/CNT composites 29
Table 3.1 - N and O elemental ratios obtained by XPS, and weight loss results measured by TGA and estimated from the XPS data. 57
Table 4.1 - Crystallization and melting parameters of extruded and μIM PA6 parts.....70
Table 4.2 - Hermans orientation factors calculated for μP and extruded PA6 samples.....73
Table 5.1 - Crystallization and melting parameters of extruded and μIM PA6 and its nanocomposites..81
Table 5. 2 - Hermans orientation factors calculated for μP and extruded PA6 samples. 87
Table 6.1 - Nitrogen and oxygen atomic composition of CNT obtained by XPS and weight loss results measured by TGA. 95
Table 6.2 - Optical microscopy and electrical resistivity characterization of the composites with 4.5% p-CNT and f-CNT..... 101

List of Abbreviations and Symbols

Abbreviations

A - Total agglomerate area

A_0 - Total area analysed

Al - Auminium

AFM - Atomic force microscopy

A_R - Area ratio

at% - Atomic percentage

BE - Binding energy

C60 - Buckminsterfullerene

CB - Carbon black

CNT - Carbon nanotube

CNT210 - Carbon nanotube functionalized by 1,3-dipolar cycloaddition at 210 °C

CNT250 - Carbon nanotube functionalized by 1,3-dipolar cycloaddition at 250 °C

CVD - Chemical vapor deposition

D - Macrodispersion index

d - Diameter

DA - Diels-Alder

DC - Direct current

DCA - Dipolar cycloaddition

DMF - Dimethyl formamide

f – Effective volume of the filler

EDAX - Energy dispersive X-ray analysis

Fa - Fragmentation number

f-CNT - Functionalized carbon nanotubes

f_z – Hermans orientation factor

ΔH_f - heat of fusion

HNO_3 - Nitric acid

HipCO – high pressure carbon monoxide

HRTEM - High-resolution transmission electron microscopy

H_2SO_4 - Sulfuric acid

IM – injection molding

It - Tunneling intensity

L/D - Length to diameter ratio

LDPE - Low density polyethylene

μIM – microinjection molding

μP - microparts

MFI - Melt flow index

MWNT - Multi-walled carbon nanotubes

N_2 - Nitrogen

OH - Hydroxyl

PA - Polyamide

PC - Polycarbonate

PE – Polyetilene

p-CNT – as received carbon nanotubes

PP - Polypropylene

PS - Polystyrene

Pt - Platinum

SDS - Sodium dodecyl sulfate

SEM - Scanning electron microscopy

STM - Scanning tunneling microscopy

SME- specific mechanical energy

SWNT - Single-walled carbon nanotubes

T - Temperature

T_c – crystallization temperature

TEM - Transmission electron micrograph

TGA - Thermogravimetric analysis

T_{m1} - first heating temperature

T_{m2} - second heating temperature

vol% - Volume percentage

w% - Weight percentage

XPS - X-ray photoelectron spectroscopy

Z-Gly-OH - N-benzyloxycarbonylglycine

θ - Chiral angle

χ_c - Degree of crystallinity

φ - Volume frcation

Units

A/cm^2 - Ampere per square centimeter

eV - Electron volt

GPa - Gigapascal

g/h - Grams per hour

g/cm^3 - Gram per cubic centimeter

h - Hour

K - Kelvin

Kg - Kilogram

Kg/mol - Kilogram per mole

kV - Kilovolt

M - Mole per liter

mg - Milligram

mL - Milliliter

mm - Millimeter

mm/min - Millimeter per minute

mV - Millivolt

MPa - Megapascal

nA - Nanoampere

nm - Nanometer

rpm - Rotations per minute

s - Second

TPa - Terapascal

W - Watt

W/mK - Watt per meter per Kelvin

wt% - Weight percentage

Å - Ångström

°C - Celsius Degree

°C/min - Celsius Degree per minute

μm – Micrometer

μL – Microliter

Ω cm - Ohm centimeter

1. INTRODUCTION

1.1. Context

Important advances in nanoscience and nanotechnology have been strongly motivated by the discovery of a variety of carbon nanostructures, since the later half of twentieth century.

Carbon, the sixth element in the periodic table, has received immense attention from the era of the discovery of fullerene (1985) and of carbon nanotubes (1991). Thus carbon nanotubes (CNT) hold their position as the strongest and the most promising material in the development of nanotechnology.

CNT possess high flexibility, large aspect ratio (typically >1000), low mass density and indicate extremely high tensile modulus and strengths.

Thus, the combination of mechanical and electrical properties of CNT, the low content of CNT required and cost-effective composites that can be fabricated represent important advantages comparing with commonly used fillers such as carbon black or carbon fibers. The above, makes CNT the ideal reinforcing agents in conductive and high strength composites.

An important prerequisite for the production of CNT/polymer nanocomposites is the efficient dispersion of individual CNT through the polymer matrix and the establishment of a strong chemical affinity (covalent or non-covalent) with the surrounding polymer matrix. Various methods of CNT chemical modification have been proved quite successful.

In polymer nanocomposites area, to replicate microstructured parts in industry field, microinjection molding (μIM) is one of the most suitable and cheap process, with high precision among a variety of polymer processing methods. So it is a promising technology with application in the areas of biotechnology, as components of optical systems, as microgears, in microfluidics, medical technology and electronics. The microsystems technology has shown annual growth rates of ~15% in recent years.

1.2. Motivation

The discovery of CNT, their unique electronic, mechanical, and structural properties and the prospect of developing novel carbon-based nanomaterials has excited interest among researchers worldwide.

Besides CNT having been considered as ideal reinforcing filler in polymer composites, the inherently difficult handling of CNT poses serious obstacles to their further nanotechnology applications.

Chemical modification of CNT, a very actively discussed topic, is an effective way to prevent CNT aggregation and to achieve strong interfacial interactions with the polymer, which helps to better disperse and improve the load transfer across the CNT-polymer matrix interface. Nevertheless, the effects of the functionalization type on the mechanical and electrical properties of composites produced are under investigation.

In this thesis, the CNT surface is modified through a nonaggressive approach using different temperature and time for the functionalization reaction, 1,3-dipolar cycloaddition. The type and the quantity of each functional group were achieved in other to optimize the best reaction conditions.

Considering the work published, the functionalization should improve the CNT dispersion through the polymer matrix and will improve the mechanical, electrical and thermal properties of the nanocomposite.

From an industrial point of view, it is necessary a fast and cost-effective technique to mold CNT/polymer composites. The increasing demand for small and even micro scale parts and the trend towards miniaturization makes μIM a technique of growing importance in this field.

In spite of this, the special thermo-mechanical conditions of μIM will afect morphological features of microparts that may strongly differ from those prepared by conventional injection molding resulting in specific physical properties which are other point of relevant interest that it is not well understood yet.

It is also relevant to understand the effect of CNT addition on polymer matrix, a semicrystalline matrix such as polyamide 6. Some reports referred CNT as nucleating agents, but additional knowledge concerning the effect of CNT amount, funcionalization and μIM in polyamide 6 cristallinity are necessary.

Moreover, the effect of surface modification on dispersion, the mechanical and electrical properties of the resultant nanocomposites with as-received and functionalized CNTs will be explored.

The knowledge acquired from this work may be useful for the industrial production of CNT/polymer composites, through microinjection molding, with enhanced mechanical and electrical properties.

1.3. Thesis outline

This thesis is divided in seven Chapters:

Chapter 1 presents the motivation of the present work, as well as the thesis outline.

Chapter 2 focus on carbon nanotube properties, applications and synthesis. An overview of the different functionalization methods and various mixing methods for producing CNT/polymer composites will be given. Microinjection molding is described with more relevance. A detailed analysis on CNT dispersion in the polymer matrix is also included. Finally, the physical properties of CNT/polymer nanocomposites are referred.

Chapter 3 includes a detailed investigation concerning the functionalization reaction implemented. Carbon nanotubes were functionalized using a solvent-free chemical procedure. The effect of temperature on the reaction was studied based on a detailed chemical analysis of the CNT surface by XPS. The surface morphology was assessed.

The **chapter 4** will present a detailed study about the effect of microinjection molding, firstly on the properties of and then on the amount of polyamide 6 crystalline forms.

Chapter 5 will refer to the effect of CNT contents into the polymer matrix. The influence of functionalization in polyamide 6 was also assessed.

Chapter 6 describes the effect of functionalization, extrusion and microinjection molding on the carbon nanotube dispersion in the polyamide. The dispersion of the nanotube agglomerates was quantified and nanotube/polymer interface was analyzed. The effect of microinjection molding on the electrical properties of the resulting composites were studied and compared to the extruded composites. Besides that, the influence of functionalization on the mechanical properties of the composite was also assessed.

In **chapter 7** general conclusions regarding the CNT functionalization and the effect of microinjection molding are drawn.

2. STATE OF THE ART

This chapter presents an overview of the morphology, properties and applications of CNT. The chemical functionalization methods for nanotubes will be reviewed.

Then, the melt processing methods for preparation of CNT/polymer composites including microinjection molding will be described.

The final section of this chapter will focus on the analysis of CNT dispersion in polymer nanocomposites, and the properties of the nanocomposites produced by melt-mixing methods.

2.1. Carbon nanotubes

Carbon nanotubes (CNT) represent an exciting research area in modern science. These molecular-scale carbon tubes are the stiffest and strongest fibers known, with remarkable physical properties and low density. These properties suggest that CNT are the ideal candidates for high performance polymer composites, with a wide range of potential applications.

Today they are widely recognized as the essential contributors to nanotechnology and, consequently, the development of a new re-thinking about physics and chemistry.

The discovery of CNT and their potential encourage the development of a variety of synthesis methods to produce CNT including: arc-discharged, laser ablation, chemical vapor deposition (CVD) and high pressure carbon monoxide (HiPCO).

The carbon arc discharge [1, 2] and the laser ablation [3] methods usually work on the gram scale and are, therefore, are relatively expensive.

For the use of nanotubes in composites, large quantities of nanotubes are required at low cost, ideally without the requirement for complicated purification.

Until now, CVD is the most commercially attractive method to produce CNT for composite work (Figure 2.1), both in academia and in industry [4, 5].

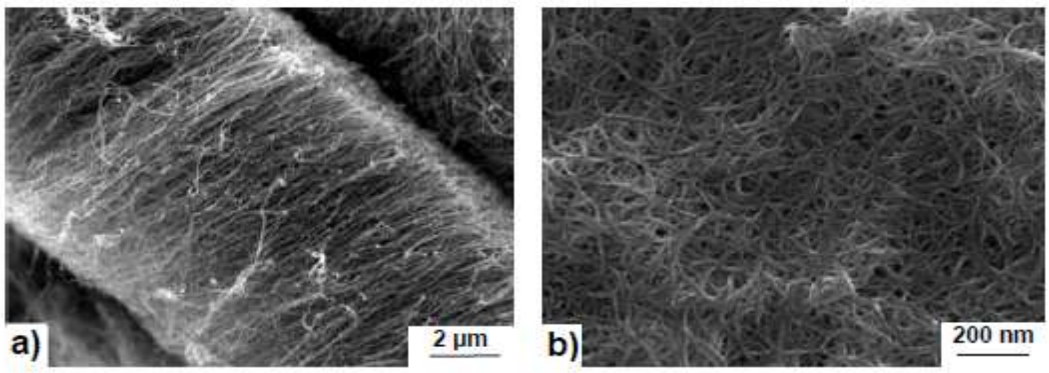

Figure 2.1 - Scanning electron micrographs of (a) aligned CNT and (b) HiPCO CNT produced by CVD methods [2].

Although a number of commercial CVD routes exist, the HiPCO process has received particular attention [6].

Since recent years, tremendous progresses have been made such as kilogram of CNT can be produced per day at very low cost using standard laboratory equipments.

2.1.1. Properties of carbon nanotubes

The synthesis of carbon structures in the form of C_{60} and other fullerenes has stimulated intense interest in the structures based on graphitic carbon sheets. In 1991, using an arc-discharge method similar to that used for fullerene synthesis, Sumio Ijima [1] produced needle structures in tubular form. TEM observations (Figure 2.2) reveal that each needle comprises coaxial tubes of graphitic sheets, ranging from 2 up to about 50, called multi-walled carbon nanotubes (MWNT), with different outer diameters. On each tube, carbon atom hexagons are arranged in helical about the needle axis.

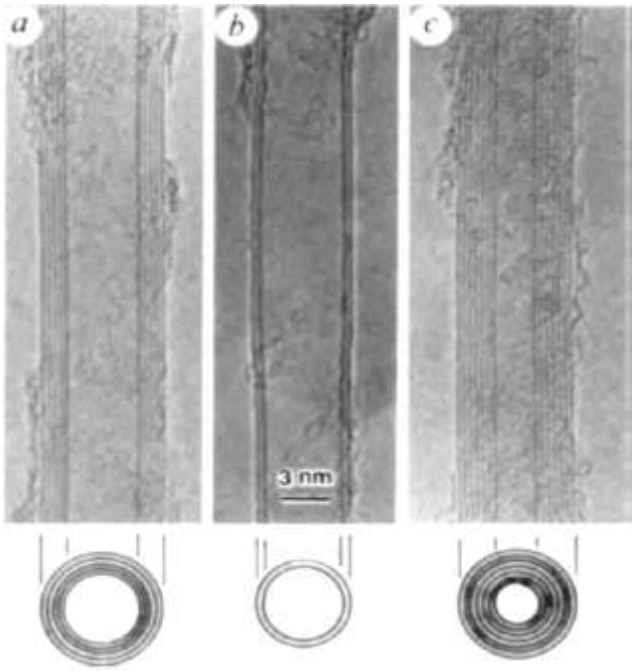

Figure 2.2 - TEM micrographs of MWNT. A cross-section of each CNT illustrates the different sheets number (n) and outer diameter (d). a) n=5, d=6.7 nm b) n=2, d=5.5 nm and c) n=7, d=6.5 nm [7].

Two years later, with the same arc process, a single carbon atoms layer rolled in a tube was synthesized [7] and with cobalt catalysis [8] and consequently called single-walled carbon nanotubes (SWNT) with diameters of one nanometer.

In generally, CNT consist of graphitic sheets, which have been rolled up into a cylindrical shape. As-grown, each nanotube is closed at both ends by a hemispherical cap formed by the replacement of hexagons with pentagons in the graphite sheet which induces curvature. Each nanotube is a single molecule where carbon atoms are covalently bonded with sp^2 hybridization.

CNT have typical diameters in the range of 1–50 nm and lengths of many microns. In contrast, commercial carbon fibers are typically in the 7-20 μm diameter range as summarized in Figure 2.3.

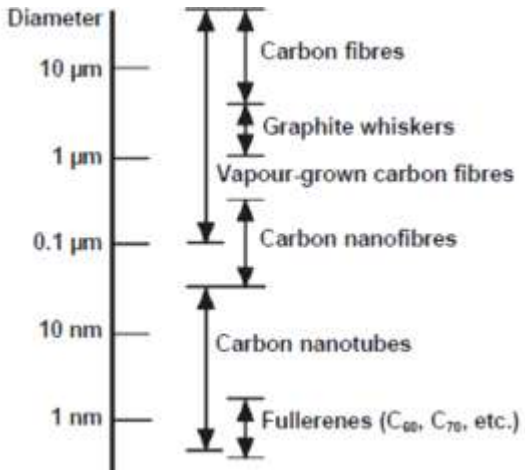

Figure 2.3 - Comparison of diameters of various fibrous carbon-based materials [2].

There are two main kinds of nanotubes: single-walled nanotubes (SWNT) or multi-walled nanotubes (MWNT). SWNT are formed by a two-dimensional hexagonal lattice of a single graphite sheet onto the surface of a cylinder of ~0,4-3 nm in diameter [9] and can be up to a few micrometers long, which are actually a single molecule and are often curved rather than straight. Although SWNT are usually obtained in the form of bundles or ropes (Figure 2.4 A and B) due to Van der Waals interactions [10]. MWNT consists of two or more concentric cylinders, each rolled out of single sheets separated by approximately the interlayer spacing in graphite, 0,34 nm, where weak Waals forces bind the tubes together. The outer diameter of such MWNT can vary from 1,4 to 100 nm [9] (Figure 2.4 C).

With this dimensions, CNT present a very high length to diameter ratio (L/D), in the order of 1000, so they can be considered as nearly on-dimensional structure.

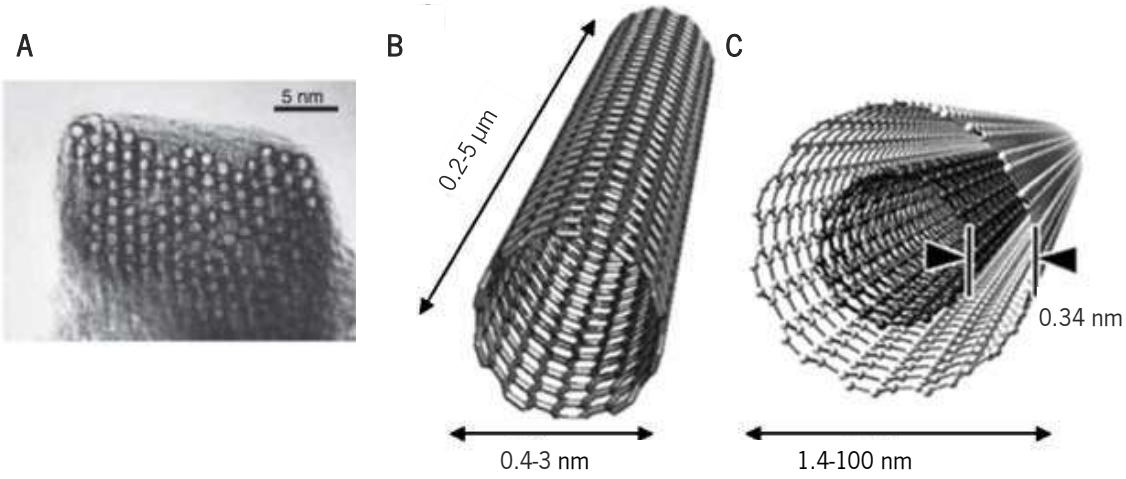

Figure 2.4 – TEM micrograph showing the lateral packing of 1.4-nm-diameter SWNT in a bundle where the tube-tube distance is 0,315 nm (A) [10]. Conceptual diagram of SWNT (B) and MWNT (C) showing typical dimensions of length, width and separation distance between graphene layers in MWNT (adapted from [11]).

In SWNT, the graphite sheet may be rolled in different orientations along any two-dimensional lattice vector (m,n). The orientation of the graphite lattice relative to the axis defines the chirality or helicity of the nanotube that can be classify as armchair ($n=m$), zigzag ($n=0$ or $m=0$) or has chiral ($m\neq n$) [12]. Depending on the direction in which the graphite sheet is rolled, SWNT may be either semiconductor or metallic [13]. For MWNT, since interlayer interactions appear to be weak, the overall behavior is determined by the electronic properties of the external shell as indicated by theoretical studies for double wall nanotubes [14].

However, nanotubes are not perfect structures, but rather contain defects formed during synthesis. It is frequently encountered a type of defect comprised of two pairs of five-membered and seven-membered rings, referred as a 7-5-5-7 defect, called Stone–Wales defect, that contain around 1–3% of the carbon atoms of a nanotube (Figure 2.5). This defect site constitutes the onset of the possible plastic deformation of a CNT [15] and may also change the lattice orientation, helicity and thus modifying the electrical properties. This extraordinary behavior could lead to an unique application: a nanodiode [16].

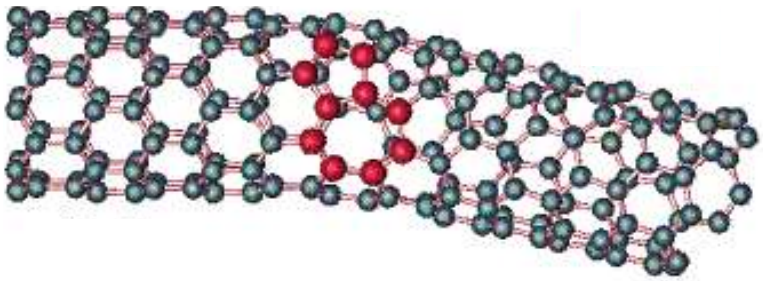

Figure 2.5 - A Stone–Wales defect on the sidewall of a nanotube leads to a local deformation of the graphitic sidewall and thereby introduces an increased curvature in this region [16].

CNT possess extraordinary properties which has attracted a special attention among scientific community.

Metallic CNT have ballistic transport, carrying current with essentially no resistance over long nanotube lengths. The conductivity for metallic nanotubes is about 10^5 to 10^6 S/m and for semiconducting tubes about 10 S/m. Electrical conductivity of SWNT [17] has been reported to range between 1×10^4 and 3×10^6 S/m depending on sample type and entanglement state and for MWNT [18] can vary between 20 and 2×10^7 S/m depending on the helicities of the outer shell, diameter and the presence of defects [19]. Thus the electric current carrying capacity is about 1000 times higher than copper wires.

Relative to thermal properties, the thermal conductivities of CNT are highly anisotropic, reaching 3000 W/(m·K) over the length of the MWNT tube [20], greater than diamond (2000 W/m·K) but insulating in the transverse direction. Simulations suggest an unusually high value 6600 W/(m.K) [21]. CNT are thermally stable up to 2800 °C in vacuum.

In what concerns the mechanical properties, the value obtained for CNT Young's modulus is around 1 TPa [22-24], similar to the accepted value of the in-plane modulus of graphite and being up to 100 times stronger than steel. In 2000, Yu et al measured the highest tensile strength of any material, 52 GPa [23] for ropes of SWNT and 63 GPa MWNT that broke in the outermost layer [25].
The strength of CNT reported depends on the distribution of defects, as well as interlayer interactions in MWNT and bundles of SWNT. The magnitude of these properties depends on the diameter and whether they are single-walled or multi-walled form, as shown in Table 2.1.

Table 2.1 - Typical properties of CNT [26].

Property	SWNT	MWNT
Tensile strength (GPa)	50-500	10-60
Elastic modulus (TPa)	~1	0,3-1
Elongation at break (%)	5,8	-
Density (g/cm^3)	1,3-1,5	1,8-2,0
Specific surface area (m^2/g)	10-20	

At macroscopic level, CNT are a black and thin powder.
The most striking effect, however, is the combination of high flexibility (Figure 2.6) and strength with high Young's modulus, a property that is absent in graphite fibers [27].
The remarkable flexibility of the hexagonal network allows the system to sustain very high bending angles, kinks and highly strained regions. In addition, nanotubes are observed to be extremely resilient, suggesting that even largely distorted configurations can be due to elastic deformations with no atomic defects involved.

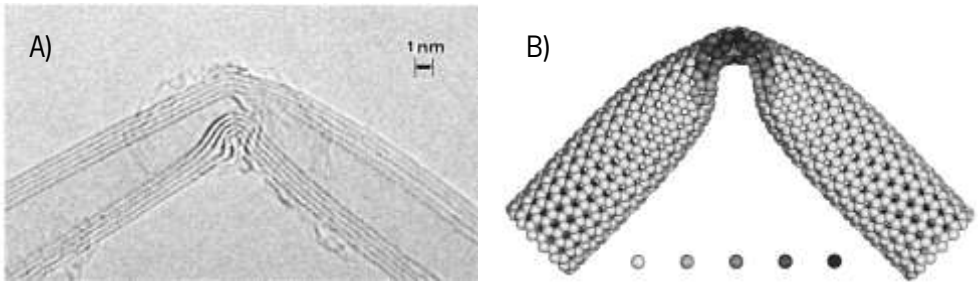

Figure 2.6 - A) HREM image of kink structures formed in nanotubes under mechanical duress and B) computer simulation of nanotube buckling [27].

The high aspect ratio of CNT means that a lower loading of CNT is needed compared to other conductive additives such as carbon black, carbon fiber or stainless steel fiber, to achieve the same electrical conductivity.

With all these properties, CNT are expected to be an excellent additive to impart electrical conductivity in plastics with a wide range of applications.

Table 2.2 sumarizes the main CNT properties from different companies.

Table 2.2 – Properties of the different CNT products.

	Nanocyl™ NC7000 [28]	Baytubes®* C150P [29]	FutureCarbon CNT-MW [30]	Graphistrength® C100 [31]
Carbon purity	>90%	>95%	>90%	>90%
Diameter	9.5 nm	5–20 nm	Not specified	10–15 nm
Length	1.5 µm	1–>10 µm	Not specified	0.1–10 µm
Surface area	250–300 m^2/g	Not specified	~250 m^2/g	Not specified
Bulk density	66 kg/m^3	120–170 kg/m^3	28 kg/m^3	50–150 kg/m^3
Agglomerate size	Not specified	0.1–1 mm	Not specified	0.2–0.5 mm

* Bayer´s production of CNT was discontinued

2.1.2. Applications of carbon nanotubes

CNT have attracted a great deal of attention worldwide with their extraordinary structural, electric and mechanical properties which are leading to many promising applications, including electrostatic painting manufactured already for Ford Taurus, electrochemical devices [32, 33], lithium-ion batteries

or fuel cells [34], field effect transistors [35, 36], field emission displays [37-39], hydrogen production and storage [40], sensors and probes [32, 41, 42] and in conductive and high-strength composites, the first realized major commercial application of CNT [39, 43-45].

The most important application of nanotubes based on their mechanical properties are expected to be as reinforcements in composite materials. Interestingly, CNT polymer composites could be tougher and more scratch-resistant than any other materials, even better than the traditional carbon fibers that have about fifty times the specific strength (strength/density) of steel [34].

However, for these applications, there are challenges to be overcome when processing nanotube composites. This topic will be detailed in the section of the analysis of CNT dispersion.

2.2. Chemical functionalization of carbon nanotubes

Since it is extremely difficult to disperse CNT in a polymer matrix due to their agglomeration, and due to the Van der Waals force, functionalization of CNT is expected to be an effective way to decrease nanotube aggregation. Functional groups bonded at the CNT surface may lead to better dispersion in solvents and polymers and strong interfacial interactions, to improve the load transfer across the CNT/polymer matrix interface. There are several approaches for functionalization of CNT, including covalent and non-covalent functionalization, described in detail, in review papers [12, 26, 46-50].

2.2.1. Covalent functionalization

Covalent functionalization is based on covalent bonding of functional groups onto the CNT. It can be performed at the termini of the tubes or at their sidewalls. This process can be made by reaction with chemically reative molecules such as fluorine [51], and further replacement of the fluorine atoms by amino, alkyl and hydroxyl groups, as reported by Stevens et al [52].

In recent years, other methods have been successfully employed, including cycloaddition reations, such as Diels–Alder reaction [53], carbene and nitrene addition [54, 55] and 1,3 cycloaddition of azomethine ylides [56]. All these methods can be regarded as sidewall functionalization.

Functionalization of CNT with polymer molecules (polymer grafting) is another strategy particularly important for processing of polymer/CNT nanocomposites [57]. Two main categories “grafting to” and “grafting from” approaches have been reported. The “grafting to” approach involves attachment of a preformed polymer chain to the surface of pristine or functionalized CNT via chemical reaction [58, 59]. The main limitation is that initial binding of polymer chains sterically prevents diffusion of additional macromolecules to the surface, leading to a low grafting density. The “grafting from” method is based on growth of the polymer chains from the surface of the CNT with initiators by in situ polymerization of monomers. However, this method requires strict control of the amounts of initiator and substrate as well as control of conditions for the polymerization reaction. This technique was widely used for the preparation of PMMA and other polymer grafted nanotubes [60, 61].

Defect functionalization is another method for covalent functionalization of CNT. This process takes advantage of chemical transformation of defect sites on CNT or defects created on the sidewalls as well as at the open ends of CNT by an oxidative process using strong acids such as HNO_3, H_2SO_4 or a mixture of them [62], or with strong oxidants such as $KMnO_4$ [63] or ozone [64].
The presence of carboxylic acid (-COOH) or hydroxyl (-OH) groups on the nanotube surface represent useful sites for further chemical reactions, such as silanation [65], esterification [66], amidation [67, 68], thiolation [69], alkylation and arylation [70], leading to a reduction of Van der Waals interactions between the CNT, which facilitates the separation of nanotube bundles into individual tubes. Additionally, due to polar groups bonded, the tubes become soluble in polar solvents. Osorio et al [71], based on dispersion analysis in aqueous media, observed that CNT functionalized with a mixture of three acids presented better stability and an higher amount of functional groups adsorbed on the surface.
The oxidative process described is very aggressive, as treatment with strong acids can damage the surface of CNT, as large defects are created on the CNT sidewalls, and is known to produce extensive CNT breakage, reducing the CNT aspect ratio [72]. Aspect ratio must be large to maximize the load transfer to the CNT, crucial to optimize composites strength and stiffness.
The various approaches for covalent functionalization are well summarized by [47, 49, 50].

An appropiate covalent reaction approach is the cycloaddition to π electrons of the CNT, that may provide covalent bonding at the CNT surface and represents a non-aggressive method, compared to the oxidizing acid treatments described above.

Prato et al. [56, 73] reported covalent functionalization of CNT via 1,3-dipolar cycloaddition of azomethine ylides, a very reactive intermediate and bond efficiently to the π-system of the CNT. Treatment of SWNT in DMF with an aldehyde and an *N*-substituted glycine derivative at elevated temperature resulted in the formation of substituted pyrrolidine groups on the SWNT surface (Figure 2.7) and is a powerful tool for enhancing the solubility of CNT in polar solvents. Advantageously, this reaction works well with both SWNT and MWNT.

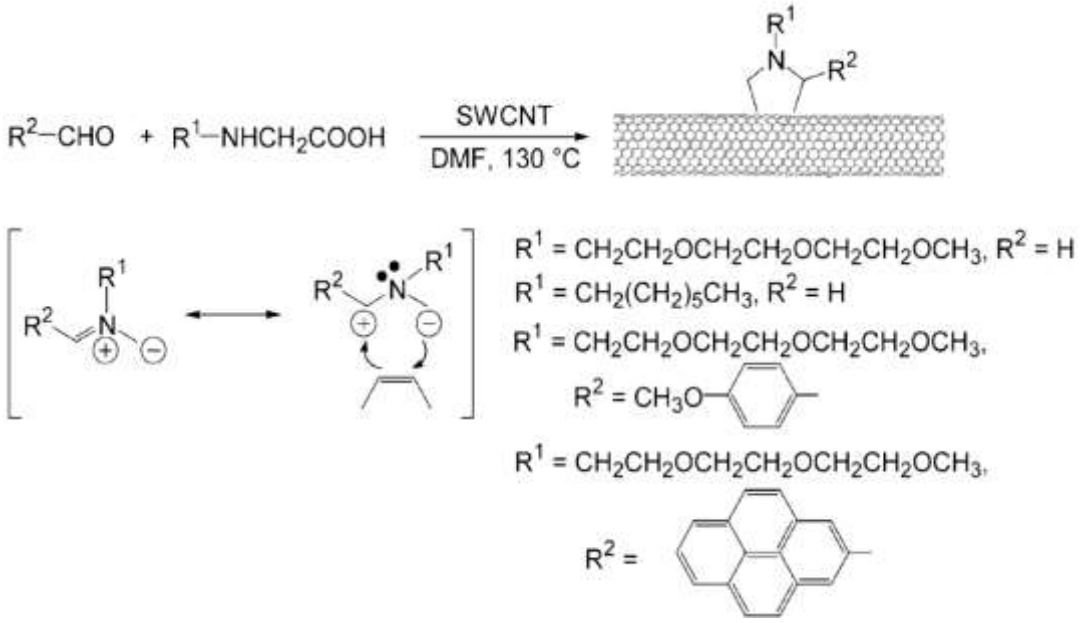

Figure 2.7 - 1,3 - Dipolar addition of azomethine ylides to SWNT and MWNT [47]

In order to increase the number of functional groups present at the CNT surface, without altering their electronic properties, using the addition of azomethine ylides to CNT, dendrimers can be built on the amino function [74].

Although the 1,3-dipolar cycloaddition reaction requires a large amount of DMF and heating during 5 days for the functionalization of CNT. Using microwaves as energy source under solvent-free conditions the reaction time was reduced to 1 h preserving all the types of nanotubes and increasing the number of functional groups per carbon atoms [75]. However, this process was limited to small lab scale production and applying this energy source it is difficult to ensure temperature control and homogeneous reaction conditions.

The 1,3-dipolar cycloaddition reaction of azomethine yilides can also be satisfactory achieved in solvent-free conditions to functionalize CNT. It was applied to functionalize carbon nanofibers (CNF) and scaled up from the few hundreds of milligrams of nanofibers to the tens of grams of nanofibers functionalized per batch [76].

The CNF surface functionalization improved dispersion in a polyamide 6 matrix, CNF/polymer interface and thus the mechanical properties of the composites produced [76]. An increase of 30–60% in elastic modulus and 10–25% in yield strength, from the polymer matrices to the composites, was observed with both PP or PP-g-MA with CNF functionalized by 1,3-dipolar cycloaddition and Diels Alder reaction [77]. The CNF functionalized by the 1,3-dipolar cycloaddition method originated the composites with higher thermal stability. This reaction was applied to CNT, resulting in the formation of a secondary amine as will be described in more detail in chapter 3.

Results show that covalent functionalization plays an essential role on the compatibility of CNT with the matrix. The possible disadvantage concerns the electrical properties that tend to decrease. This may be overcome with the optimization of the chemical treatment.

2.2.2. Non-Covalent functionalization

Non-Covalent functionalization is particularly desirable and has recently attracted increasing research interest for its capacity in leaving the electronic structure of CNT and mechanical properties intact, and improve solubility and processability. This type of functionalization mainly involves wrapping with polymers, surfactants or endohedral molecules (Figure 2.8).

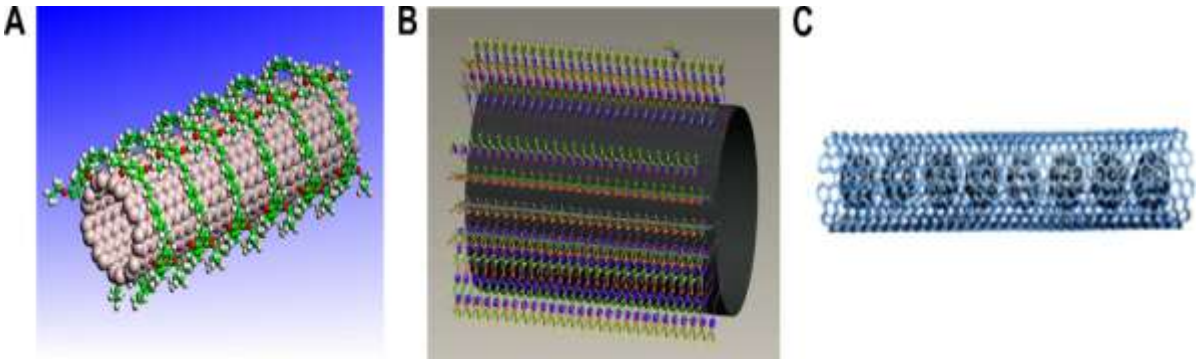

Figure 2.8 - Schematics of CNT functionalization using non-covalent methods (A: polymer wrapping; B: surfactant adsorption; C: endohedral method) [50].

Wrapping with polymers is achieved through the Van der Waals interactions and π–π stacking between CNT and polymer chains containing aromatic rings [78].

The suspension of CNT in the presence of polymers, such as polystyrene [79], lead to the wrapping of polymer around the CNT to form supermolecular complexes of CNT desirable for the preparation of polymeric carbon nanocomposite materials.

The physical adsorption of surfactants on the CNT surface lower the surface tension of CNT and the surfactant-treated CNT overcome the Van der Waals attraction by electrostatic/steric repulsive forces, effectively preventing the formation of aggregates. CNT can be well dispersed using anionic, cationic, and non-ionic surfactants [80] such as sodium dodecylsulfate (SDS) [81] and sodium dodecylbenzene sulfonate (NaDDBS) [82] that are commonly used to decrease CNT aggregation in water. The interaction between surfactants and CNT depends on the nature of the surfactants, such as its alkyl chain length, headgroup size, and charge [83].

In endohedral method, the inner cavity of CNT offers space for the storage of guest atoms or molecules such as C60, Ag, Au and Pt [84] or small biomolecules, such as proteins, DNA [85]. The incorporation often takes place at defect sites localized at the ends or on the sidewalls.

While in chemical functionalization the bonding of functional groups is permanent and mechanically stable, in the non-covalent functionalization bonding is less strong, and restricts some potential applications of CNT, being limited to dispersion in solution.

Major principles of these methods along with the corresponding advantages and disadvantages are summarized in Table 2.3.

Table 2.4 – Advantages and disvantages of various functionalization methods [50].

Method		Principle	Possible damage to CNTs	Easy to use	Interaction with polymer matrix*	Re-agglomeration of CNTs in matrix
Chemical	Sidewall	Hybridization of C atoms from sp^2 to sp^3	√	X	S	√
	Defect	Defect transformation	√	√	S	√
Physical	Polymer wrapping	Van der Waals force, π-π stacking	X	√	V	X
	Surfactant adsorption	Physical adsorption	X	√	W	X
	Endohedral method	Capillary effect	X	X	W	√

* S: Strong; W: Weak; V: Variable according to the miscibility between matrix and polymer on CNT.

2.3. Composite processing

The effective use of CNT as reinforcements for high strength polymer composites depends strongly on the ability to disperse them uniformly throughout the matrix and on the good interfacial interaction with the matrix, to achieve effective load transfer across the CNT-matrix interface, without reducing their aspect ratio. Currently, several processing methods are available for producing polymer/CNT composites based on either thermoplastics or thermoset matrices such as: solution mixing, in situ polymerization and melt blending.

Processing methods known thus far for CNT-based composites are described below. Due to the large volume of related literature, only the seminal works will be discussed for each processing method.

2.3.1. In-situ polymerization

The main advantage of this method is that reinforcement is obtained at molecular scale. The CNT are dispersed in monomer, followed by polymerization. It enables grafting of polymer molecules onto the walls of CNT, mixed with free polymer chains. Moreover, due to the small size of monomeric molecules, the homogeneity of the resulting composite adducts may be much higher than mixing CNT/polymer in solution in particular if the CNT are compatible with the monomer. In this sense, it is a convenient processing technique, which allows the preparation of composites with high nanotube loading and good miscibility with many polymer types [86, 87]. This technique is particularly important for the preparation of insoluble and thermally unstable polymers, which cannot be processed by solution or melt processing (Figure 2.9). Depending on required molecular weight and molecular weight distribution of polymers, chain transfer, radical, anionic, and ring-opening polymerizations can be used for in situ polymerization processing.

This method has been used with intrinsically conducting polymers. The recent advances in situ polymerization resulted in new polymer/CNT composites with improved mechanical properties [86].

The in situ radical polymerization was used for several nanocomposites synthesis with polymer such as: poly(methyl methacrylate) [88], polypropylene [89], polyamide 6 [90, 91] and polimide [92].

Figure 2.9 - MWNT (left) and MWNTCOOH (right) in the master solution of polyamide 6 after stored for 24h. There is no evidence of phase separation or precipitation [91].

As described, in situ polymerization can be applied for the preparation of almost any polymer composites containing CNT. The bonds between polymer and nanotube involve physical adsorption and wrapping of polymer molecules through Van der Waals and π-π interactions. Covalently functionalized CNT may graft polymer molecules during in situ polimerization.

2.3.2. Solution processing of composites

The most common method for preparing CNT/polymer composites has been to mix both components into a suitable solvent. Combining with high power ultrasonication process the mixture of nanotubes with polymer solution is more effective and the aggregates of CNT may be effectively broken down. The disadvantage is that high power ultrasonication also breakes the CNT, decreasing their aspect ratio, and thus, their reinforcing ability. The CNT/polymer composites are formed by precipitation or by evaporation of the solvent to form a composite film.

It should be noted that this method relies on the efficient dispersion of nanotubes in the suitable solvent according to the solubility of the polymer. However pristine nanotubes do not form stable suspensions in most solvents. To get around this problem, mainly with higher loading of nanotubes, a number of groups have used an additive such as a surfactant to disperse the nanotubes before mixing with the polymer solution [93]. The most common choices of surfactant are derivatives of sodium dodecylsulfate (SDS). This technique results in improved dispersion.

Solution mixing and precipitation technique has been used to improve the dispersion of CNT in a polycarbonate [94], in polypropylene [95] or polyurethane [96] with addition of SDS. CNT were untangled and well dispersed into the polymer matrix due to both ultrasonics and stirring.

When using solution blending, nanotubes tend to agglomerate during slow solvent evaporation. In order to succeed rapid evaporation of solvent during the suspension, casting techniques [97, 98] or coagulation have been proposed [99].

Moreover, solution-based processing methods are time consuming and can damage the CNT during the mixing procedure.

2.3.3. Melt mixing

As described above for solution mixing, the matrix polymer must be soluble in at least one solvent which is problematic for many polymers. Besides, the use of large amounts of solvents carries a large environmental burden.

An alternative method is melt mixing, a common and simple method, that can be used with thermoplastic polymers, due to the fact that they soften and melt when heated above their melting point.

In melt mixing, CNT are mechanically dispersed into a polymer matrix using a high temperature and high shear force mixer or compounder. The shear forces help to break nanotube agglomerates or prevent their formation [86, 87].

Advantages of this technique are its high rate and simplicity, not to mention its compatibility with standard industrial techniques.

Melt mixing may be achieved by different kinds of methods such as: batch processing and continuous processing.

For batch processing the equipment used are Batch mixers and microcompounders. There are several mini mixers available, namely Haake, DACA microcompounder, MiniMax, DSM microcompounder. DACA and Haake mainly used in laboratory research and development [100-102].

These mini mixers process small amount of material which is a benefit considering the high cost of the CNT. Besides, for the study of controlling factors for melt mixing, it seems appropriate and meaningful the use of small scale mixers to evaluate nanocomposites made with CNT. Although this represent a significant disadvantage compared to extruders, they do not allow a continuous processing so do not reproduce accurately the preparation of composites in industrial scale.

Two types of extruders may be considered, single and twin screw extruders. At the industrial scale, twin screw extruders are commonly used to produce polymer composites since allow a continuous output and high amount of material, in opposition to the discontinuous mixers.

The twin-screw extruder (particularly co-rotating) presents more potential for producing polymer composites since have more ability to disperse and distribute CNT than single screw extruder [103].

Their design allows the modification of the feeding location and screw configuration and the control of the temperature along the barrel and die Figure 2.10.

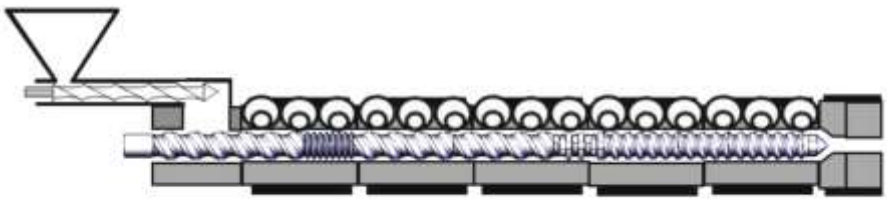

Figure 2.10 - Schematic representation of the prototype modular co-rotating twin screw extruder [104].

Homogeneous CNT dispersion throughout PA6 matrix and significant enhancements in mechanical properties were achieved for 1 wt % MWNT/PA6 composites [105] prepared via melt-compounding method using a Brabender twin-screw mixer and compression molding.

The influence of processing conditions using a twin-screw extrusion were studied. Villmow et al. [106, 107] showed that high rotation speed, higher temperature profile and a screw profile with mainly mixing elements and lower residence time lead to decreasing CNT agglomerate size and resulted in the best dispersion and lower electrical percolation threshold. It was reported that polymer melt viscosity and molecular weight also affect CNT agglomerate dispersion [108]. Even though increasing the residence time and/or the mixing speed can increase the energy input and hence improve the dispersion, it may also lead to CNT breakage [109].

Recently, it was reported that the simple application of a converging/diverging flow sequence in a capillary rheometer to the CNF/PP composite melt lead to a better dispersion than the conventional twin-screw extrusion [104].

Haggenmueller et al. [110] used a combination of solvent casting, melt mixing and melt spinning to prepare SWNT/PMMA. The dispersion increased with each additional melt mixing cycle and due to the alignment of the SWNT along the fiber axis, these nanocomposites showed improved mechanical and electrical properties.

The disadvantage of melt mixing method is that the dispersion of CNT in a polymer matrix is quite poor compared to the dispersion that may be achieved through solution mixing. In addition, the CNT loading must be lower due to the high viscosities of the composites at higher loading of CNT.

Well-dispersed CNT were obtained by extrusion and injection molding [111]. Most of the fiber breakage occurs in the initial compounding stage in the extruder, and no further changes were perceived after subsequent processing cycles such as injection molding.
At industrial scale, polymer processing methods such as injection molding required large-scale quantities of raw materials, which are inappropriate for expensive fillers such as CNT.
Compression molding and solution based processing methods are also used to shape the samples. However, these processing methods are limited to small-scale production of polymeric parts, requiring longer processing time and being limited to producing simple parts. An industrial alternative to produce parts with small dimentions is microinjection molding.

2.3.4. Microinjection molding

For CNT/ polymer production a mixing process, for example, melt extrusion is first necessary. Depending on the final morphology/shape of the composites desired and the equipment available, then the samples can be processed by compression molding or by injection molding.
In the last few years, there has been an increasing trend towards product miniaturization with the rapid development of micro-engineering technologies, that make possible the serial production of micro-structures on a large scale. In this context, microinjection molding (μIM) is one of the key technologies for micro-manufacture. This technique has mass-production capability due to high level of automation, short cycle times, relatively low component cost considering the small material quantities required for micro components and the waste of polymer is considerably minimized [112]. Therefore, use of μIM in industry and the number of scientific studies in this field is increasing.

There are a number of definitions of what is a microinjection moulded product. According to the dimensions of manufactured parts [113, 114], μIM includes two areas while Whiteside et al. [115] and Ruprecht et al. [116] suggested μIM could cover three areas:

- Microinjection of parts: parts with weight in the range of milligrams, overall dimensions, functional features, and tolerance requirements expressed in terms of micrometers;

- Microstructural parts: parts with dimensions in the macro-range, weight of the order of grams but that possess micro-structured regions with microstructural details.
- Microprecision parts: parts of any size, but with tolerance requirements that are expressed in terms of micrometers

2.3.4.1. µIM process

Among the various micro-molding processes, such as hot embossing and microthermoforming [117, 118], µIM possesses the advantage of process the wide range of thermoplastics available, having standardized process sequences, a high level of automation and short cycle times [119], cost-effectiveness for mass-production, very accurate shape replication and good dimension control [120], low maintenance costs of equipment and applicability of the large amount of industrial information and 'know-how' available from conventional injection moulding.

Nevertheless the know-how of conventional injection cannot be transferred easily to µIM since the material behavior changes in the micro-scale are different due to the dimensions of the cavity (typically in the sub-millimetre range and even down to a few micrometres) and the filling time of the cavity (in the order of a few tens of milliseconds) [121].

The µIM process comprises the following process steps [122]: mold closing, injection, holding, cooling, plasticization, mold opening and part ejection. The mold cavity equipped with a micro structured tool (mold insert) is closed and a ram or piston is used to injected a plascicized material. The pressure control mode is activated and replaces the speed control mode. The material is then forced under pressure inside a mould cavity where it is subjected to holding pressure. The polymer (and the tool) is cooled down below its glass transition temperature. The machine then plasticates a prescribe amount of new material, according to the course establish, for preparation of the next shot. The cooling continues and once the set ejection temperature is reached, the mold is opened and the molded part ejected as illustrated in Figure 2.11.

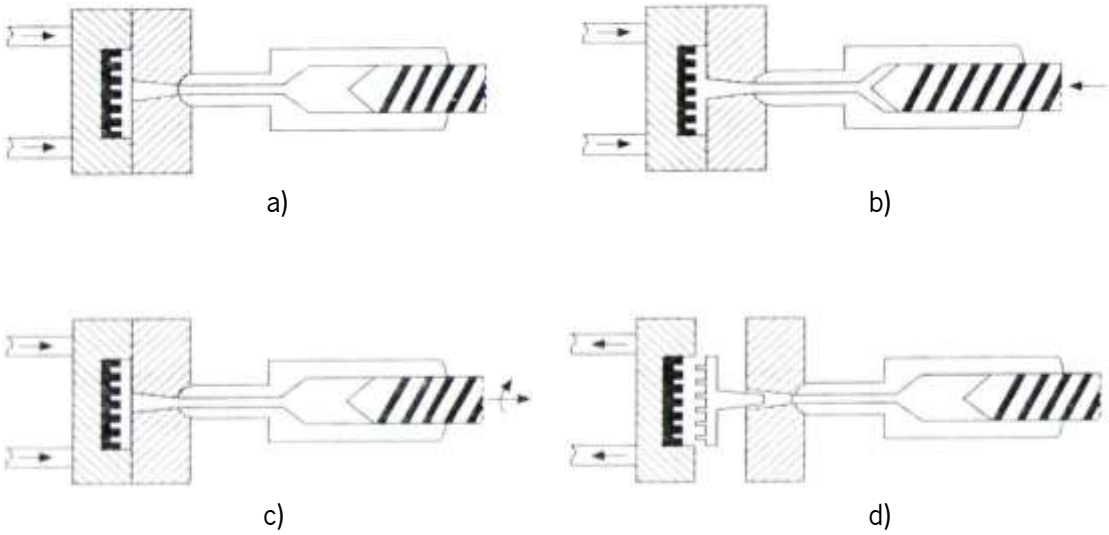

Figure 2.11 - Typical stages involved in microinjection molding: (a) mold closing, (b) injection and holding, (c) cooling and plastication, (d) mold opening and part ejection [122].

One particular obstacle in μIM comes from the difficulty in filling high aspect ratio microstructures. The polymer melt can prematurely freeze before the full feature depth could be filled. This difficult can be overcome increasing the mold temperature. However this increases the cycle time. A solution is a mold with rapid heating and cooling capability. This cyclic temperature control is called variothermal process [123-125], rapid thermal response molding [126], or dynamic mold temperature control. Rapid cooling can be simply achieved in a conventional way, e.g., by circulating water in the mold base.

In μIM, the main challenge is the replications of micro features with high aspect ratios. The high surface area to volume ratio of the micro cavities makes the melt fill freeze or solidify much faster than in conventional injection molding which can lead to an incomplete filling of micro features.

Thus, many research groups investigate the factors that improve the surface quality. The melt and mold temperatures and injection speed [127, 128] are considered as the main factors affecting the part quality in μIM. Holding time and holding pressure were also identified as moulding factors with significant effects [129]. For Pirskanen et al. [130] the best replication results were achieved when a small injection piston diameter and large shot size and for Ong et al. [131] and Sha et al. [114], high mold temperature, high injection rate and high injection pressure are recommended for the filling process. However, when comparing the magnitude of their influence on the melt filling quality the reported results are not consistent.

Once a mold insert has been made and processing conditions stablish, several thousand parts can be molded with little effort. Figure 2.12 displays a photograph of microparts made from PC as they come from the μIM machine. They are still connected to the sprue and runners.

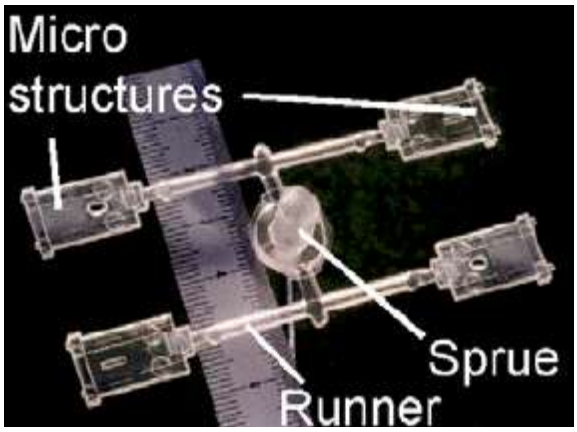

Figure 2.12 – Typical batch of micro structures as it comes from an injection-molding machine [116].

2.3.4.2. Microinjection equipment

Today in the market there are several μIM machines manufactures such as: Arburg, Rondol, Cronoplast, Sumitomo, Dr Boy, Engel, Ferromatik, Itron, Nissei and Battenfeld. These microinjection machines, with clamp forces between 2 and 15 Tn, are based on the overall configuration of a common injection machine but, according to the manufacturer, they incorporate certain amendments aimed at facilitating mechanical processing of extremely small volumes of plastic (small plates with very low clamping force, small groups of injecting operated by pistons, plasticizing through bearings, totally electric drive, special screw feeder for micropellets, ultra-high speed controllers).

Another approach consists an eventual separation between the injection unit and the plastating unit as Battenfeld Microsystem 50, where the plasticization is performed in the extrusion screw or hot cylinder and mounted at angle to the inject axis.

The smallest machine in the range designed particularly for micro moulding and continuous output, equipped with only 12 mm standard plasticising unit, is the BOY 12 (Figure 2.13), a fully hydraulic that precisely meters small injection volumes less than 0.1cm^3 with high repeatability. Boy 12 possesses an injection unit in two steps: plasticizer screw and injection piston with reduced dimentions compared to those for conventional injection molding (Figure 2.14). Hardware to increase precision and a viewer system to inspect the injected pieces are available. Other characteristics are listed below [132].

- Clamping force: 129 kN
- Minimum height of the mold: 100 mm
- Course opening: 200 mm
- Course extraction: 30 mm
- Screw diameter: 14 mm and L/D 18:1
- Maximum injection volume: 6,1 cm^3
- Injection pressure: 190 MPa
- Weight: 760 kg

Figure 2.13 – Boy 12A [132].

Figure 2.14 - Comparison of dimensions between screw and injection plungers for μIM (left) and a screw for conventional injection molding (right) [113].

As in conventional molding process, the micromolding material undergoes a coupled of mechanical and thermal influences. Although, high shear and rapid cooling rates combined with a large surface area to volume ratio may have a much greater influence over the morphology and resultant properties of a micromoulded product that are different from that in conventionally molded parts [121].

2.3.4.3. Applications

The use of micro-systems covers very large and differentiated fields. Some examples are illustrated at Figure 2.15 and Figure 2.16 and include information technology components (reading caps for hard disc [133], ink jet printers nozzles [134], etc.), medical and biomedical devices [120] (pacemaker, sensors, auditory devices, lenses, micro-fluidic systems for blood and DNA analysis, etc.), high technology products (palm-sized high-definition displays, mobile phones etc.), micro-optics [135, 136] (waveguides, micro-lenses, fiber connectors), micro-mechanics [137] (micro-gears, micro-actuators,

micro-pumps, micro-switches), electronic circuit boards and electrical switches [138, 139] and many more are expected to arise in the future.

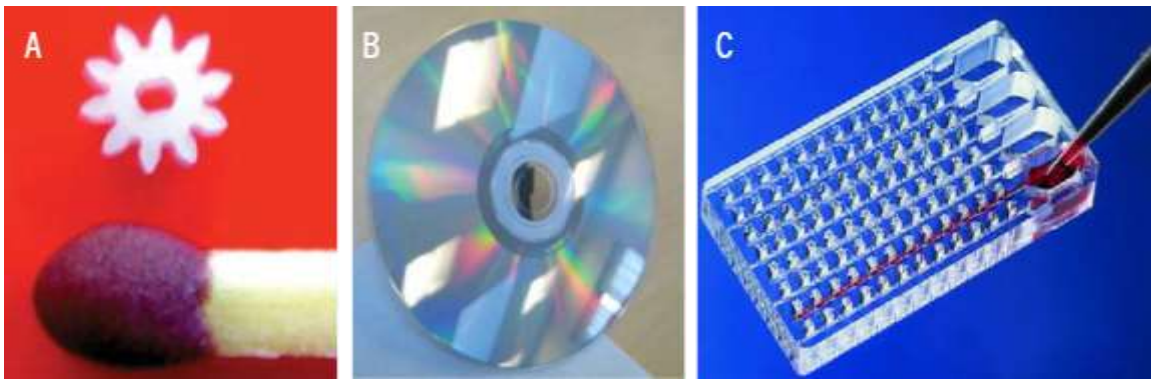

Figure 2.15 - Example of a micro-molded part: A - micro-gear; B - macro-part with a micro-structured region (DVD disc) [113] C - cell chip LILLIPUT made by injection molding [140].

Figure 2.16 - Examples of microparts with weight in the range of milligrams [141].

These microparts have zones of critical dimensions, such as hollows of the size of a pin, bolts, channels and hooking systems.

2.4. Physical properties of polymer/carbon nanotubes nanocomposites

2.4.1. Electrical properties

CNT bear a high potential for electric applications in plastics due to their huge aspect ratio. This facilities the production of conducting polymer structures at low loadings of nanotube fillers without compromising other performance aspects of the polymers such as their low weight, low melt viscosities, etc., which has triggered an enormous activity world-wide in this scientific area.

In a polymer matrix, as the concentration of CNT progressively increases, there is a critical concentration that corresponds to a sudden increase of electrical conductivity by several orders of magnitude. This critical concentration is defined as percolation threshold.

Below this value the composite remains electrically insulating because the conductive particles are dispersed or grouped into small clusters.

Both experimentally and theoretically results have shown that the percolation threshold decrease with increasing the filler aspect ratio [142, 143].

CNT become the most interesting fillers for conductive polymer composites and has encouraged world-wide researches, since their large aspect ratio and excellent conductivity can result in exceptional low percolation thresholds [144, 145].

The electrical conductivity of such composites is usually discussed in terms of percolation theory and is given by the percolation scaling law $\sigma(p) = \sigma_0(p - p_c)^t$ where σ is the electrical conductivity, σ_0 is a prefactor, p is the concentration of the conducting phase, p_c is the percolation threshold concentration and t the critical exponent. The values for the exponent t, observed for polymers filled with carbon black, carbon fibers, CNT and graphene sheets, are typically in the range of 1 to 4 [146].

For CNT, typical concentration values for the electrical percolations are lower than 5 wt% loading, as opposed to 8-20 wt% for most carbon black containing compounds [147,148].

After the percolation threshold, a further increasing in the filler loading usually has little effect on the composite electrical conductivity, as shown in Figure 2.17. Besides this, additional amount of CNT will increase the viscosity and difficult the processing method.

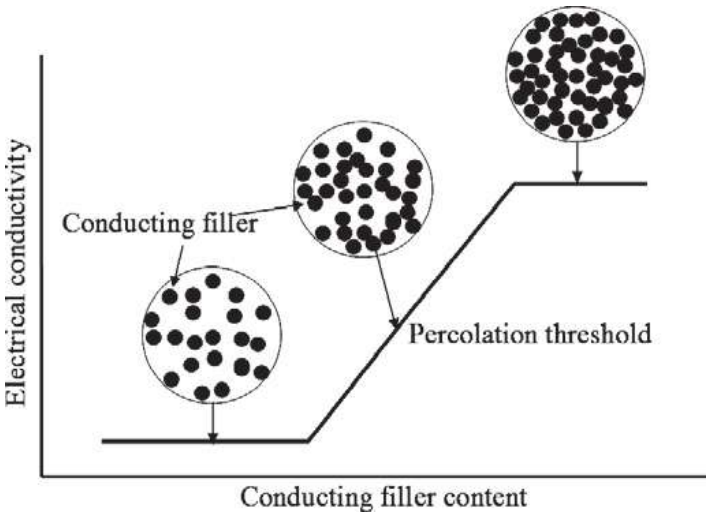

Figure 2.17 - Schematic of percolation phenomenon and conducting network in conducting composites [50].

Building a conductive network within an insulative matrix at lower concentration need well dispersed CNT but does not necessarily require well distributed CNT as illustrated in Figure 2.18.

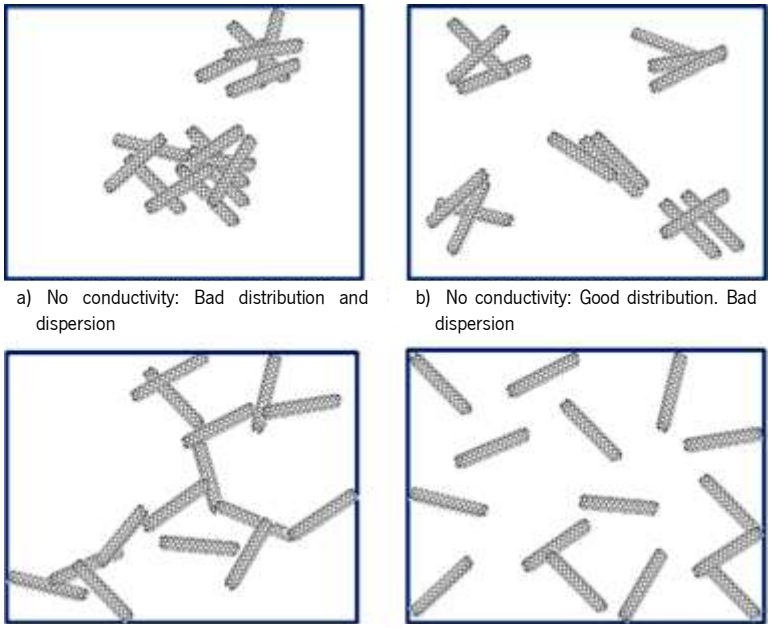

Figure 2.18 – Schematic sketches show the effect of 1D filler on the conductivity of polymer composite [149].

The electrical percolation threshold for nanocomposites depends on the dispersion state and aspect ratio of CNT [150], composite processing methods [151], degree of surface modification [56] of CNT and type of polymer [152]. The correlation of minimum percolation threshold and maximum conductivity on the CNT production method seems to be lower compared to the type of polymer and

dispersion method. This can only be explained with the marked distance dependence of tunneling or jumping where the electron must overcome a barrier potential [153].The electric current may flow by means of tunnelling if direct contact between CNT are not available. Nevertheless, some polymer types favor the formation of insulating polymer coatings of different thicknesses on the CNT surface [151].

For industrial applications, the reduction of the electrical percolation threshold in CNT/polymer composites is an economical decisive factor. In this sense, extensive review for experimental and theoretical work about the electrical percolation of carbon nanotubes for various polymer matrixes was published [151, 154]. Table 2.5 represents some published data in this field.

Table 2.5 - Summary of experimental parameters and conductivity results for polymer/CNT composites

Polymer	Filler type	Percolation threshold (wt %)	Composite electrical conductivity (S/m)	Processing method	Ref.
PC	SWNT	1,5 – 2,0	-	Melt mixing	[155]
		0,8		Coagulation	
LDPE	MWNT	1–3	2 (10 wt%)	High energy ball milling	[156]
PP	MWNT	1,1	4,60 (10,7 wt%)	Melt mixing	[157]
Nylon 6	MWNT	≈ 2-3	$\approx 10^{-3}$(2 wt%)	Melt mixing	[158]
	f- MWNT	0,5	$\approx 10^{-2}$(2 wt%)		
	MWNT	4-6	-	Melt mixing/IM	[159]
	MWNT	2-2,5	0,1 (5 wt%)	Melt mixing	[160]
Nylon 6,6	MWNT	0,5-1	0,1 (5 wt%)	Melt mixing	[160]

The effect of thermoplastic matrix and injection/microinjection conditions on the conductive network will be explored in chapter 6 since depend on the state of dispersion.

2.4.2. Mechanical properties

To employ CNT as effective reinforcement in polymer nanocomposites, four main requirements have to be met: proper dispersion, alignment, large aspect ratio and appropriate interfacial adhesion between the CNT and polymer matrix [86].

Dispersion is probably the most fundamental issue. CNT uniformly dispersed result in a more uniform stress distribution, an efficient load transfer to the nanotube network and minimizes the presence of

stress concentration centers increasing the strength and modulus. However, beyond a critical CNT loading, additional CNT will promote the formation of aggregates, diminishing CNT/polymer adhesion and consequently, decreasing mechanical properties.

Although it is extremely difficult to separate individual nanotubes during mixing with polymers due to strong attractive interactions, nanotubes aggregate to form bundles which are difficult to disrupt. Furthermore, these bundles are tangled with each other Besides that, it is difficult to fabricate high nanotube weight fraction composites, considering the high viscosity for CNT/polymer mixtures obtained.

However, this limitation may be overcome by introducing functional groups on the CNT surface that can help dispersion in the composite material by improving the interface with the surrounding polymer chains as described previously in section 2.2. As a result, external stresses applied to the composite are efficiently transferred to the nanotubes.

Depending on the polymer used and processing conditions, the reported measured strength is variable. The Young's modulus and tensile strength of SWNT/PP composites considerably increase in the presence of nanotubes, until a maximum for 0.75 wt.% SWNT, further amounts lead to a marked decrease [161].

Alignment is a less crucial issue for mechanical properties but relevant for μIM composites mainly in what concerns electrical properties as will be referred in detail.

When a certain degree of alignment of CNT in PS is achieved the improvement in elastic modulus may reach five times that of the randomly oriented composite [162]. Nevertheless, a perfect alignment is not always beneficial for electrical properties.

Spitalsky et al. [87] examined a vast collection of published data relatively to mechanical properties of CNT/polymer composites considering many parameters, such as CNT type, growth method, chemical pre-treatment as well as polymer type and processing strategy.

The brief outlook bellow describes the recent published work based on CNT/PA composites.

In 2004, Meincke et al [159], fabricated composites from CVD-MWNT in PA6 on a corotating twin-screw extruder. This almost doubled the modulus, from 2.6 to 4.2 GPa at 12.5 wt.%. However, this was accompanied by a significant reduction in the elongation at break, as for a consequence the ductility of the materials decreased dramatically from 40% to just 4%.

Zhang and co-workers [163] made composites from CVD-MWNT in polyamide 6 by the simple melt-compounding using a Brabender twin-screw mixer. They observed a threefold increase in modulus

from 0.4 GPa to 1.24 GPa by addition of only 2 wt.% nanotubes (Figure 2.19). In addition, a significant increase in yield strength from 18 to 47 MPa was observed with similar increase in ultimate tensile strength. Furthermore, no decrease in toughness was observed as the ductility only fell slightly from 150% to 110%.

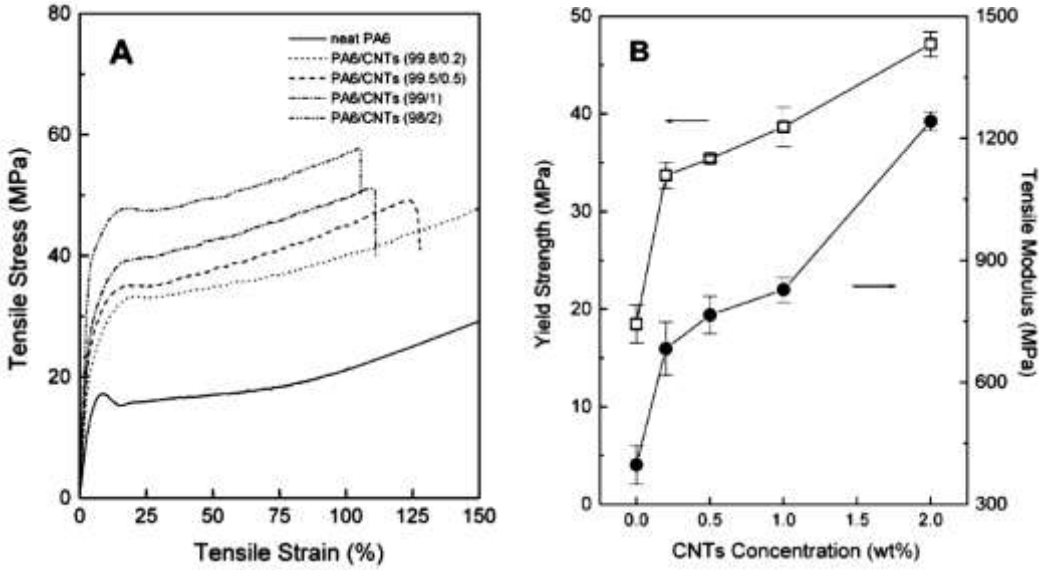

Figure 2.19 - (A) Typical stress-strain curves. (B) Tensile stress (at yield) and tensile modulus for PA6 and its nanocomposites as a function of MWNT concentration [163].

The results were lower for nanocomposites produced in a mini twin screw extruded and μIM but improved for functionalized MWNT compared with commercial MWNT [164].

In all cases, microscopy observations indicate a uniform and fine dispersion of MWNT throughout PA6 matrix and a strong interfacial adhesion (Figure 2.20) which is responsible for this remarkable enhancement in overall mechanical properties of the nanocomposites prepared.

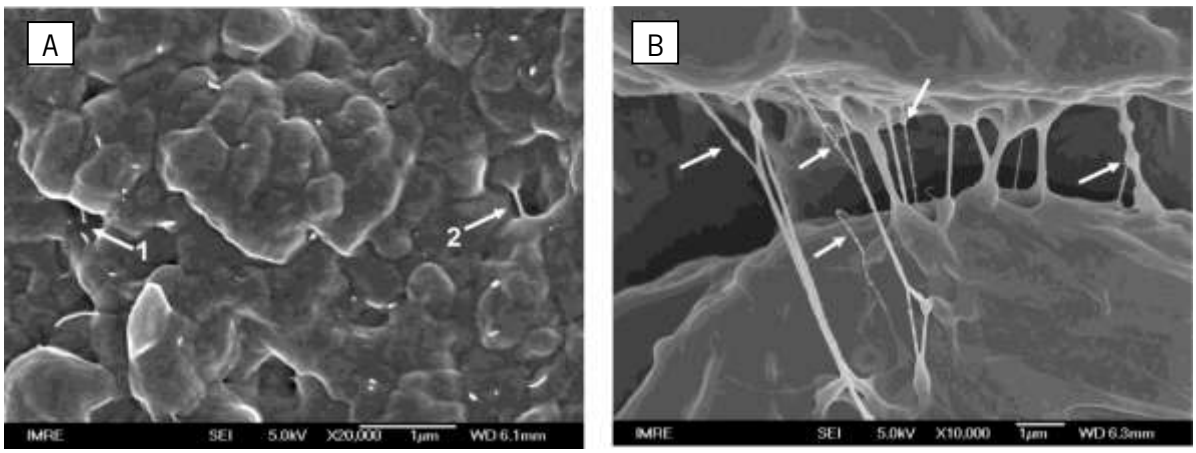

Figure 2.20 - A - SEM image showing microcracks linked by stretched nanotubes in PA6 nanocomposites. B - CNT sheathed with polymer in PA6 nanocomposites [163].

In some cases, fragmentation of the tubes has been observed, which is an indication of a strong interface bonding is. In some cases, the effect of sliding of layers of MWNT and easy pull-out are seen, suggesting poor interface bonding.

2.4.3. Thermal properties

The massive thermal conductivity of CNT can be exploited to make thermally conductive composites. SWNT were used to enhance the thermal transport properties of industrial epoxy. Samples loaded with 1 wt % SWNT showed a 70% increase in thermal conductivity at 40 K, rising to 125% at room temperature[165].

Thermal stability of polymers may be affected by the presence of the nanotubes, that interfere with the mobility and crystallization of the polymer chains [166, 167]. The nanotubes delay the onset of thermal degradation of the polymer, for example, PMMA or PVOH [86], and enable the composite to be used for high temperature applications [168]. The addition of 1 wt% CNT to epoxy increases the glass transition temperature from 63 to 88°C [169].

Thostenson et al. [170] reported that for 5 wt.% CNT concentration the thermal conductivity increases 60% over that of the unreinforced epoxy. Unlike electrical conductivity, where a sharp percolation threshold is seen, the increase in thermal conductivity with increasing nanotube concentration is nearly linear.

2.5. Dispersion of carbon nanotubes in polymers

The CNT dispersion in a polymer matrix can be characterized at various scales, from the macro to the nano level.

2.5.1. Direct methods

The quantification of CNT dispersion state at the macroscopic level is accessible by optical microscopy (OM). Using an image analysis program [171], the images acquired from microtomed sections of the composite, observed under transmition optical microscopy, may be analyzed. Typically, the CNT agglomerates can be observed as dark spots, and their area measured.

To determine the macrodispersion, Kasaliwal et al. [172, 173] developed a method based on the macrodispersion index, *D,* described by the equation $D = 1 - f\frac{A/A_0}{\varphi}$. The agglomerate area ratio, A/A_0, corresponds to the ratio of the total agglomerate area (*A*) to the total compsite area analyzed (A_0) and assesses the amount of the non-dispersed CNT.The parameter φ is the volume fraction of the filler and *f* is a factor related to the effective volume of the filler. For CNT, *f* was estimated to be 0.25, but it depends on the type of CNT.

D ranges from 0 to 1, with 1 indicating perfect dispersion.

The state of dispersion was also characterized through the analysis of the cumulative area ratio of the CNT agglomerates [107, 104, 174]. This method is interesting to compare CNT agglomerate distributions of different composites, but it does not provide information about the absolute state of dispersion.

OM does not provide a simple, quantitative measure of dispersion. Several images must be processed to guarantee a statistical result to quantify the CNT dispersion state. Even so, the information obtained is 2D, and a full description of dispersion would require a 3D description of the system.

At the nanoscale level, atomic force microscopy (AFM) is used to measure the CNT diameter (about 12-15 nm after processing). Altough it is not correct to discuss the length of the tubes since in AFM micrographs only parts of the tubes are visible at the cut surface [175].

Direct measurements of CNT dispersion in a polymer can also be performed by UV–visible spectroscopy. Nevertheless, only individual CNT are active in the UV–visible spectrum, and thus it is normally applied to CNT dispersions in solution, coupled with transmission electron microscopy (TEM) [81, 176].

Pötschke et al. [177] used TEM to analyze qualitatively the state of dispersion. The micrographs show that the CNT appear uniformly distributed as individual tubes, without significant agglomeration and no preferred orientation of CNT in extrusion direction is observed. To quantify the dispersion of CNT in PS, Bellayer et al. [178] used a histogram of the distribution of the distances between the neighbouring CNT based on TEM images. The volume fraction of dispersed CNT was estimated by Stoyan et al. [179] considering the mean length of projected CNT per unit area, and the section thickness.

Quantitative information concerning the spatial relationship between individual CNT is difficult to obtain since the 2D micrographs only partially reflect the 3D structure of the material. Also, the TEM images may not be representative of the entired sample. Thus the ‘true’ dispersion situation cannot be resolved.

Recently, Krause et al. [180] developed a relatively simple method to determine the length distribution of CNT before and after extrusion (Figure 2.21). A suitable solvent was selected to dissolve the matrix of melt mixed 2% CNT/PC composites and disperse the CNT, in order to perform TEM. Investigations indicated a significant shortening after melt processing up to 30% of the initial length.

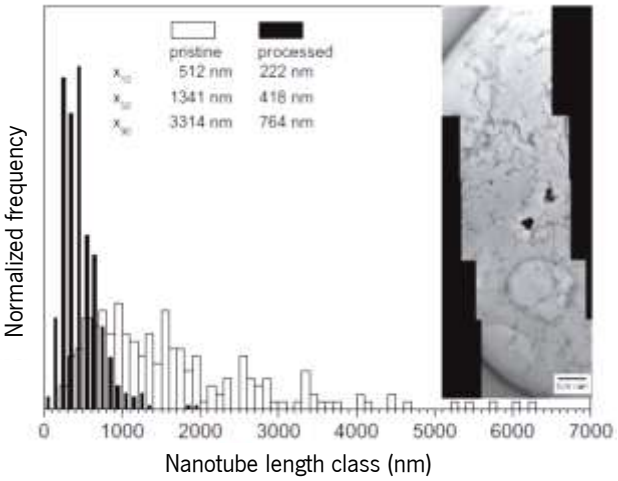

Figure 2.21 – Comparison of length distributions of Nanocyl™ NC7000: before (pristine MWNT) and after processing (as recovered from an extruded PC composite with 2 wt% CNT), including TEM images of processed NC7000 presented on the right-hand side [180].

Spatial statistics and image processing techniques were also applied to TEM images to obtain quantitative information about CNT dispersion, distribution and alignment [181].

Scanning electron microscopy (SEM) coupled with OM was also used for analyzing dispersion, the state of alignment and dimensions of CNT in the epoxy resin [145]. Interfaces between CNT-agglomerates and PP-matrix, distribution and dispersion of small agglomerates and individualized CNT in different PP were studied by Mičušík et al. using SEM [157].

TEM and SEM allow measuring the CNTdispersion on a small composite section. The evaluate of large specimen areas is unrealistic. The small section analyzed may not be representative of the entire material sample. Furthermore, these techniques are time consuming and expensive, in particular the preparation of samples for TEM is rather difficult.

Recently, a new model was proposed, based on the composite index, compIndex, that takes into account the dispersion index and agglomerate size distribution index of the CNT [182]. Based on simulations, the number of clusters, the average number of contact per fiber, the relation to shear flow and electrical conductivity could be obtained [183].

2.5.2. Indirect methods

Electrical conductivity, viscosity, storage modulus and mechanical parameters may be used to assess the state of dispersion, although, providing a qualitative insight about the dispersion state. The correlation between these parameters and micro or macrodispersion is not simple.

For example, Le et al. [172] demonstrated that the macro and microdispersion, respectively, investigated by OM and AFM, increases insignificantly with mixing time but they observed that the conductance followed this increase initially, but decayed gradually along the time of mixing. According to Figure 2.22 there is a critical mixing time.

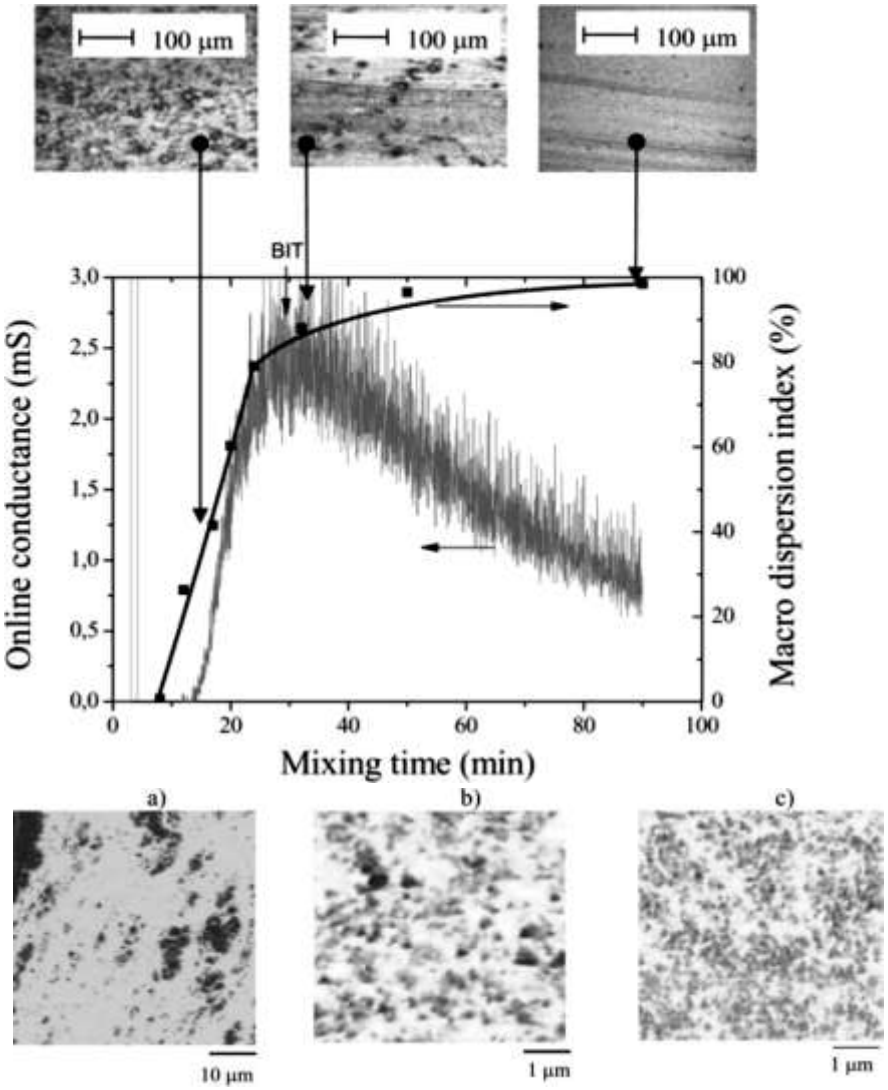

Figure 2.22 - Online conductance, macrodispersion index, at the top OM images and at the bottom AFM-images of CNT-rubber nanocomposites. Samples taken at 13 min (a), 32 min (b) and 90 min (c) [172].

Logakis et al. [184] proposed that CNT dispersion can be assessed indirectly through both the DC conductivity and the crystallization temperature of the CNT/PP nanocomposites. The higher conductivity levels obtained under high rotation speed, temperature or high mixing time, conditions that increase the energy input to the system, are related to the disentanglement of CNT which facilitates the formation of more conducting pathways.

Moreover, it was observed that the crystallization temperature (T_c) increases for CNT/PP nanocomposites. This is interpreted as resulting from better disentanglement and spatial distribution of the CNT within the polymer matrix which offer a higher effective surface and higher number of sites for the nucleation of the polymer chains during crystallization.

For nanocomposites with 0,5% PMMA/SWNT [185], a good correlation between the quantified dispersion levels and physical properties was observed. Storage modulus showed an increase of four orders of magnitude and electric conductivity almost eight orders of magnitude at the highest dispersion level.

The composite mechanical properties are largely affected by the presence of CNT agglomerates, and vary considerably with the CNT dispersion level. Thus, the mechanical properties may also be used as an indicative of CNT dispersion.

For 2% PA6/CNT nanocomposites [163], mechanical testing showed that, compared with neat PA6, the elastic modulus and the yield strength of the composite were greatly improved by about 214% and 162%, respectively. This was attributed to the good CNT dispersion and adhesion to the polymer matrix.

Indeed, these indirect control methods seems to be more effective and less time consuming as compared to the usually applied microscopy techniques above mentioned.

2.5.3. CNT dispersion mechanism

The dispersion of CNT in other materials (solvents, polymer solutions, or polymer melts) requires their disentanglement from the agglomerates that they form. For this process to take place, the CNT agglomerates have to be infiltrated by the matrix material that should wet the CNT surface. The dispersion of nanofillers in polymer melts is usually described to follow two mechanisms: agglomerate rupture and agglomerate erosion [174].

The effectiveness of dispersion through these mechanisms depends on the CNT and polymer characteristics.

The change in size of large agglomerates into smaller parts can be processed by two mechanisms. If large agglomerates are broken down into smaller ones in short times they undergo a rupture mechanism (a bulk phenomenon); whereas free tubes as well as small fragments and agglomerates are eroded from the surface of bigger agglomerate, they experience erosion (a surface phenomenon), needing comparatively longer time [174] as shows Figure 2.23 and Figure **2.24**. This last mechanism was previously described for carbon black like an "onion peeling model" [186].

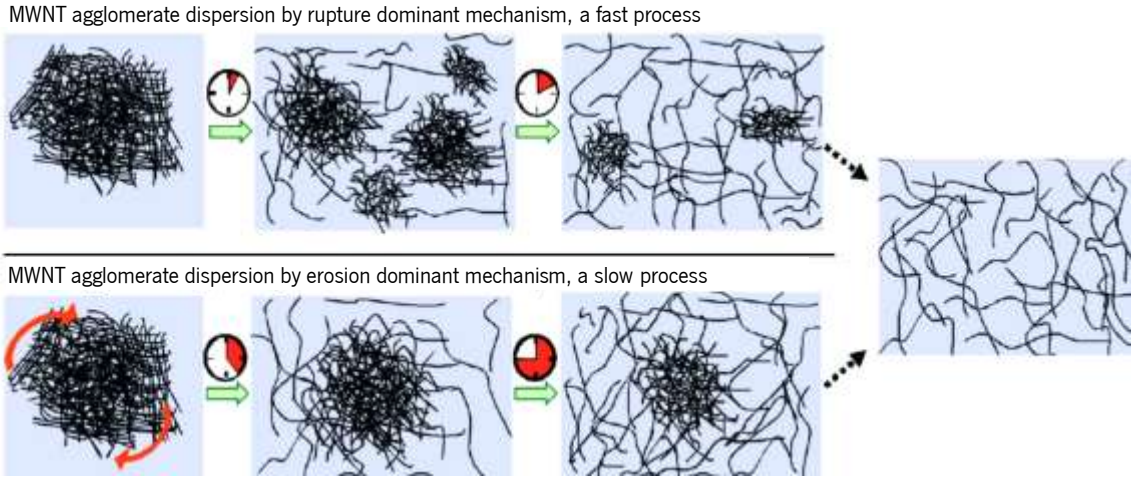

Figure 2.23 - Schematic descriptions of MWNT agglomerate dispersion mechanisms [174].

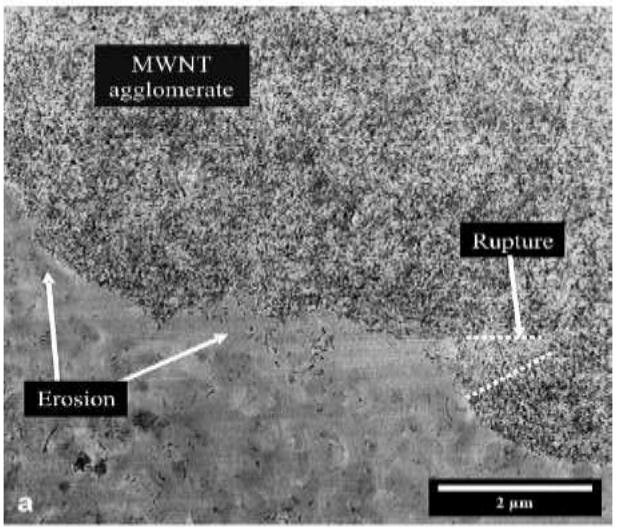

Figure 2.24 - Illustration of rupture and erosion mechanism (dotted lines indicates region of crack propagation) [174].

It was reported that once erosion starts it may progress during long times, while rupture is concluded abruptly.The agglomerates break under shear or tensile stress if the stress applied is greater than the agglomerate strength [187,188].

The dominating mechanism of agglomerate dispersion dependent on the applied shear stress namely on the fragmentation number (Fa) [189]. If Fa is smaller than $Fa_{critical}$, particles undergo dispersion mainly by erosion and if Fa is larger than $Fa_{critical}$, particles undergo dispersion mainly by rupture.
Since the rupture mechanism is fast, causes breakage of the CNT reducing their aspect ratio whereas the erosion mechanism is slow but leads to well infiltrated agglomerates and is not expected to cause damage to the tubes.
Kasaliwal et al. [174] reported that depending on the processing condition, for CNT agglomerates dispersion the two above mechanisms can coexist, however one mechanism may prevail against the other.

Wetting of the CNT by the polymer melt has been acknowledged to be a requirement for good adhesion and depends mainly on the interfacial energy between CNT and wetting liquids and on external nanotube diameter. If the CNT are functionalized, the functional groups on the CNT surface influence the wetting behavior [187,190].

Another important step is the infiltration of the polymer chains into the primary agglomerates. The melt infiltrate the agglomerates reducing the agglomerate strength so CNT may disperse relatively easier. The rate of this step depends on the agglomerate size, smaller agglomerates are fully infiltrated faster [187] and it is faster for low melt viscosities, and thus, lower polymer molecular weights [108]. The best dispersion is achieved at low melt temperatures or high speed where the shear stress applied to the agglomerates is high enough to break them [191]. The infiltration has, next to the applied shear stresses, a big influence on the agglomerate dispersion by rupture and erosion mechanisms.

Less reported but equally relevant is the CNT migration [192] that can be used to disperse the CNT in thermoplastic matrix such as PA and PC using polyethylene (PE) based concentrates with high CNT levels [193]. The CNT migration lies in the much more favourable interaction between nanotubes and PA6 or PC, with a lower interfacial energy, than between nanotubes and PE. The improved dispersion of the CNT leads to significant lower electrical percolation thresholds of these nanocomposites as compared to direct incorporation.

2.5.4. Influence of processing method

The processing conditions for melt mixing were found to have a strong influence on the CNT dispersion.

Andrews et al. [194] have shown for CNT in different matrices that the best dispersion for composites prepared by shear mixing was attained with the highest energy input, achieved either by high rotation speed or long mixing time, but also led to a decrease in CNT length.

A minimum damage for the CNT was obtained at low energy input by Kasaliwal et al. [173] with high melt temperature and high mixing speed that improve the dispersion and lead to composites with low resistivity. Krause et al. [160] indicated that a certain mixing energy is necessary to obtain a state of CNT dispersion leading to low resistivity values but further input of mixing energy increase the electrical resistivity considerably.

The influence of screw configuration, rotation speed and throughput on the residence time and specific mechanical energy (SME) [107], temperature profile [106], feeding conditions [195] in extrusion process and flow type in extruder and modified capillary rheometer [104] in correlation with the resulting macroscopic CNT dispersion was also reported.

For extrusion process, high mixing temperature, low rotation speed and high mixing time were found to be the best conditions to get low electrical volume resistivity values of PA/CNT composites [160]. Altough, Pankaj et al. [196] suggested that an excessive shearing action for longer time duration may lead to breakage/shortening of CNT. The higher mixing temperature had the most dramatic effect in increasing the electrical conductivity.

2.5.5. Carbon nanotube reaglomeration

There are two major issues for an effective dispersion of nanofillers in a polymer: one is to disperse the CNT bundles into individual CNT and the other is to maintain the stable dispersion of CNT. However, during a second processing or shaping step (compression or injection molding, for example) of a composite with well dispersed CNT, it is common to observe that they tend to attract each other due to the Van der Waals forces, leading to reagglomeration, also designed by secondary agglomeration.

The secondary agglomeration leads to re-forming of the CNT agglomerates. Such regions may increase electrical conductivity [187] mainly for samples initially well dispersed and subjected to melt mixing at high temperatures [191]. It may also have the opposite effect, decreasing the conductive of a conductive composite.

Compression also alters the state of CNT dispersion. When well dispersed CNT composites are subject to compression moulding at high temperatures, the polymer melt remains under quiescent conditions

and secondary agglomeration occurs. This may enhance the formation of a conductive network structure [191].

To understand the effect of shear on destruction and build-up of conductive filler networks formed by CNT in PC [197] and in epoxy resin [198], time-resolved measurements of electrical conductivity have been performed. The conductivity shows a tremendous decrease during a short shear deformation applied to the melt with agglomerated CNT while increase for initially well dispersed CNT. Interestingly, samples with 'dispersed' and 'agglomerated' CNT approach the same value of the electrical conductivity after a sufficient time of steady shear deformation (Figure 2.25).

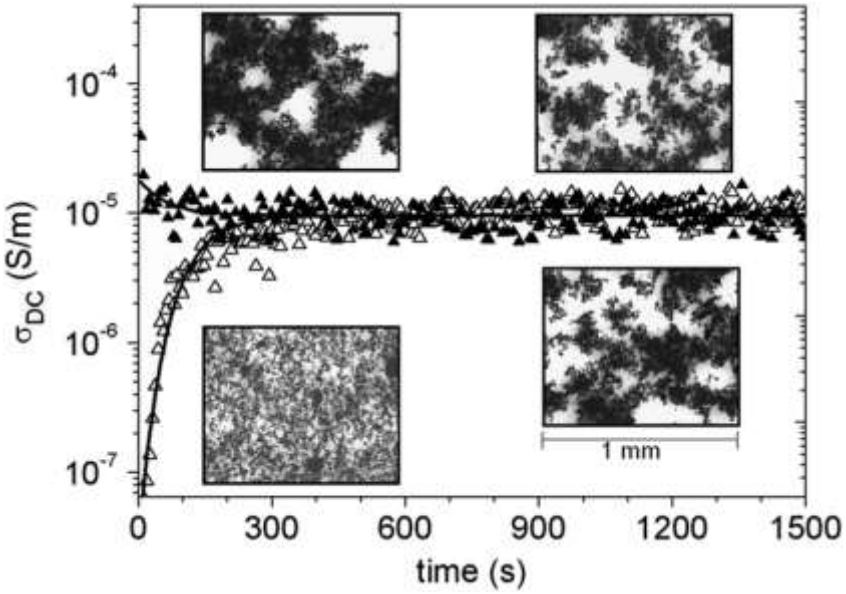

Figure 2.25 - Time dependent DC conductivity of CNT/epoxy suspensions containing 0.1 wt % MWNT at 70 °C at a steady shear rate of 0.5 s^{-1} for two samples with initially dispersed (▲) and agglomerated (△) nanotubes. The inserts show optical micrographs of the initially and final states for both samples [199].

After shearing in the molten state, the CNT are allowed to relax the orientation and re-agglomerate. This conductive filler arrangement can be "frozen". For exemple, after heating the CNT/PC composite above the glass transition temperature of the matrix polymer, *T*g, the secondary agglomeration starts and leads to an increase of conductivity. By cooling below *T*g the conductive filler network is frozen in the glassy polymer matrix [187, 198].

In injection molding this can be done through annealing of the injection moulded parts or by keeping the mould over the melt temperature for some time before cooling it down [200, 201]. The time necessary for reconstruction depends on the mobility of the polymer chains [200]. Their mobility

increases with increasing melt temperature that also favors reagglomeration in both amorphous PC and semicrystalline PA6 nanocomposites [202].

The use functionalization helps to avoid reaglomeration of CNT in epoxy resin at an elevated temperature [203].

2.5.6. Influence of injection and microinjection molding on the CNT dispersion

Most reports correlate the CNT dispersion with electrical behavior of CNT/polymer composites, usually for samples prepared by hot pressing, a simple method and mostly applied at lab scale. This is not the best method to produce conductive polymer composites at industrial scale, that require processing methods such as: injection moulding, spinning, stretching and extrusion.

During these processes the conducting networks are deformed and the influence of processing conditions on the build up or destruction of the conducting network is not comparable to compression molding.

2.5.6.1. CNT orientation

Few reports quantify the dispersion, distribution and orientation of CNT in conventional IM [181]. The dispersion may be analyzed by OM and TEM, and frequently it is correlated with composite electrical resistivity.

In IM and μIM, the polymer is subjected to shear and extensional forces that may induce CNT orientation and will influence the CNT network.

Pujari et al. [204] reported that increasing shear rate decreased the aggregate size and the degree of entanglement while aligning the nanotubes in the flow direction.

These results are in agreement with those reported by Abassi et al. [205] in samples prepared using different processing methods. In compression molded samples CNT were randomly oriented, while in the microinjected dog-bone samples, that featured very high shear values, CNT were well aligned in the longitudinal flow direction.

Depending on injection moulding parameters, mainly for high injection velocity, can be observed a distinct alignment of CNT near the sample surface that is less pronounced across the depth of the sample [181].

Indirect methods, such as X-ray diffraction and Raman spectroscopy may be used to get information about CNT orientation.

CNT orientation was studied in samples prepared through compression molding, IM and μIM.

Abassi et al. [206] reported that compression molded samples show whole rings indicating random orientation while μIM samples show distinct and bright asymmetric arcs, a clear indication of a relatively high level of orientation.

Macropart processed through conventional IM also shows orientation mainly at shear layer. The highest orientation parameter from Hermans orientation function, f_z, was found for μpart due to higher shear rates, faster cooling speeds during μIM and reduced thickness of μpart (Figure 2.26) [121, 207-208].

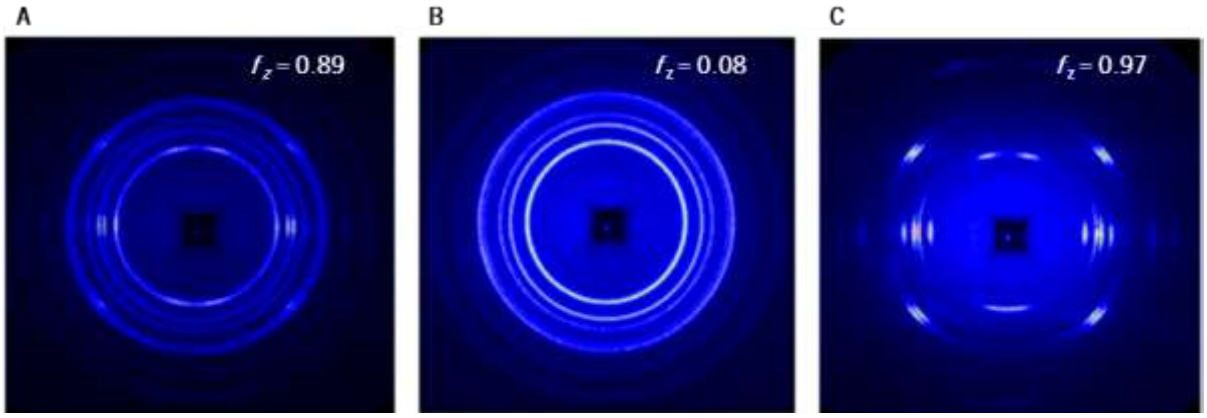

Figure 2.26 - 2D WAXD patterns for two samples: A - the shear layer of macropart; B - the core layer of macropart; C - the μpart. The flow direction is vertical. The orientation parameter was estimated from azimuthal WAXD pattern of (040) reflection. Adapted from [208].

The CNT alignment may also be detectable by Raman Spectroscopy of the composites based on D and G bands [209, 210].

The intensity ratios $D_{\Pi}/D_{\perp}$ and $G_{\Pi}/G_{\perp}$, parallel/perpendicular to the flow direction, were used to assess the degree of nanotube alignment. Values close to unity indicate that there is no preferential nanotube alignment in the PC matrix while higher values indicate well aligned CNT in the longitudinal flow field and were achieved for μIM samples, mainly for tensile bar [205].

The D/G intensity ratio is also used to assess the degree of crystallinity in carbon samples; a lower ratio indicates fewer defects in the crystal structure [211] and a constant value of D/G, in both parallel and perpendicular geometries, means that the CNT structure do not suffer any change [212].

2.5.6.2. Correlation between μIM and electrical conductivity

As shown above, the effect of IM and μIM on CNT alignment is quite different from that observed for extruded and compression molded samples, modifying electrical percolation threshold. A special attention was given to the influence of IM parameters: holding pressure, injection velocity, mold

temperature, melt temperature and shear and elongation flow on the electrical resistivity [201]. It was reported that high melt temperatures [196] and low injection speeds lead to uniform electrical conductivities [213-215]. Furthermore, higher electrical conductivities were found at locations away from the gate [214] or near of the sprue and in the middle of the sample [213]. It was also reported that the electrical condutivity decreased as the length of the flow path increased [213], and vary with part thickness [216].

Since μparts have extremely reduced dimensions, it is reasonable to combine CNT/polymer nanocomposites and μIM because of the low amounts needed of highly priced. In this context, only a few investigations have focused on μIM, a valuable industrial molding technique. As consequence of the stresses induced by combination of shear and elongational flow field and fast cooling, the polymer suffers a complex thermo-mechanical history and changes of the nanotube network can occur due to network orientation, network disruption and orientation of separated tubes [183, 187, 205, 217]. Due to high processing velocities, orientation of molecular chains and CNT occur and remain, during rapid cooling to ensure short cycle times. In addition, skin effects, either by migration of CNT towards the core or by CNT orientation, may be expected, like in conventional injection molding [213]. In this sense, it is crucial to understand the effects on nanotube networks, mainly on the alignment of CNT. This may shift the percolation threshold to higher filler concentrations by decreasing the probability of fiber–fiber contact comparing to other processing methods [205, 218, 219] and the polymer chains may 'insulate' the individual CNT in the contact regions.

The effect of processing conditions on the volume resistivity of the composites prepared by μIM was investigated both through the thickness and in-flow directions [220]. High melt temperature and low injection velocity increase the electrical conductivity in μIM components. Nevertheless, the percolation results are above to that obtained for compression molded samples like reported Abbasi et al. [206].

As can be seen from Figure 2.27, for compression molded samples the percolation threshold is found to be around 3 wt% and 1 wt% of CNT for the PC and PP nanocomposites, respectively, whereas no step-like increase in electrical conductivity was observed for both nanocomposites prepared by μIM.

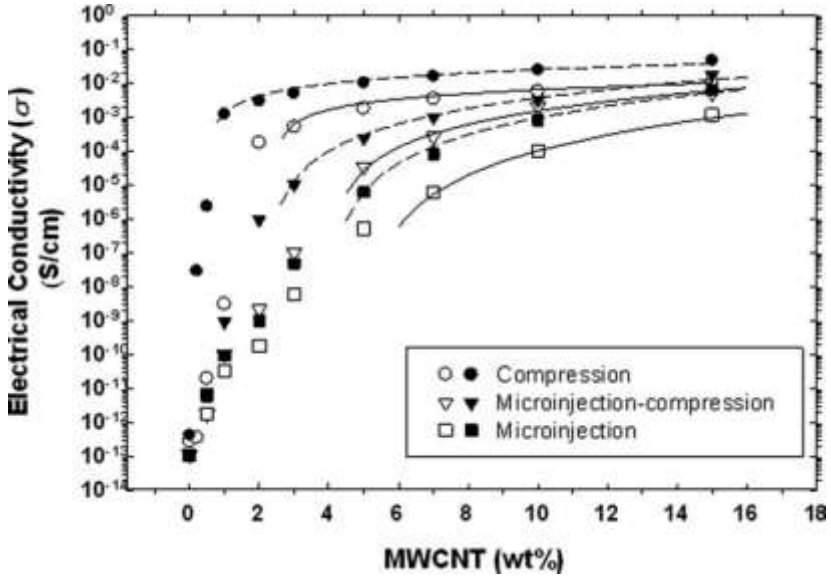

Figure 2.27 - Effect of polymer processing conditions on electrical conductivity and percolation threshold of the PP/MWNT (filled symbols) and PC/MWNT (open symbols) nanocomposites [206].

Interestingly, Abassi et al. [205] reported that the percolation threshold is highly affected by the mold geometry. According to preliminary results revealed that for a dog-bone shaped mold cavity, where the main flow is longitudinal, the percolation threshold is higher (about 9 wt%) than those of the disk shaped cavity samples where the radial flow in the disk shape cavity reduces the effect of high shear rate and less nanotube alignment is achieved.

The results of Abassi et al. [205] and Behnam et al. [221] show that highest conductivities occur for slightly aligned, rather than isotropic CNT and rather than a perfectly aligned nanotube film where the number of conduction paths begins to decrease.

Alig et al. [187] showed that the "skin-core" structure tipical of IM present morphology differences due to competition of destruction and build-up of agglomerates that are correlated with a considerable higher conductivity of the middle layer ('cut') than that of the outer layers.

Furthermore, another relevant parameter is measurement direction [221]. When nanotubes are strongly aligned, the electrical resistivity becomes highly dependent on the measurement direction while for nanotubes with completely random orientation, the value of resistivity is independent of the measurement direction. Extreme orientation reduces the electrical conductivity in all directions, with greatest reductions in the perpendicular direction [183].

2.5.7. Influence of nanotube material and polymer type

The CNT and polymer type were found to influence the CNT dispersion.

Krause et al. [222] studied the dispersability of four different commercially available CNT materials in aqueous surfactant solution. The best dispersabilities were found for Nanocyl™ NC7000 and FutureCarbon CNT-MW. To prepare stable dispersions of Baytubes® C150P or Graphistrength® C100 five times the energy was needed. A similar result was obtained for melt mixed PA 12 with different CNT [223]. The higher stability of Nanocyl™ NC7000 CNT was also reported by Pegel et al. [191] and Krause et al. [224].

It was also shown, that agglomerates of CNT with shorter length or larger outer diameters have less agglomerate strength and can be easier dispersed [225].

Besides the effect of different CNT, the properties of matrix also affect the interactions between CNT and the polymer matrix that play an important role for the dispersion process.

Kasaliwal et al. [225] reported the effect of different thermoplastic matrices on CNT dispersion.

Even though the applied shear stress was the same in all cases, some differences in the agglomerate dispersion were observed probably due to interfacial energy between polymer and CNT.

The dispersion seems to get worse with increasing interfacial energy as can be observed in Figure 2.28 [225].

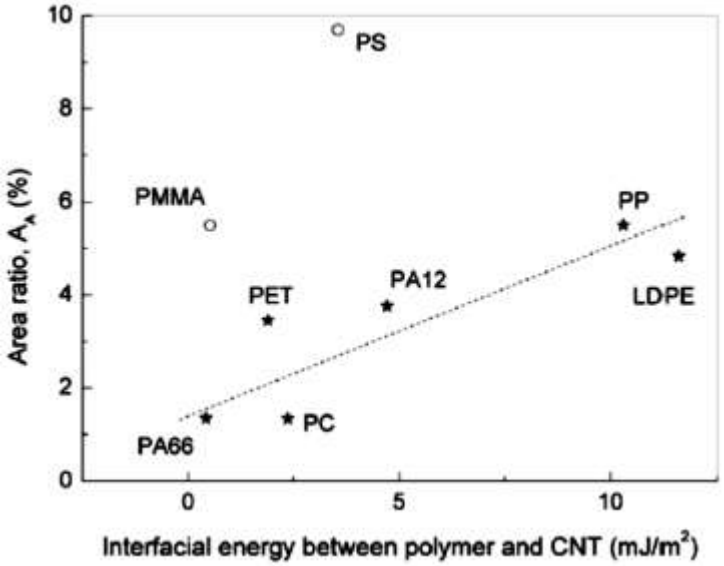

Figure 2.28 - Area ratio of remaining initial CNT agglomerates (A_A) versus interfacial energy between nanotubes and polymer to study the effect of polymer matrix type on dispersion (dashed line is for guiding eyes) [225].

It is also important to consider the crystallinity of matrix since may affect electrical properties [226].

The electrical percolation threshold in CNT/polymer composites is found to be the lowest for thermoset and amorphous thermoplastics while thermoplastic matrices, such as polyamides [159, 227], offer the highest value, also higher than the theoretically predicted percolation threshold considering L/D of CNT [158].

In the case of semi-crystalline thermoplastics, additional complexity arises since crystallites are too organized to allow the introduction of CNT. The dispersion of CNT is significantly affected due to the crystallization induced phase separation or transcrystallinity that can appear onto the surface of CNT [228] and subsequent rejection of CNT by the advancing crystalline fronts disturbing the CNT percolating network [158, 226, 227, 229].

Tjong et al. [230] and Jeon et al. [231] reported that the percolation threshold depend on the crystallization behavior of polymer matrices.

In the case of the present work the cristallinity of the matrix, polyamide 6, a semicristalline polymer, is a relevant factor that should focus our attention.

As mentioned above there are several parametars that affect CNT dispersion and the final composite properties as will be comproved in the next chapters.

3. CHEMICAL FUNCTIONALIZATION OF CARBON NANOTUBES

This chapter is based on the article:

Paiva MC, Simon F, Novais R, Ferreira T, Proença M, Xu W, Besenbacher F. Controlled functionalization of carbon nanotubes by a solvent-free multicomponent approach. *ASC Nano* 2010, *4* (12), 7379-7386.

3.1. Introduction

The chemical inertness of the CNT surface and their highly entangled form hinder the manipulation, interaction or bonding of the CNT to other materials. The chemical modification of the CNT surface is an approach generally used to overcome some of these problems [9, 49, 54, 56].

A widely used covalent functionalization method consists on the CNT acid treatment. The carboxyl groups formed at the surface may react with amines [9], or engaged esterification reactions [239]. Altought, the acid oxidation route lead to CNT structural damage and breakage that affect the large CNT aspect ratio and prejudice further applications. Thus, other functionalization routes should be selected. Reactions involving the direct cycloaddition to the CNT π-electrons were successfully performed under mild conditions leading to little or no CNT breakage. The 1,3-dipolar cycloaddition (DCA) of azomethine ylides is among this class of reactions. It was successfully applied to the functionalization of CNT in 2002, [56] using a dimethyl formamide solution and heating for five days. The reaction time was reduced to one hour using microwaves as energy source under solvent free conditions [75, 240], but was limited to small lab scale production. The effect of microwaves on carbon nanotubes is complex [241], and it is difficult to ensure temperature control and homogeneous reaction conditions while applying this energy source. Using solvent free conditions and heat, the reaction time could be reduced to two hours and the process scaled-up to tens of grams of homogeneously functionalized CNT [76, 77].

The present study reports the functionalization of CNT by the DCA reaction using a specific amino acid, N-benzyloxycarbonylglycine, that allowed the reaction to proceed under solvent free, one-pot conditions. Evidence for the formation of two types of functional groups, namely a pyrrolidine and a benzyl carbamate, was obtained. Their relative concentration could be controlled by adjusting the reaction temperature and time. Thus, the CNT may be prepared with variable surface reactivity, depending on the application envisaged. Furthermore, this was achieved by a simple multicomponent reaction approach that may easily be scaled-up.

3.2. Experimental section

3.2.1. Materials and functionalization method.

The carbon nanotubes used in this study were NC 7000 from Nanocyl. These MWNT were produced by catalytic carbon vapor deposition, and present nominal average dimensions of 9.5 nm diameter and up to 1.5 μm length. The chemical functionalization was performed under solvent-free conditions, as described elsewhere [77]. The amino acid used was N-benzyloxycarbonylglycine (Z-gly-OH), 99%, from Aldrich, and the paraformaldehyde was reagent grade, from Sigma. An ethanolic solution/suspension of Z-gly-OH and paraformaldehyde (1:5 molar ratio) was prepared. A suspension of the CNT in the ethanolic solution was gently heated until the solvent was completely removed, so that a thin layer of Z-gly-OH and paraformaldehyde was deposited on the CNT surface. The solid mixture was heated at different temperatures and times in a round-bottom flask. The reaction temperatures were selected on the basis of previous calorimetric studies reported elsewhere [76]. For studies presented here the reactions were carried out at 180, 210, 230 and 250 °C. The resulting nanotubes were washed several times with ethanol, filtered and dried.

3.2.2. Carbon nanotube analysis.

Thermogravimetric analysis was performed on a Modulated TGA Q500 from TA Instruments. The samples were heated at 10 °C/min under a constant flow of N_2, from room temperature to 800 °C. At least five samples were tested for each functionalization condition.

Scanning Tunneling Microscopy (STM) experiments were performed with a home-built ambient Aarhus STM. The STM images were acquired in the constant current mode. Typical tunneling parameters were 1000-2000 mV and 0.8-1.2 nA for the bias voltage and the tunneling current, respectively, when imaging at the nanometer scale. The samples were prepared by deposition of a few μL of a concentrated solution (or suspension) of the CNT on a highly oriented pyrolytic graphite (HOPG) surface and fast solvent evaporation. The functionalized CNT solutions were prepared with ethanol in the ultrasonic bath during 1 to 4 hours.

All XPS studies were carried out by means of an AXIS ULTRA photoelectron spectrometer (KRATOS ANALYTICAL, Manchester, England). The spectrometer was equipped with a monochromatic Al Kα ($h\cdot\nu$ = 1486.6 eV) X-ray source of 300 W at 15 kV. The kinetic energy of photoelectrons was determined

with a hemispheric analyzer set to pass energy of 160 eV for wide-scan spectra and 20 eV for high-resolution spectra, respectively.

The samples were prepared as loose powder packed beds on an insulating double-sided adhesive tape. In order to avoid electrostatic charging during measurements all samples were irradiated by a low-energy electron source working in combination with a magnetic immersion lens. Later, all recorded peaks were shifted by the same value that was necessary to set the component peak of the graphitic carbon species of the C 1s spectrum to 283.99 eV. This reference value was obtained from analyzing the C 1s spectrum of a mixture made from carbon nanotubes and poly(lactic acid) [244]. One sample was analyzed for each functionalization condition.

Quantitative elemental compositions were determined from peak areas using experimentally determined sensitivity factors and the spectrometer transmission function. Spectrum background was subtracted according to Shirley et al.[242]. The high-resolved spectra were dissected by means of the spectra deconvolution software. Free parameters of the component peaks were: binding energy (BE), height, full width at half maximum and the Gaussian-Lorentzian ratio.

Scanning electron microscopy was performed using a FEI Quanta 400 FEG ESEM equipped with EDAX Genesis X4M.

3.3. Results and discussion

3.3.1. The 1,3-dipolar cycloaddition reaction.

The surface modification of multiwall carbon nanotubes (CNT) by the DCA of azomethine ylides is a widely used reaction that yields a pyrrolidine cycloadduct at the CNT surface. The reaction is easy to set up but the common approach requires the use of a large amount of solvent (dimethyl formamide) and long reaction times (five days) [56]. The approach presented in this work was based on the solvent-free reaction of the α-amino acid, N-benzyloxycarbonylglycine (Z-gly-OH) with paraformaldehyde. Heating the solid reaction mixture produces formaldehyde by thermal decomposition of paraformaldehyde, the formaldehyde diffuses through the melted amino acid forming the 1,3 dipolar species represented in Figure 3.1. The 1,3 dipoles formed in the CNT vicinity may react with the CNT surface through cycloaddition to originate the benzyl carbamate 1. Increasing the temperature leads to

thermal cleavage of the protecting group of the original amine leading to the formation of the pyrrolidine 2 in Figure 3.1, as reported in previous calorimentric and thermogravimetric studies [76]. The product ratio obtained (compounds 1 and 2) may vary with the reaction conditions.

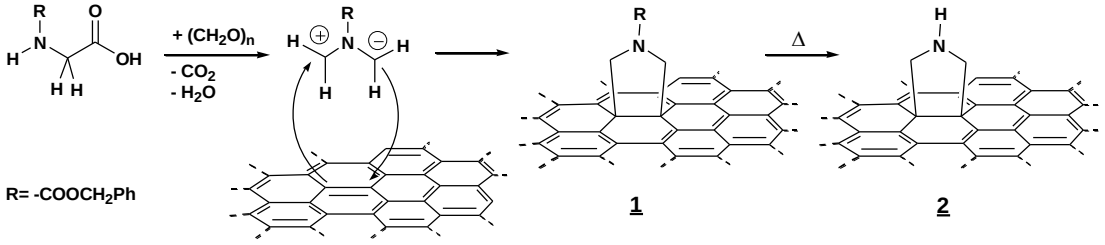

Figure 3.1 - Functionalization of the CNT surface by the 1,3-dipolar cycloaddition reaction of azomethine ylides.

The pyrrolidine formed at the CNT surface is a nucleophilic group that may react further with other molecules. For example, it may react with different polymers if they contain reactive groups such as carbonate or maleic anhydride, establishing a covalent interaction between the CNT and the polymer [77].

In the present work the CNT surface modification through the solvent-free multi component reaction route for the DCA reaction and its dependence on reaction time and temperature, were studied. The degree of CNT functionalization was determined by means of X-ray photoelectron spectroscopy (XPS) as the number of nitrogen atoms bonded to the CNT surface relative to the number of carbon atoms (elemental ratio [N]:[C]). For a given functionalization degree the CNT surface reactivity will depend on the conversion of **1** into **2**. The higher the conversion degree the more reactive will be the CNT surface, and the lower the expected weight loss measured by thermogravimetry (TGA) for a similar yield of N bonded to the CNT surface.

The functionalized CNT were analysed by TGA and XPS. TGA measured the weight loss of the CNT heated from ambient to 800 °C under inert atmosphere, providing the weight of organic functional groups bonded to the CNT surface under the reaction conditions studied. XPS is a technique that analyzes the CNT sample surface within a depth scale of not more than 8 nm. The quantitative determination of the relative number of nitrogen and oxygen atoms bonded to the CNT surface provides evidence for the formation of products **1** and **2** and clarifies the effect of reaction temperature and time on the pyrrolidine yield. The chemical surface composition of the CNT samples and their thermal stability were analyzed and discussed considering that the main reaction products formed were

1 and **2**, resulting from the cycloaddition reaction. Other side reactions or oxidation products were considered negligible. Thus, the increase in oxygen concentration on the CNT surface after functionalization was associated to the presence of the carbamate **1**.

3.3.2. Carbon nanotube surface analysis.

The nanometric scale morphology of the CNT deposited on HOPG surfaces was observed by STM. The STM studies were carried out with the Aarhus STM operated under ambient conditions [243]. The chemical modification along the CNT interrupts the sp^2 C-C network of the highly electrically conductive graphene layer, forming sp^3 C. The smooth, homogeneous surface of the non-functionalized CNT observed under STM turns into an irregular surface with bright protrusions. This observation was discussed previously for the ultra-high vacuum STM analysis of CNT functionalized under similar conditions [244]. Figure 3.2 depicts the STM image of CNT functionalized at 210 °C for 7 hours. The image was obtained under ambient conditions, and shows the hemispheric end-cap of a CNT extremity, supporting the consideration that the 1,3-dipolar cycloaddition method carried out under the described conditions does not physically damage, or break, the CNT structure. The STM imaging conditions (tunnel current and bias voltage) are detailed in the Figure captions.

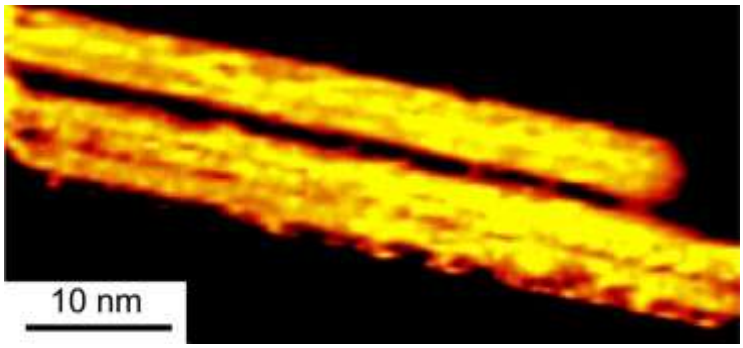

Figure 3.2 - CNT showing evidence of chemical functionalization of the nanotube wall, obtained by ambient STM, scanning condition: It= -1.21 nA, Vt= -831 mV.

Figure 3.3 compares XPS wide-scan spectra of an untreated CNT sample (a) and two CNT samples that where functionalized under different conditions (b) and (c). The untreated sample showed an intense C 1s peak at a binding energy of ca. 284 eV and a small O 1s peak at ca. 532.5 eV. After carrying out the DCA reaction at 180 °C for 3 h (Figure 3.3 b) the intensity of the O 1s peak clearly increased and a considerable amount of nitrogen was detected as N 1s peak at ca. 400 eV. Aluminium (Al 2p and Al 2s peaks) was present as a contamination from the CNT production process. The binding energy of the Al 2p peak is approximately 74.3 eV, which is in agreement with the binding energy of

Al_4C_3. Scanning electron microscopy (SEM) analysis of the CNT showed the presence of contamination debris dispersed in the CNT. Energy dispersive X-ray analysis (EDAX) of the debris identified it as aluminium carbide, Al_4C_3. A small amount of silicon dioxide is also observed. The contamination may originate from alumina used in the Chemical Vapor Deposition (CVD) process that turned into aluminium carbide under the CNT production conditions. The contamination remained after chemical functionalization of the CNT, as illustrated in Figure 3.3.

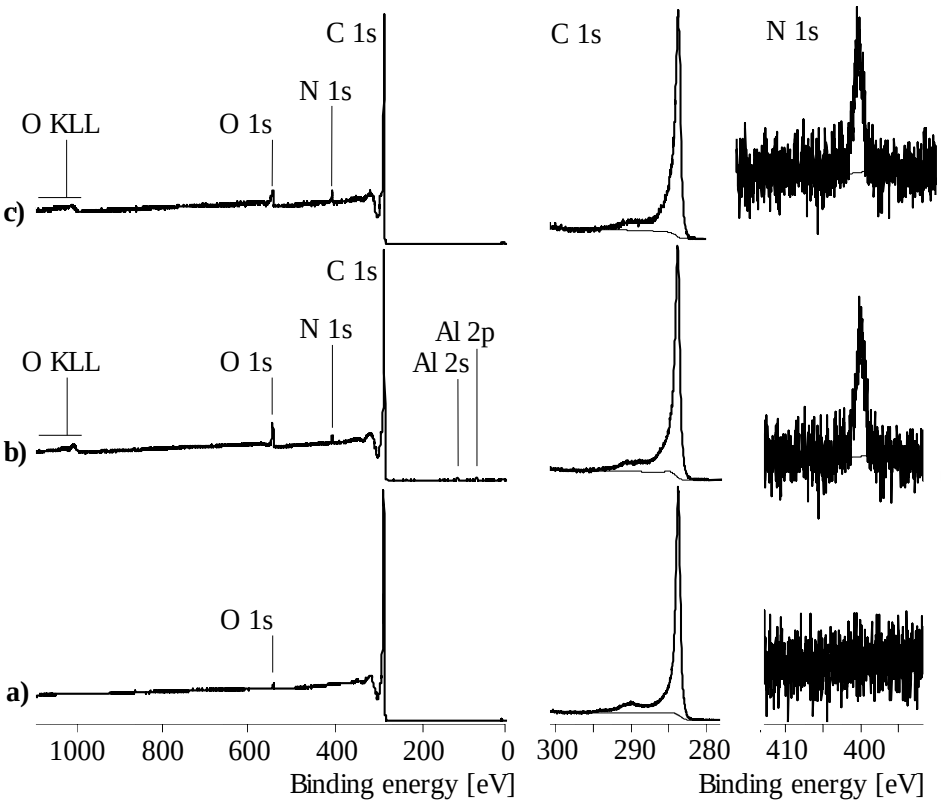

Figure 3.3 - Wide-scan, C 1s and N 1s XPS spectra of an untreated CNT sample (a) and CNT samples after carrying out the DCA reaction at 180 °C for 3 h (b) and at 230 °C for 12 h (c). The abbreviation O KLL designates the oxygen Auger peaks.

SEM images of the Al contamination found in the functionalized CNT (230 °C) obtained with secondary electrons (a), backscattered electrons (b), and identified by EDAX (c) are presented in Figure 3.4.

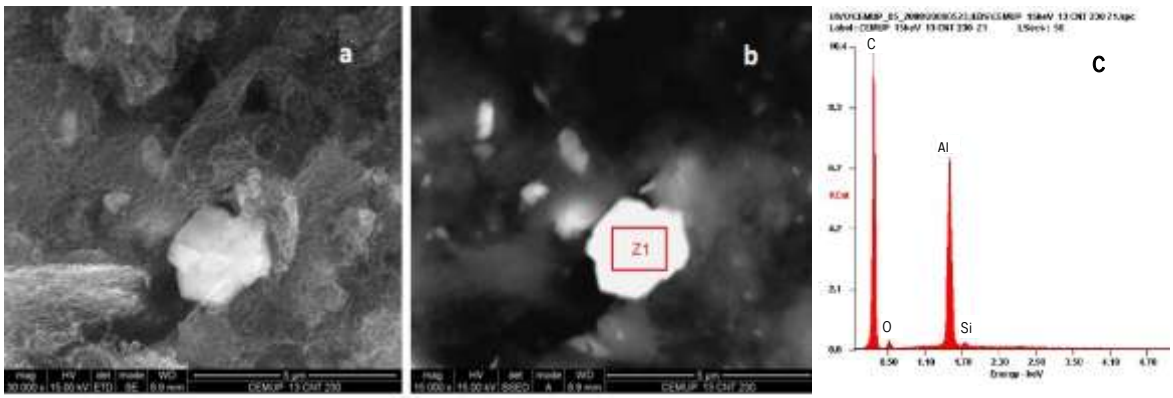

Figure 3.4 - SEM images of CNT functionalized at 230 °C obtained with secondary electrons (a) and backscattered electrons (b). The area Z1 was analyzed by EDAX (c).

The shape of the high-resolution C 1s spectra of untreated and functionalized CNT samples was characterized by a main component peak and a strong tailing to the higher binding energy side (Figure 3.5). The conjugation of the π-electrons in the poly-aromatic CNT lattice result in a high number of linear combinations forming a quasi-continuum of π and π* orbitals. Electron transitions between these orbitals induce wide shake-up peaks that control mainly the C 1s spectra peak shape and complicate the peak analysis, making it difficult to describe the binding states of carbon. For the deconvolution of the C 1s spectra of the functionalized CNT samples, the C 1s spectrum on an untreated CNT sample was used as a reference (Figure 3.5). Deviations from the reference spectrum were interpreted as new binding states of carbon, which were formed during the DCA reaction.

The C 1s spectrum of an untreated CNT sample was deconvoluted into a distinctly asymmetric component peak A showing the sp^2 carbon atoms of the graphite-like CNT lattice. The asymmetric shape arises from the exited vibration states of the carbon atoms. Four shake-up peaks were necessary to obtain an adequate least squares fit. A small, not significant, component peak C, may be associated to C–O bonds on the CNT surface. Its binding energy compares with the typical binding energy for phenol OH groups [245]. After carrying out the DCA reaction at 180 °C for 3 h the C 1s spectra was slightly modified, increasing the tailing region at a binding energy of about 287 eV and 289.5 eV (Figure 3.5b). The reaction coupled a considerable amount of oxygen- and nitrogen-containing groups onto the CNT surface.

Table 3.1 summarizes the atomic ratios of the surface-coupled nitrogen [N]:[C] and oxygen [O]:[C]). The functionalities added to the CNT surface caused three additional component peaks (Figure 4b). Component peak B may be associated to amine-like C–N bonds, the carbon atoms of the Ph–CH_2–O groups contribute to component peak C, and the carbonyl carbon atoms of the N-benzyloxycarbonyl

substituent of the pyrrolidine group were detected as component peak D. The area of component peak B exactly agreed with half of the [N]:[C] ratio determined from the corresponding wide-scan spectrum, indicating that the nitrogen atoms bond to two equivalent carbon atoms bonded to the graphitic lattice. The two component peaks C and D showed the presence of the benzyl carbamate **1** (Figure 3.5). The areas of the two component peaks C and D were equal and nearly half of the area of component peak B, which is consistent with the stoichiometry of product **1**. The intensities and peak positions of the shake-up peaks were not significantly affected.

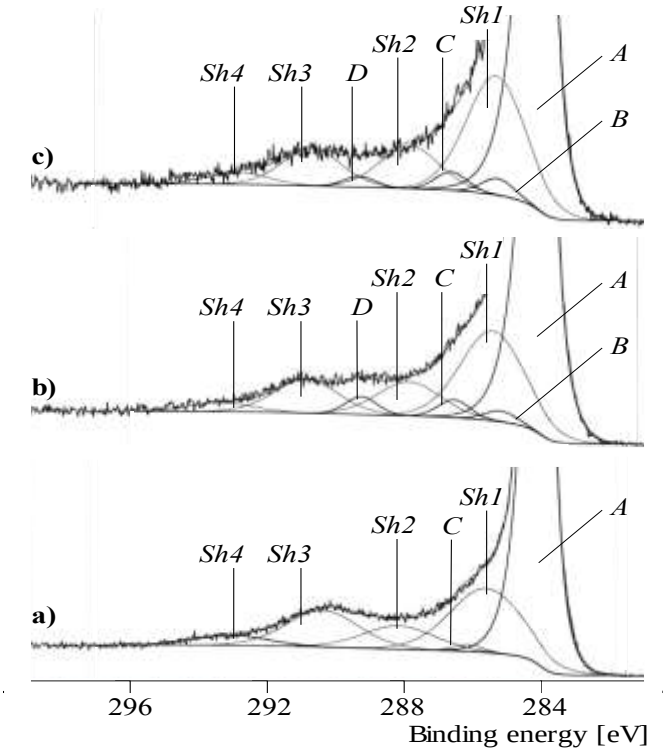

Figure 3.5 - High-resolution C 1s XPS spectra of an untreated CNT sample (a) and CNT samples functionalized at 180 °C for 3 h (b) and at 230 °C for 12 h (c). The intensities of all spectra were normalized using component peak A as reference. In order to visualize the component and shake-up peaks, component peaks A are shown as cut-out. The abbreviations are explained in the text.

The C 1s spectrum of a CNT sample functionalized at 230 °C for 12 h is quite similar to the C 1s spectrum of the sample prepared at 180 °C for 3 h (Figure 3.5c). However, the number of oxygencontaining functional groups added to the CNT surface decreased (Table 3.1).

While the area of component peak B is slightly increased (consistent with the increase of the [N]:[C] ratio), component peak D, arising from the N-substituted pyrrolidine groups, is smaller (Figure 3.5c). Obviously, the increased temperature and the longer reaction time support the thermal decomposition of species **1**, which is converted into its secondary amine form **2** (Figure 3.1).

Normally, the interpretation of the N 1s spectra concerning the binding states of nitrogen is difficult, when it is involved in amino, carbonic acid amide and carbamate groups. Figure 3.6 shows a series of N 1s spectra recorded from CNT functionalized at 180 °C and 230 °C. It can be clearly seen that all N 1s spectra are composed of two component peaks, E and F.

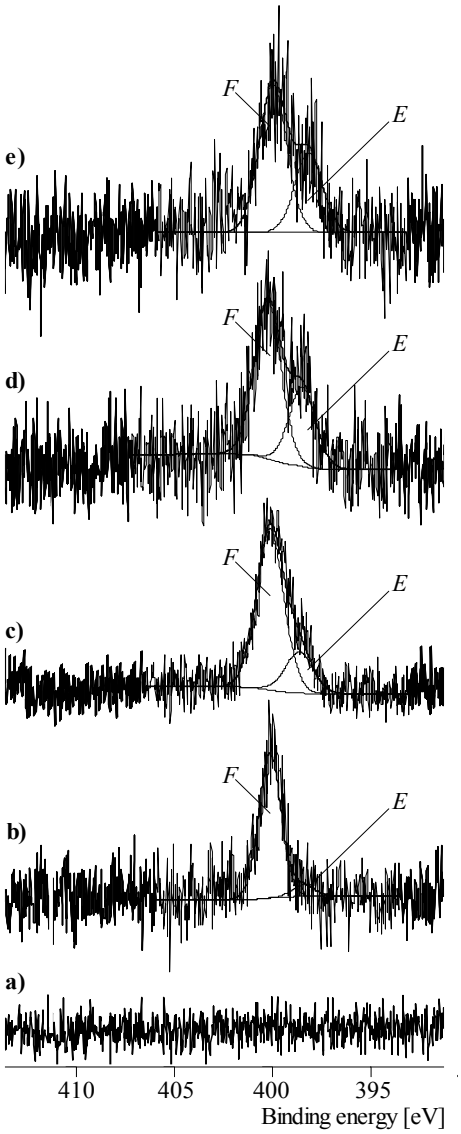

Figure 3.6 - High-resolution N 1s XPS spectra of an untreated CNT sample (a) and CNT samples functionalized at 180 °C for 3 h (b), 230 °C for 3 h (c), 230 °C for 9h (d), and 230 °C for 12h (e).

The binding energy of component peaks F was about 400.8 eV, which is typical for nitrogen atoms in carbamate bonds [246]. The component peaks E, having a lower binding energy of about 399.1 eV, may be assigned to amino groups [245]. The N 1s spectra confirm the success of the 1,3-dipolar cycloaddition reaction carried out on the CNT, and provide quantitative information about the relative proportion of the reaction products 1 (area of component peak F) and 2 (area of component peak E).

As mentioned above, an increase in the reaction temperature leads to the formation of secondary amino groups, which are desirable for subsequent surface modification reactions or the covalent coupling of the CNT to polymer matrices. It was also observed that longer reaction times forced the thermal decomposition of the carbamate groups.

3.3.3. Weight loss analysis.

TGA studies performed under inert atmosphere provided the weight of organic groups bonded to the CNT surface, and the results are presented in Table 3.1 that also reports the XPS results for the atomic concentration of N and O formed at the CNT surface under the reaction conditions studied, measured on the wide scan spectra. The oxygen concentration reported was corrected for traces of inorganic oxides and for the oxygen content of the non-functionalized CNT, corresponding to the oxygen in the functional groups, O_{org}. The XPS data may be analyzed in order to estimate the weight loss, considering that the organic groups attached to the CNT surface are mainly compounds 1 and 2, where the later is formed by thermal decomposition of the former. Within a reasonable approximation, the weight loss estimated from the XPS results for N and O atom concentration should approach the weight loss measured by TGA under inert atmosphere.

Table 3.1 - N and O elemental ratios obtained by XPS, and weight loss results measured by TGA and estimated from the XPS data.

Reaction temperature (°C)	Reaction time (h)	N:C	$(O:C)_{org}$	wt_{TGA} (%)	wt_{XPS} estimated (%)
Non-functionalized MWNT		-	0.008	1.6 ± 0.7	1.9
180	1	0.021	0.028	19.5 ± 2	24.1
	3	0.016	0.030	20.4 ± 2	23.5
	6	0.018	0.034	18.5 ± 1	26.2
210	2	0.020	0.039	25.8 ± 2	29.5
	7	0.028	0.020	22.0 ± 2	22.2
	14	0.020	0.009	20.7 ± 2	13.7
230	3	0.036	0.020	11.1 ± 1	24.9
	9	0.028	0.013	13.7 ± 4	18.5
	12	0.028	0.019	13.4 ± 2	21.7
250	3	0.020	0.014	17 ± 2	16.4
	5	0.019	0.002	14 ± 2	9.6
	7	0.022	0.002	13 ± 2	10.6

Graphic representation of the weight loss variation with reaction time measured by TGA and estimated from XPS is shown in Figure 3.7. In general, the XPS estimated and experimental TGA weight loss results are in good agreement. Deviations between the XPS estimates and the measured TGA values may originate from the heterogeneity of the functionalization of the CNT and the small sample size. Another approximation concerns the CNT oxygen content due to the original oxidation state of the non-functionalized CNT that was considered constant and equal to 0.008, for the O:C elemental ratio. The results concur with the assumption that the DCA reaction is the major event under the reaction conditions described.

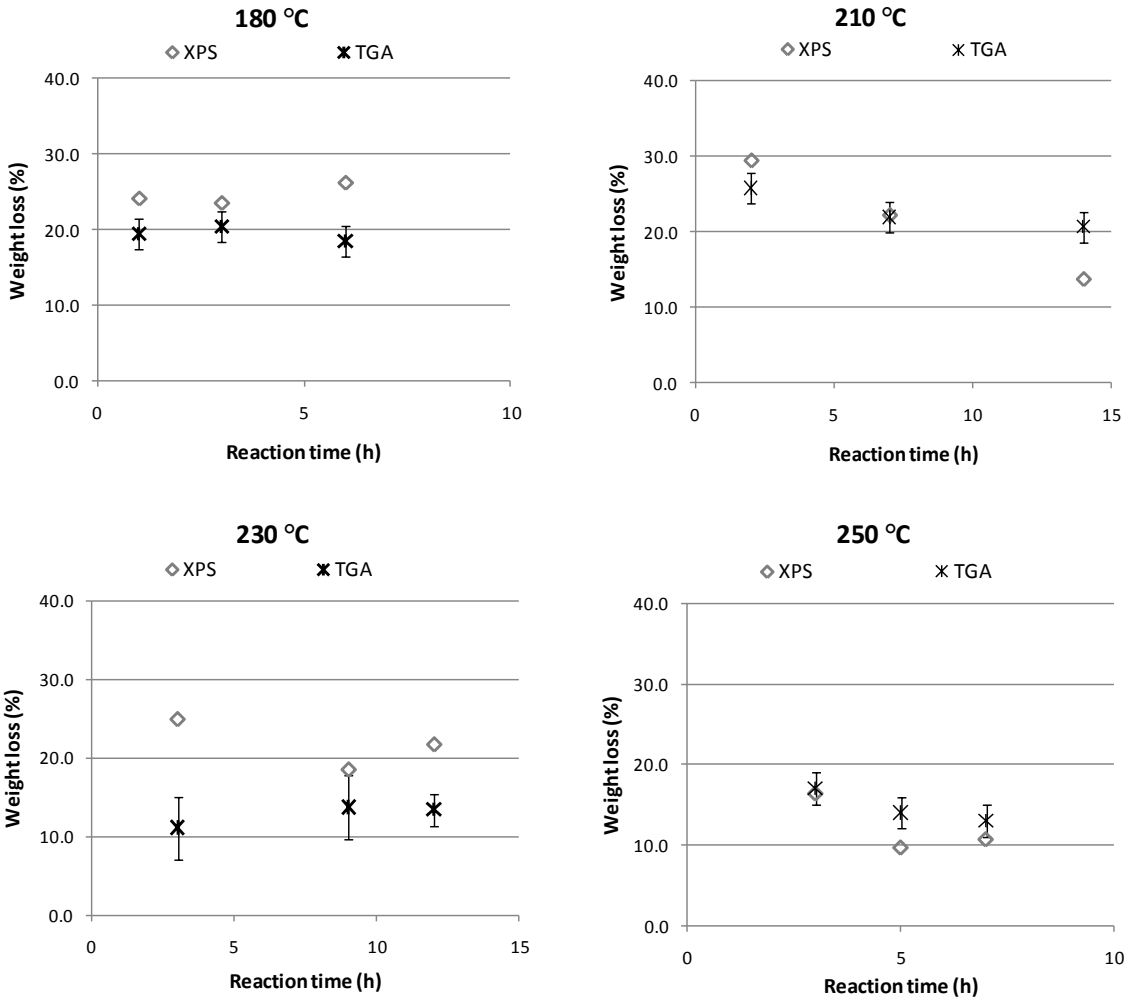

Figure 3.7 - Graphic representation of the weight loss variation with reaction time and temperature, measured by TGA and estimated from XPS results.

3.3.4. Influence of the reaction conditions on surface chemistry.

Previous investigations have shown that the formation of reaction product **1** is an exothermic process [76]. Thus the reaction yield, or the total amount of N that may be bonded to the CNT surface, may vary with the reaction temperature. Plotting the average total amount of nitrogen bonded to the CNT surface and its variation interval for all the samples functionalized at each reaction temperature, an increase in the overall reaction yield was observed from 180 to 230 °C, and a decrease was observed above that temperature, as illustrated in Figure 3.8.

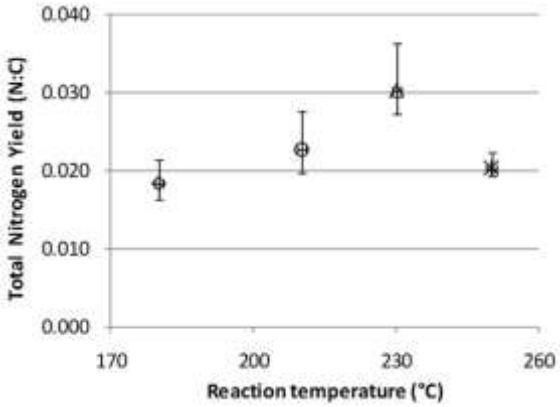

Figure 3.8 - Variation of the total N bonded to the CNT surface with reaction temperature.

The total concentration of N and O bonded to the CNT surface allowed to estimate the concentration of **1** and **2**, and its evolution with reaction time and temperature. Assuming that the protected amine **1** was the only oxygen containing functional group present, the concentration of group **1** will be equal to the atomic concentration $O_{org}/2$, and the N atoms that are not bonded to oxygen atoms will be in the pyrrolidine form, **2**. The variation of the concentration found for the two functional groups with reaction conditions is represented in Figure 3.9.

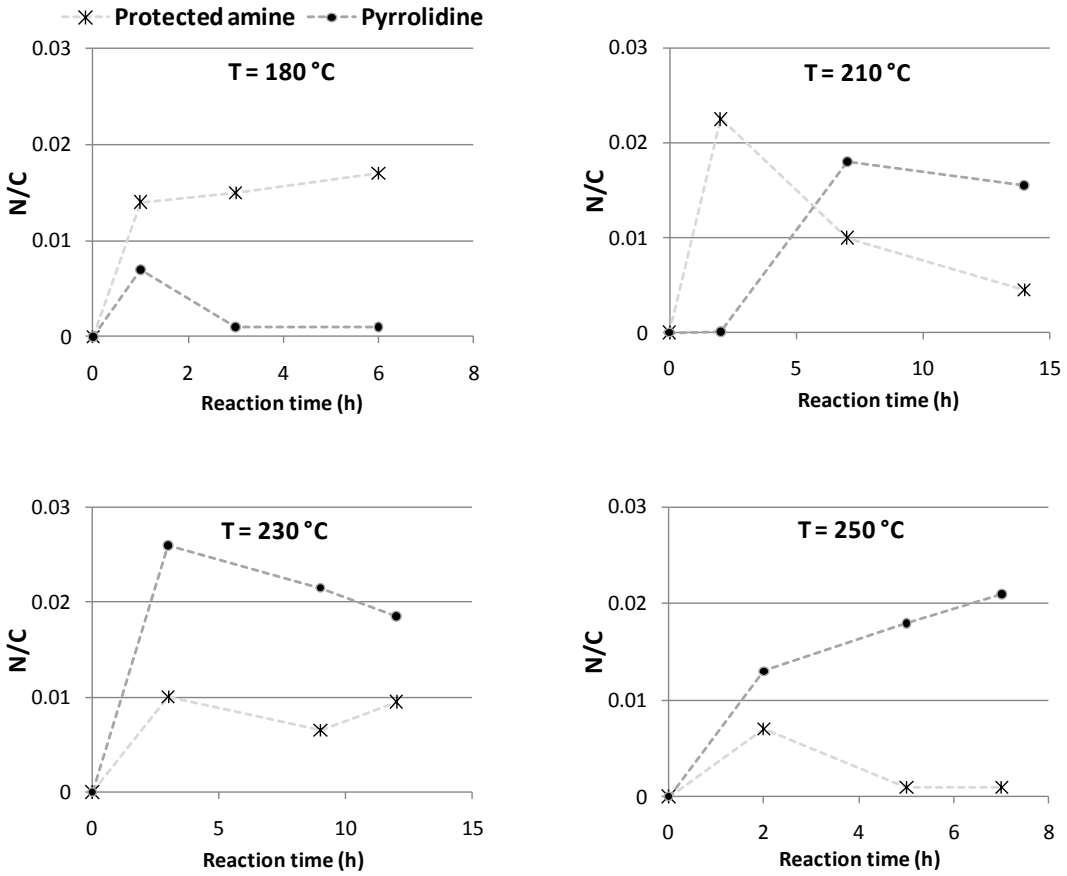

Figure 3.9 - Concentration of the CNT functional groups under different reaction conditions.

The results demonstrate that in the lower temperature range the main product formed was the benzyl carbamate **1**; as the reaction temperature increased, the concentration of the reactive pyrrolidine **2** increased; at 210 °C the concentration of **2** was dominant only for reaction times greater than seven hours; at 230 °C and above the concentration of **2** dominated even for shorter reaction times.

The detailed chemical characterization of the modified CNT surface allows the optimization of the functionalization reaction, and the tailoring of further reactions or physical interactions with other materials.

3.4. Conclusions

The 1,3-dipolar cycloaddition of an azomethine ylide to CNT was carried out using a multi-component reaction approach. The DCA reaction was successful even after a short reaction time (1 hour) and a relatively low reaction temperature (180 °C) under solvent free conditions.

The CNT functionalization reaction was studied in detail by STM, TGA and XPS techniques. The reaction yield in terms of CNT nitrogen content was estimated by XPS and increased with reaction temperature up to 230 °C. A decrease was evident above this temperature. For each temperature, the concentration of nitrogen bonded to the CNT reached a steady state during approximately the first two hours of the reaction.

The major functionalization product obtained with a reaction temperature of 180°C was the benzyl carbamate **1**, while at 230 and 250°C the pyrrolidine **2** was predominant. At 210°C, the reaction time determined the **1** to **2** product ratio.

4. MICROINJECTION MOULDING OF POLYAMIDE 6

This chapter is based on the article:

Ferreira T, Lopes P, Pontes A, Paiva MC. Microinjection Molding of Polyamide 6. *Polym. Adv. Technol.* 2014, *25*, 891–895.

4.1. Introduction

The need for miniaturization and production of plastic micro-parts (μP) are leading to an increasing interest in μIM. This technique provides an adequate solution for the large-scale production of thermoplastic polymer parts [125]. The processing conditions and mold geometries required by this processing technique lead to high shear stress on the polymer melt and to quite different conditions compared to conventional injection molding. Studies reporting the effect of the processing parameters on the properties of the μP produced have been reported in the literature [247, 114]. Conventional injection molding studies have shown that high shear stress applied to the polymer melt induce molecular alignment and may facilitate crystallization, in particular for the polymer close to the cold mold wall, inducing the formation of a skin layer. The inner region, subject to lower stress and slower cooling rate, may develop a different morphology and is referred as the core layer [248]. μIM also induces the formation of a skin-core structure on the molded μP, but the morphology developed may differ from that produced by conventional injection molding [121, 207, 208] due to the higher shear stress and higher cooling rate imposed to the polymer during μIM.

While the features of macroscopic parts and the correlations with processing conditions are well understood, less information is available about μP. It was reported that the degree of crystallinity of the μP and the fraction of oriented polymer layer were larger, and the average size of the crystallites was smaller, for μP compared to parts produced by conventional injection molding [121, 207, 208, 249, 250]. For polypropylene, the crystallinity and molecular orientation was observed to vary with the shear stress induced during μIM [251]. Ito et al. [252] found that higher μIM speed, lower mold temperature and smaller thickness of the mold cavity induced higher molecular orientation while the opposite was reported by Healy et al. [253]. Recently, Meister and Drummer [254] reported that the reduction of mold thickness accelerate the cooling process thus decreasing crystallinity and affecting the μP mechanical properties. Lin et al. [255] pointed out that increasing injection speed, cooling time and mold temperature favoured the increase in the thickness of the core layer and enhanced the yield strength.

The literature reporting the morphology and properties of μIM polymer parts is scarce and, to our knowledge, no work was yet published relative to the μIM of polyamide.

Polyamide 6 (PA6) is a semicrystalline polymer widely used in injection molding and a good candidate for μIM due to its high mechanical performance, good processability and low melt viscosity. Depending

on the crystallization conditions, PA6 may develop two different crystalline phases, α and γ-phase, that convey different properties to the solid polymer. The α-phase is characterized by higher molecular packing and originates higher Young's modulus, while the γ-phase leads to higher ductility [256]. It was reported that slower cooling rate favors the formation of α-phase and that the conversion of γ into α-phase was observed during thermal annealing [257]. Fornes et al. [258] suggested that the skin region of injection molded samples contains mainly the γ-phase due to the rapid cooling of the skin that limits polymer chain mobility while the core region is a mixture of both α and γ-phase. Interestingly, these researchers report that higher levels of crystallinity were observed for injected relative to extruded samples, and in the core relative to the skin, for PA6.

The present work reports the μIM of μP of PA6 and the study of crystallinity and orientation. The morphology developed during μIM was analyzed by optical microscopy, wide angle X-ray diffraction (WAXD) and differential scanning calorimetry (DSC) and compared to that of extruded PA6 that do not experiment significant shear stresses.

4.2. Experimental Section

4.2.1. Materials and Sample Preparation

The polyamide (PA 6) was Badamid®B70 from Bada AG. PA6 was extruded on a miniaturized prototype twin screw extruder (L/D=27) using a profile temperature with a maximum of 255 °C and a die temperature of 235 °C. The same polymer was μIM on a Boy 12 equipment with a 14 mm screw and L/D of 18:1. The temperature profile ranged from 210 to 245 °C in the barrel, and 270 °C at the injection point. Typical μIM parameters were: pressure of 100 bar, injection rate of 240 mm s^{-1} and mold temperature of approximately 100 °C.

PA6 was μIM into tensile bars using a mold with the dog-bone cavity shape and the following dimensions: 21 mm overall length and 6 mm length of the center section, with 1 mm width by 300 μm thickness, as illustrated in Figure 4.1.

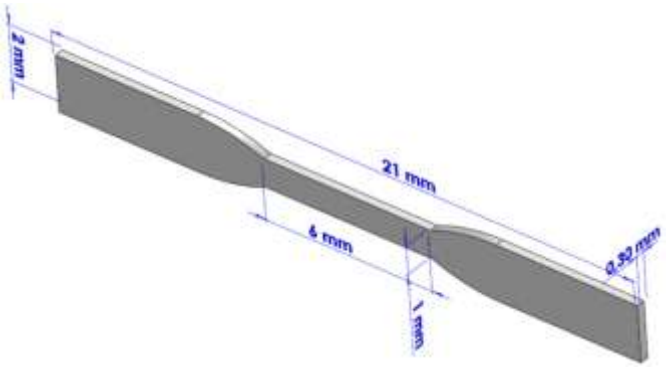

Figure 4.1 - Nominal dimensions of tensile μIM specimens.

4.2.2. Characterization

4.2.2.1. Optical Microscopy

Sections of the extruded and μIM parts were observed under polarized light optical microscopy (PLM). Sections with 5 μm thickness were cut with a microtome along the flow direction of the extruded samples and in the central region of the μP. PLM observations were performed with an Olympus microscope using cross-polarized light, equipped with a Leica digital camera.

4.2.2.2. Differential Scanning Calorimetry

DSC measurements were performed on a Diamond Pyris, under a constant flow of nitrogen and at heating or cooling rates of 10 °C min^{-1}. The μIM and extruded samples were heated to 250 °C and held at that temperature during 2 min, then cooled to 30 °C, held at that temperature for 2 min, and heated a second time from 30 °C to 250 °C.

4.2.2.3. Wide Angle X-ray Diffraction

The X-ray data were collected on a CCD Bruker APEX II at room temperature using graphite monochromatized Mo K_α radiation (λ = 0.0711 nm). Samples were positioned at 70 mm from the CCD detector and the diffraction patterns were acquired using 30 s and 10 s collection time for micro injected and extruded samples respectively.

μIM specimens were mounted vertically, with the sample plane perpendicular to the X-ray beam. The specimens were analyzed across the overall thickness in the center area, as obtained from the μIM, and after fine-polishing with 600 mesh sandpaper to remove a layer of 50-60 μm thickness on each side of the 1 mm wide specimen surface, as illustrated in Figure 4.2a and b. Extruded samples with approximately 500 μm thickness were cut perpendicularly to the extrusion direction (Figure 4.2c) and

fixed in the beam path using tape. Background scattering was acquired and subtracted from the samples scattering patterns. The Bruker files with the 2D scattering patterns where processed using POLAR software [259].

Crystallinity calculations from the integrated intensity profiles were carried out fitting Gaussians to each of the crystalline reflections and to the amorphous scattering. Orientation was calculated at the peaks position based on the intensity azimuthal distribution using POLAR software [259].

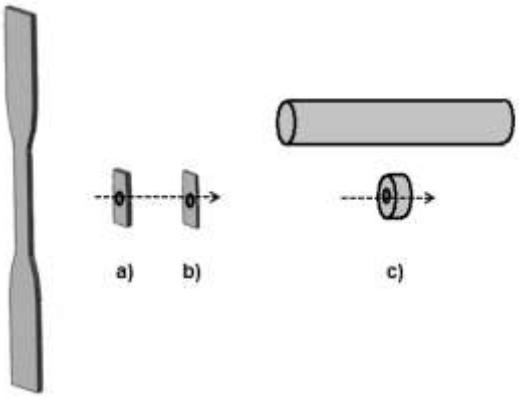

Figure 4.2 - Schematic representation of the samples prepared for WAXD analysis: samples cut from μIM specimens formed by a) the entire thickness and b) the core region, and c) samples cut from the extruded filament. The arrows represent the direction of the X-ray beam.

4.3. Results and Discussion

Figure 4.3 shows micrographs obtained from extruded and μIM samples, from the cross-section of the extruded rod and the longitudinal section (across the thickness) for μP. The extruded sample exhibit a fine-grained layer near the surface, an amorphous layer, and finally a spherulitic layer at the center (Figure 4.3 A and B). The μP (Figure 4.3 C and D) revealed the presence of three distinct regions: a bright skin layer, an isotropic spherulitic region, often referred as ‘‘shear like layer” [121, 208] and a dark region referred as core layer.

The skin layer thickness of the μP is relatively large compared to that of the extruded sample, as observed in Figure 4.3. The brightness of this skin layer observed under polarized light result from molecular orientation induced by the μIM conditions, namely high shear and rapid cooling. These

thermomechanical conditions hinder chain relaxation and favor the alignment of polymer chains within the flow, resulting in orientation as observed on the skin region of the μP.

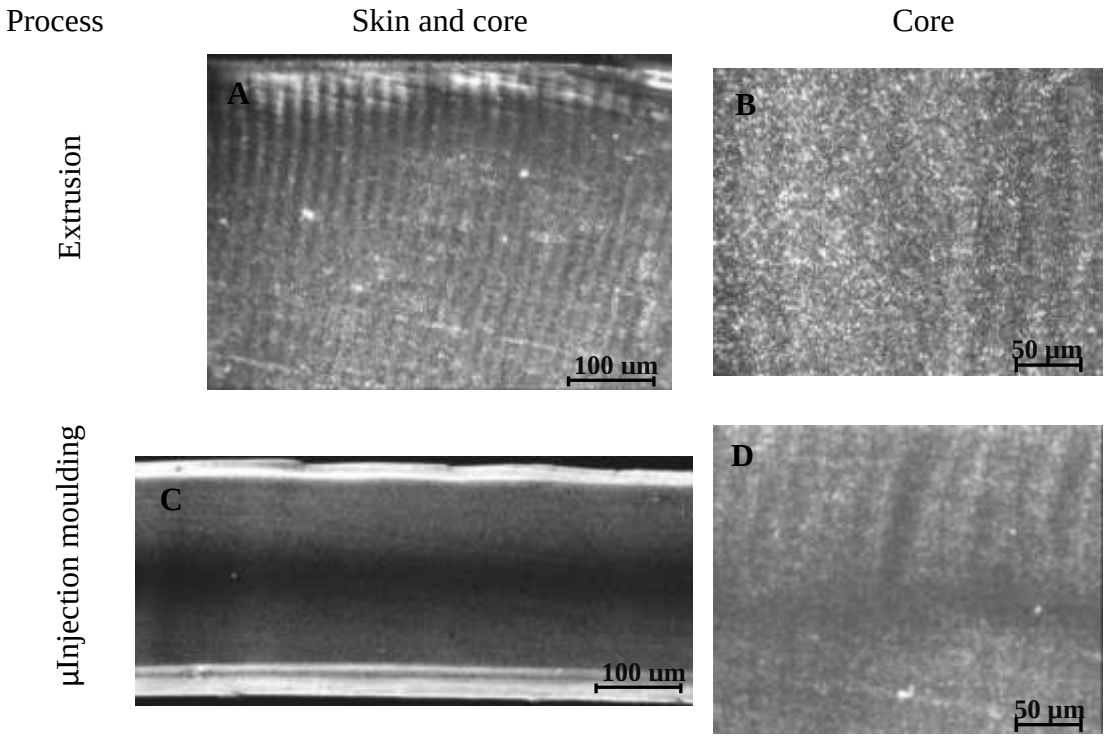

Figure 4.3 - Optical micrographs obtained by PLM for polymer sections along the flow direction for extruded and μIM parts both with the central region at relative higher magnification.

The parts produced by μIM have a high surface/volume ratio relative to parts produced by other melt processing techniques, leading to faster cooling through the volume in the μP [260] which may induce specific structure development. The thermomechanical constraints imposed on the polymer during processing may affect the crystallization, i.e. nucleation and growth rates of crystallites [249]. Thus, it is important to study the relation between the processing conditions and crystallinity, and evaluate the relative content of α and γ-phases, which may affect the material's properties.

The DSC thermograms of extruded and μIM PA6 are presented in Figure 4.4, depicting the thermal response of the samples during heating above the melting temperature, cooling, and heating a second time.

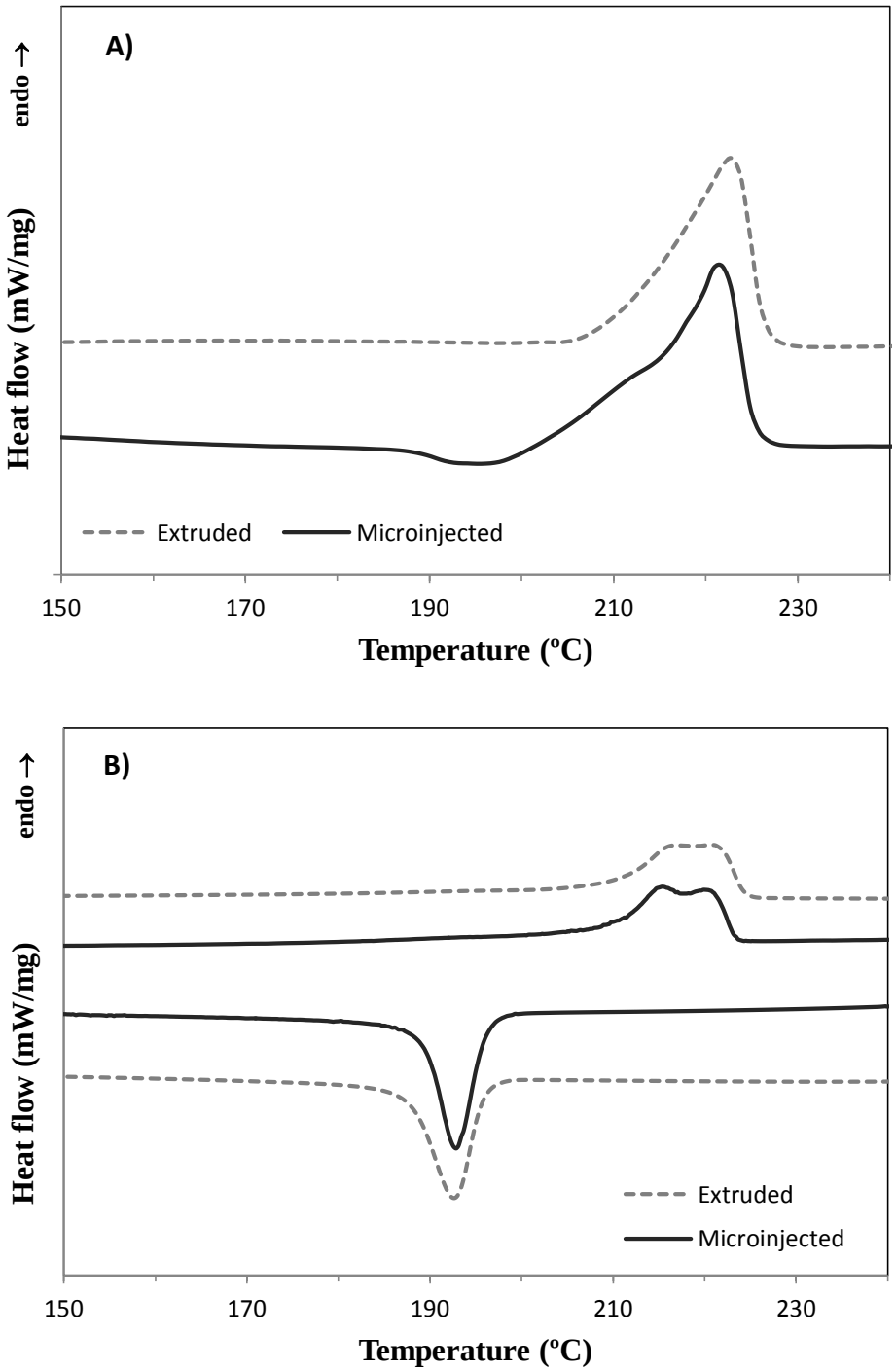

Figure 4.4 - DSC thermograms of extruded (light lines) and μIM (dark lines) PA6; A) first heating and B) cooling and second heating.

The peak observed during the first heating of the extruded part, Figure 4.4 A), is sharper than the corresponding peak of the μP that presents a shoulder on the lower temperature side. The temperature of maximum heat flow remains approximately constant for extruded and μIM samples, but the changes

on the heat flow signal begin at lower temperature for the μIM parts. This latter effect may be assigned to secondary crystallization occurring around 195°C. This crystallization peak has been attributed to the presence of nano crystals formed under the μIM shear stresses, which crystallize during the first DSC scan [261]. It was also associated to the transformation from the γ-form to the α-form during the DSC heating scan [262].

The temperatures of highest heat flow during the melting for the first and second heating ($T_{m1,}$ and T_{m2}), the crystallization temperature during the cooling (T_c) and the heat of fusion calculated from the first heating (ΔH_f) obtained by DSC are summarized in Table 4.1. The degree of crystallinity (χ_c) for PA6 was evaluated using the following relation, $\chi_c(\%) = \frac{\Delta H_f}{\Delta H_f^0} \times 100$, where ΔH_f is the heat of fusion measured for the sample (Jg^{-1}), and ΔH_f^0 is 188 Jg^{-1} [263].

Table 4.1 - Crystallization and melting parameters of extruded and μIM PA6 parts.

Sample	T_{m1} (°C)	T_c (°C)	T_{m2} (°C)	ΔH_{f1}(J/g)	χ_{c1}(%)
Extruded	222.9	192.6	217.0 221.0	57.8	30.7
μIM	222.2	192.2	215.2 220.0	47.6	25.5

During the second heating, two peaks (T_{m2}) can be observed, the lower temperature peak, near 215°C, corresponds to the melting of the γ-phase, and the higher temperature peak, near 220°C, relates to the melting of the α-phase, as suggested by several researchers [258, 264, 265]. The crystallization thermograms for PA6 are presented in Figure 4.4 B), showing a single crystallization peak (T_c) with a similar shape for both samples, observed at 192°C.

The overall degree of crystallinity measured for the μP is similar, but lower compared to that of the extruded sample. The opposite result was reported for conventional injection molded bars compared to extruded pellets [258].

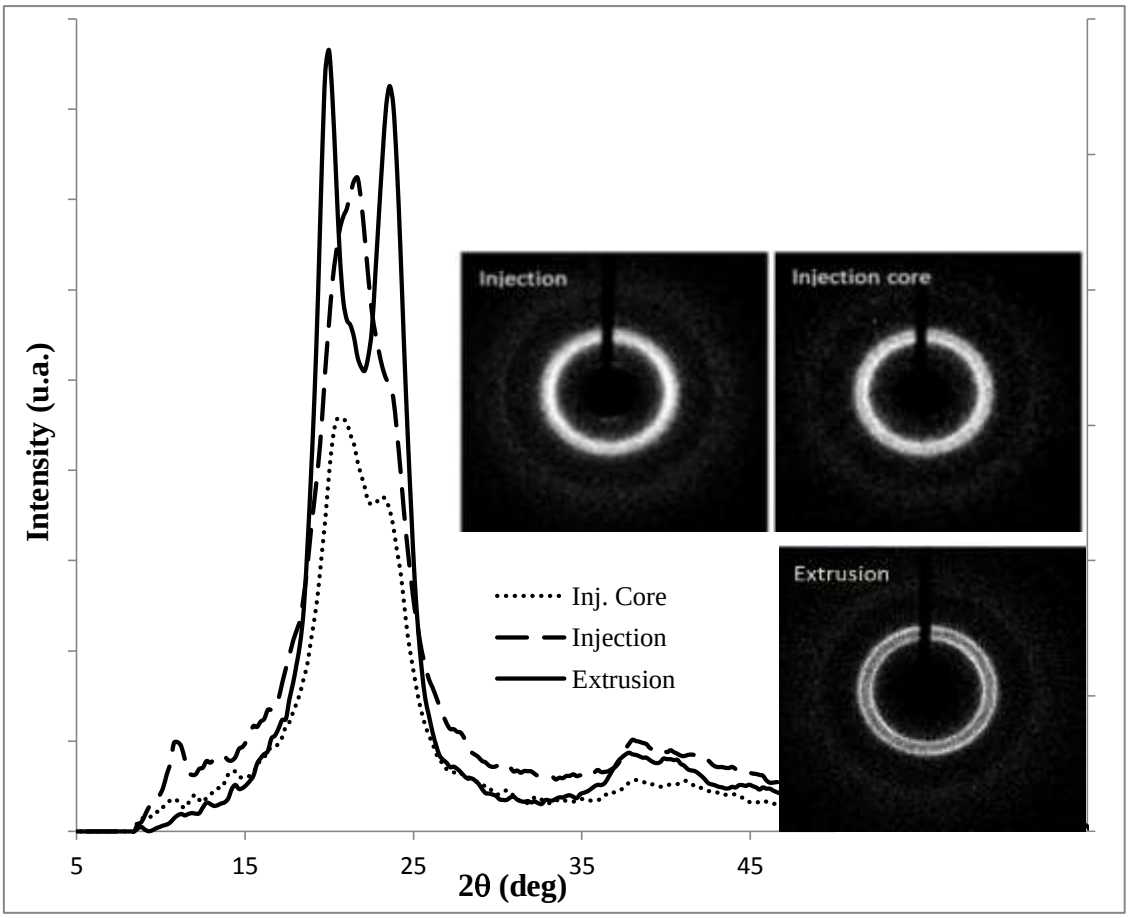

Figure 4.5 - WAXD patterns of extruded and μIM parts. For the scattering patterns, the flow direction corresponds to the perpendicular direction to the page.

The 2D WAXD scattering patterns and corresponding integrated intensity profiles are presented in Figure 4.5. The integrated intensity profiles reveal the presence of both α and γ phases of the PA6. Figure 4.6 presents the crystallinity results, the individual contribution of the α and γ-phases, and include the crystallinity measured by DSC. According to the WAXD results, the γ-phase is most abundant in the μP samples, whole and core, when compared to the extruded sample. The WAXD results also show that the μP presented slightly higher crystallinity in the core region compared to the overall sample indicating that the skin region is less crystalline. The amount of γ-phase is larger in the whole μIM sample than in the core, meaning that it predominates in the skin region. The crystallinity calculated from the WAXD results for the core region show equal contributions of α and γ-phases. The extruded samples present higher overall crystallinity compared to the μP. For these samples, the major contribution for crystallinity originates from the α-phase. This reflects the higher cooling rates (hence lower crystallization temperatures) and the high stress levels generated during μIM. These results are

in agreement with the observation that high temperature crystallization or low cooling rates promote the formation of α form, while rapid cooling and low temperature crystallization leads to γ form of PA6 [257, 258].

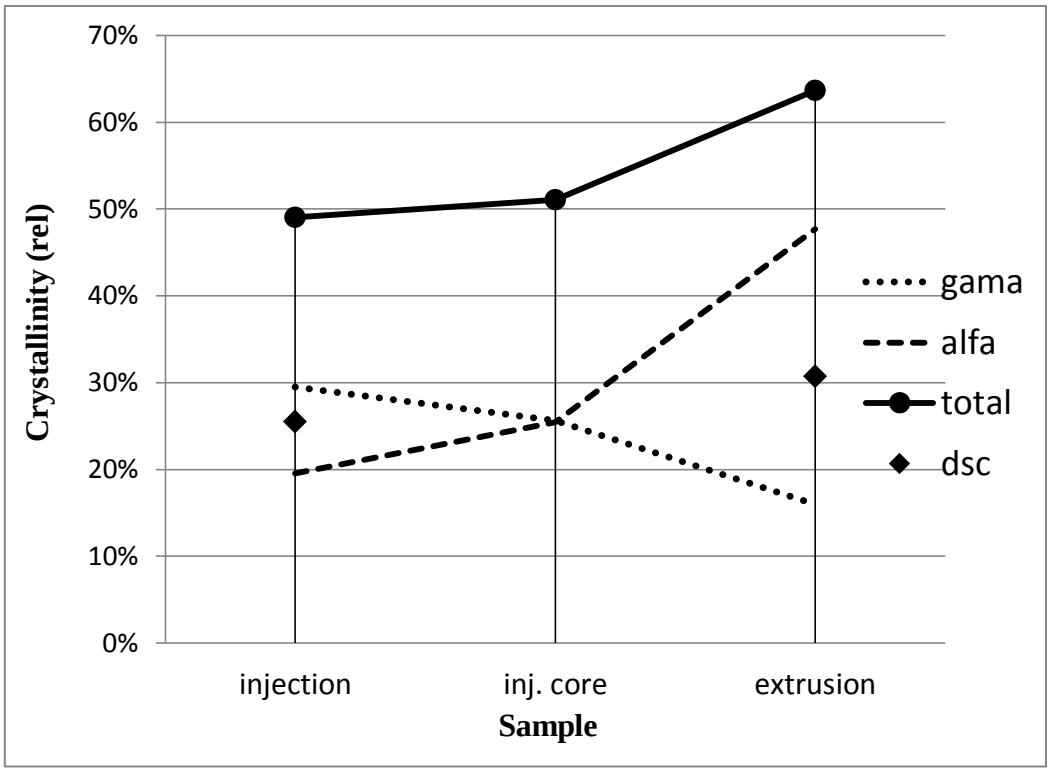

Figure 4.6 - Crystallinity and α and γ-phase content data obtained from fitting of WAXD patterns of extruded and μ-parts.

The crystallinity values obtained by WAXD are larger compared to those obtained by DSC. This trend is usually observed since the DSC technique requires the melting of the sample, while WAXD analysis is performed on the solid sample, providing a description of its crystalline structure without any perturbation [121, 208]. DSC experiments provide valuable information about the melting and crystallization behavior of PA6, while WAXD is adequate to evaluate the crystal structures and their orientation.

The collected 2D scattering patterns, Figure 4.5 insets, illustrate some degree of orientation on the μP, and almost isotropic patterns for the μP core and extruded samples, as also observed by PLM.

The orientation of the crystalline reflections was determined using POLAR software performing the analysis on the 2D intensity data. The measured intensities where decomposed in two components, one isotropic and another anisotropic. The Hermans orientation factors, f_z, [266] calculated on the anisotropic intensity component, are presented in Table 4.2 for the μP (injection), its core region (inj.

core) and for the extruded sample (extrusion). Some orientation was observed on the μP, significantly reduced in the core region, and almost absent in the extruded samples. Thus, it may be concluded that orientation effects in the μIM specimens are mainly observed in the skin region.

Table 4.2 - Hermans orientation factors calculated for μP and extruded PA6 samples.

Sample	f_z^*	Peak
Injection	-0.202	γ peak @ 21.67° (2θ)
Inj. core	-0.117	γ peak @ 21.67° (2θ)
Extrusion	-0.070	α peak @ 19.97° (2θ)

*The Hermans orientation factor ranges from -0.5 to 1.0, corresponding to fully oriented crystalline planes, perpendicular and parallel to the reference axis, respectively. A value of zero corresponds to random orientation.

4.4. Conclusions

PA6 was processed by melt extrusion and microinjection molding. The former process induces relatively low shear stress on the polymer melt, and the material is released directly into ambient conditions. The later process requires high injection speed, inducing high shear stress on the polymer melt and leading to large thermal gradient due to the small thickness of the mold cavity. The samples obtained by both melt processing methods were studied to identify differences in their morphology and structure induced by the melt processing methods.

WAXD and DSC were used to characterize the PA6 crystalline morphology. It was observed that the skin region of the μP contains mostly γ crystalline form, according to Fornes et al. [258] and shows considerable molecular orientation, as confirmed by polarized light optical microscopy. The core region of the μP presented equal contribution of both α and γ crystalline forms, and low molecular orientation was detected. The extruded material presented a larger contribution of the α form, and almost no molecular orientation was observed.

Important differences in the polymer structure, in particular the degree and type of crystallinity, and formation of a large fraction of oriented layer, occur after μIM, compared to extrusion processing. The high shear rates due to micro dimensions of the mold cavity and high injection speeds during μIM may induce polymer chain alignment. This effect, coupled with high cooling rate, particularly at the mold surface, promote nucleation and flow-induced crystallization, resulting in a greater number of oriented smaller crystals as observed by PLM [121].

5. CRYSTALLIZATION BEHAVIOR OF MICROINJECTED CARBON NANOTUBES/ POLYAMIDE 6 NANOCOMPOSITES

This chapter is based on the article:

Ferreira T, Lopes P, Pontes A, Paiva MC. Crystallization Behavior of Microinjected CNT/PA 6 Nanocomposites *In preparation.*

5.1. Introduction

CNT/polymer composites have attracted the attention of the research and industrial communities. The excellent electrical/thermal conductivity and high mechanical strength of CNT coupled with their nanoscale size and low density classify them as ideal one-dimensional polymer reinforcement, to generate nanocomposites with a wide range of potential applications [39, 43, 169, 267].

With the increasing demand for small and even micro scale parts for CNT/polymer composites, μIM became particularly desirable because of its large scale production capability and low production cost.

During μIM the polymer melt is subject to a complex thermo-mechanical history due to high injection pressure, high shear, high cooling rates and very short cycle times that may affect the properties of the microparts (μP) [125,129].

However, during μIM of CNT/polymer nanocomposites, the properties of the matrix may be changed not only by the processing itself but also due to the presence of the CNT that exhibit very large surface area.

Polyamide 6 (PA6), a semicrystalline polymer, exhibits high mechanical performance, good processability and chemical resistance and is widely used in industry. Its physical and mechanical properties depend considerably on the crystalline structure and on the degree of crystallinity [256]. The PA6 displays polymorphism, as it may crystalize in two different forms, the α- and γ-phase. In general, γ-phase is formed during fast cooling and low temperature crystallization while slow cooling promotes α-phase [257, 268].

Few studies are reported in the literature concerning the crystallization behavior of PA reinforced with CNT [167, 233, 270]. These nanocomposites seem to present different characteristics from those incorporating clays, the latter favoring the formation of the γ-phase [258, 269]. It is reported that the CNT may act as nucleation agents, favoring the formation of the α-phase of PA6, inducing an increase in the crystallization degree [167, 233, 270], and the development of a second crystallization peak in nanocomposites [163, 233, 257]. Coleman et al. report that a crystalline layer forms around the nanotubes that, combined with a good interfacial adhesion, enhances the mechanical properties [271]. However, other works report that high CNT concentrations, mainly with functionalized CNT (f-

CNT) with a stronger compatibility with PA6 [46, 50], hinder the mobility of PA6 chains, delay the crystal growth and thus lead to the decrease of crystallinity relative to neat PA6 [164, 234, 272, 273]. Concerning μIM, limited literature is found about the crystalline characteristics of μP of neat polymers [208, 251, 274, 275] and polymer/CNT nanocomposites [164, 273]. The variation of the degree of crystallinity of PA6/CNT nanocomposites prepared by μIM is negligible compared with PA6 matrix. Only recently, Abassi et al. [206] reported the effect of the processing method on the crystallinity of nanocomposites and concluded that compression, μIM and μIM-compression do not dramatically influence the crystallinity.

The present work focuses the study of extruded and μIM PA6/CNT nanocomposites with pristine and functionalized CNT. The production of these nanocomposites, the CNT dispersion in PA6, their mechanical and physical characterization, was reported previously [276]. Here we report a detailed study of the PA6 morphology developed in the nanocomposites with low and high CNT and f-CNT content (1 and 4.5 wt.%, respectively), after extrusion and after μIM. The nanocomposites were analyzed by differential scanning calorimetry (DSC) and wide angle X-ray diffraction (WAXD).

5.2. Experimental section

5.2.1. Materials and sample preparation

Polyamide 6 (PA6) used in this study was Badamid® LA70 K. The CNT were functionalized by the 1,3 dipolar cycloaddition reaction, as reported in previous chapter [277]. The PA6/CNT composites containing 1 and 4.5 wt% of as received CNT (p-CNT) and f-CNT (designated P1, F1, P4.5 and F4.5) were prepared via melt-blending using a prototype mini twin-screw extruder. The neat PA6 was also extruded under similar conditions. The extruded rod was cooled in water at room temperature and then pelletized. Finally, the pelletized and dried extrudate was μIM as described in previous work [276] to form tensile test-shaped bars with 300 μm thickness, using a Boy 12 equipment.

5.2.2. Composite characterization

5.2.2.1. Morphology

Samples of extruded and μIM PA6/p-CNT and PA6/f-CNT nanocomposites were cryogenically fractured under liquid nitrogen. The fractured surfaces were sputtered with a thin layer of palladium-gold and observed by scanning electron microscopy (SEM) on a FEI Quanta 400 FEG ESEM.

5.2.2.2. Differential scanning calorimetry

DSC was used to study the crystallization behavior of PA6/CNT nanocomposites. DSC analysis was performed under nitrogen flow in the temperature range of 30-250 °C in a Perkin Elmer Diamond Pyris equipment. The μIM samples were cut in the central region of the tensile specimen. Samples were heated to 250 °C and held there for 2 min to remove any previous thermal history, then cooled from the melt to 30°C, held for 2 min and a second heating was carried out from 30°C to 250°C. The scanning rates for heating and cooling during DSC measurements were set at 10 °C min^{-1}.

5.2.2.3. Wide angle X-ray diffraction

XRD patterns were recorded using a CCD Bruker APEX II using graphite monochromatized Mo K_α radiation (λ = 0.0711 nm).

μIM specimens from samples designed PA, P1, F1, P4.5 and F4.5 were mounted vertically and analyzed across the overall thickness in the center area. Additionally, μIM specimens of the same samples were fine-polished with 600 mesh sandpaper to remove a layer of 50-60 μm thickness, the skin layer, on each side of the 1 mm wide specimen surface, these samples are referred as Inj. core. Extruded samples with the same composition as above, with approximately 500 μm thickness were cut perpendicularly to the extrusion direction and fixed in the beam path using tape as illustrated previously in Figure 4.2.

Background scattering was acquired and subtracted from the samples scattering patterns. The sample plane was fixed perpendicular to the X-ray beam and positioned at 70 mm from the CCD detector. The diffraction patterns were acquired using 30 s and 10 s collection time for micro injected and extruded samples respectively.

All data were recorded in transmission mode. From the XRD data, quantitative evaluations of the contents of the two crystalline forms were obtained by the curve fitting of the integrated intensity profiles by Gaussian functions, two for the α phase, two for the γ phase, and one for the amorphous halo, to calculate the area of each peak.

Orientation was calculated at the peaks position based on the intensity azimuthal distribution using POLAR software [259].

5.3. Results and Discussion

5.3.1. Dispersion of CNT in PA6

Figure 5.1 presents SEM images of cryo-fractured nanocomposite surfaces. The white-dot regions represent the ends of nanotubes that were pulled out of the PA6 matrix. The PA6/f-CNT interface appears to be better than PA6/p-CNT, considering the shorter nanotube pull-out length, regardless of CNT amount. Comparison of extruded and μIM nanocomposites, it appears that the μIM improved the CNT dispersion, as already reported [276].

5.3.2. Differential scanning calorimetry

In order to investigate the effect of p-CNT and f-CNT on the crystallization and melting behavior of PA6 processed with different methods and at different CNT contents, the composites obtained were analyzed by DSC.

The temperatures of highest heat flow during the melting for the first and second heating (T_{m1} and T_{m2}), the crystallization temperature (T_c), the enthalpy of fusion for first and second heating (ΔH_{f1} and ΔH_{f2}) were measured from the DSC scans. In order to estimate the degree of crystallinity (χ_c) for PA6/CNT nanocomposites, the equation for the polymer degree of crystallinity was corrected accounting for the CNT weight fraction, as represented in equation 1.

$$\chi_c(\%) = \frac{\Delta H_f}{(1-\phi)\Delta H_f^0} \times 100 \quad (1)$$

Where ϕ is the weight fraction of CNTs in the composite, ΔH_f is the heat of fusion of the analyzed sample (J/g), and ΔH_f^0 value of 188 Jg^{-1} was used for PA6 [263]. This data is presented in Table 5.1.

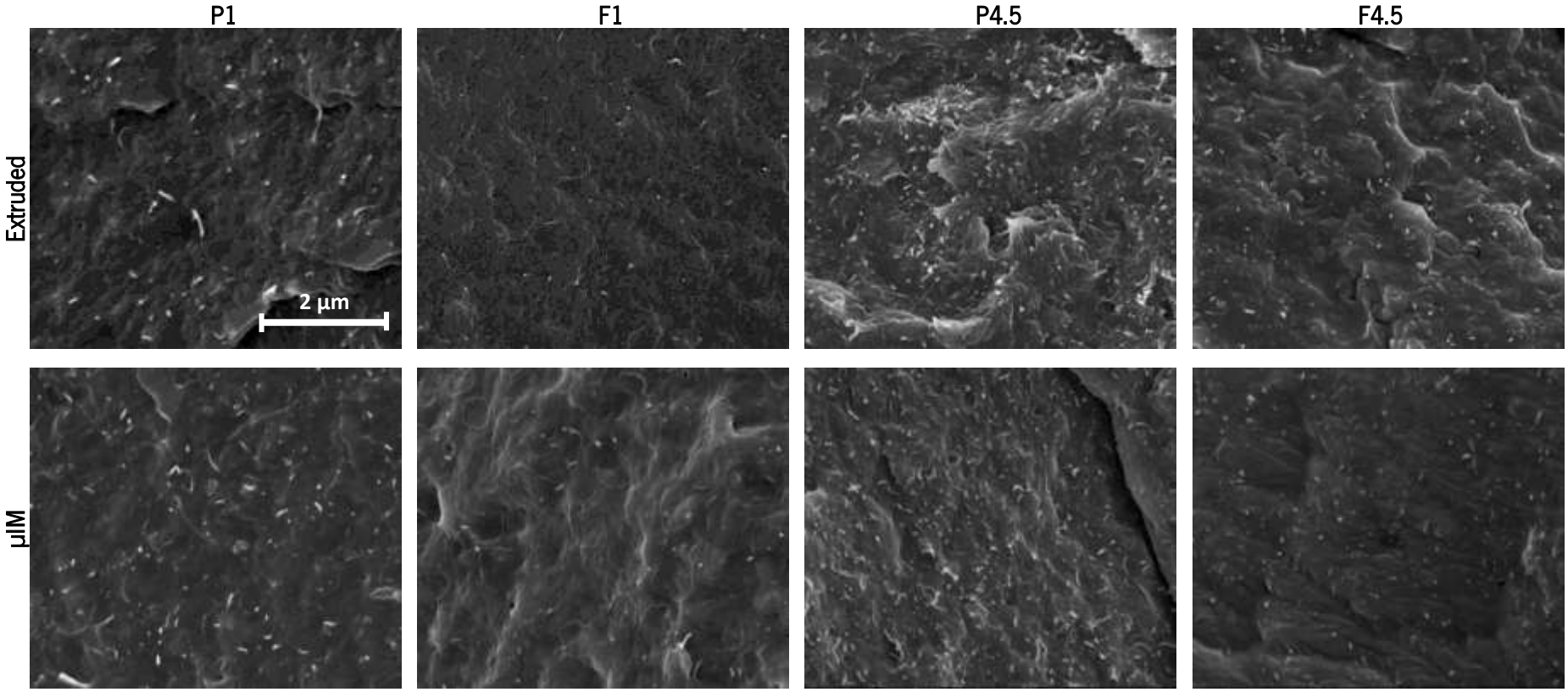

Figure 5.1 - SEM micrographs of the composites with 1% and 4,5 wt.% of p-CNT and f-CNT (designed as P1, F1, P4.5 and F4.5) obtained for extruded samples and µIM tensile specimens. All the SEM images have the same scale as the first.

Table 5.1 - Crystallization and melting parameters of extruded and μIM PA6 and its nanocomposites.

	Sample	First heating		Cooling			Second heating	
		T_{m1} (°C)	χ_{c1} (%)	T_c (°C)		ΔH_c (J/g)	T_{m2} (°C)	χ_{c2} (%)
Extruded	PA6	223	30.7	193		57.8	217 221	39.7
	P1	223	31.2	197	208	60.6	219	36.4
	F1	222	34.3	197	.....	77.2	220	35.9
	P4.5	222	30.3	197	211	59.9	221	31.9
	F4.5	223	32.5	198	210	60.0	220	37.4
μIM	PA6	222	25.5	193		69.8	215 220	30.8
	P1	222	30.2	197	209	50.8	220	35.0
	F1	222	32.9	198	208	53.9	221	35.4
	P4.5	221	30.7	197	209	46.9	218	37.9
	F4.5	221	37.1	197	208	53.9	219	38.7

Figure 5.2 shows the DSC curves of pure PA6 and PA6/CNT nanocomposites during heating above the melting temperature to study the effect of thermal history, induced during processing, in extruded and μIM nanocomposites. The first heating peak temperature is similar for PA6 and PA6/CNT nanocomposites for both processing techniques. The major difference is that μIM PA6 presents a secondary crystallization peak starting near 190°C, while the extruded materials start melting near 203°C. This secondary crystallization was already explained in section 4.3.

The μIM composites with low CNT content show a small secondary crystallization, and the heat of fusion was corrected by subtracting the heat involved in the secondary crystallization. This effect is less notorious at high CNT content, and the correction was not made for the composites with 4.5 wt.% CNT, pure or functionalized.

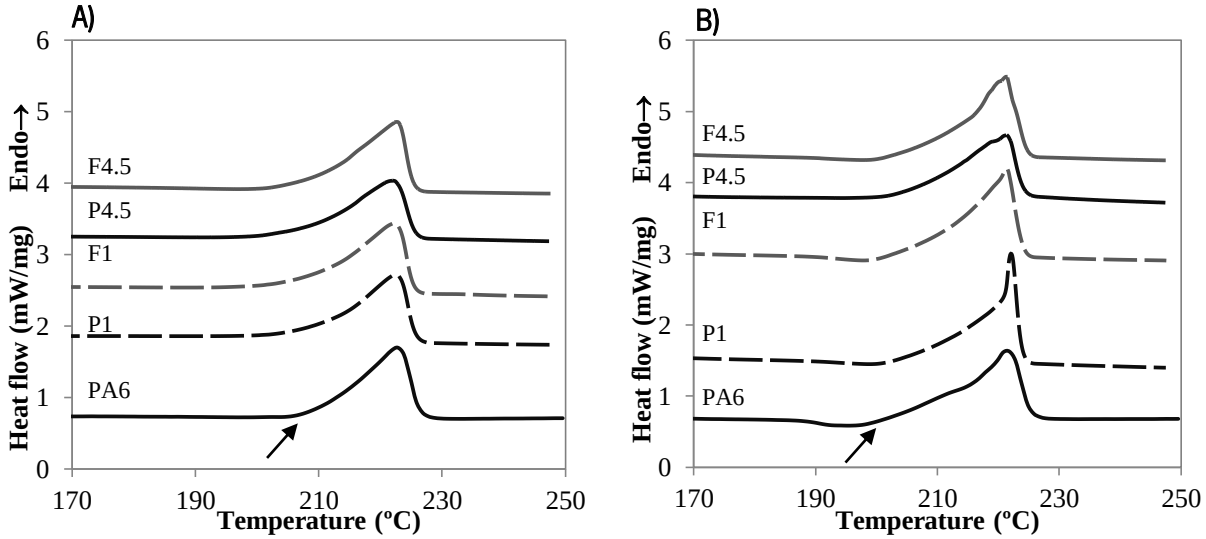

Figure 5.2 - DSC first heating curves of PA6 and PA6 with various content of p-CNT and f-CNT for A) - extruded and B) μIM nanocomposites

The effects of nanotube loading on the crystallization of PA6/CNT nanocomposites were examined using DSC after eliminating the thermal history, by melting and controlled cooling.

Figure 5.3 and Figure 5.4 show, respectively, the DSC thermograms recorded during the cooling and second heating cycles, for extruded and μIM samples of p-CNT and f-CNT and two nanotube loadings.

Figure 5.3 illustrates that for PA6 matrix only a single crystallization peak is observed with maximum intensity near 193°C, while for PA6/CNT nanocomposites the crystallization process splits into two peaks starting at higher temperature, with maxima near 197°C and 209°C, either for extruded or μIM composite samples. The crystallization peaks of nanocomposites shift to a higher temperature with the incorporation of CNT compared with neat PA6. As shown in Table 5.1, the incorporation of CNT results in a rise of T_c for all nanocomposite systems but this increment is not proportional to the CNT content. These results suggest that CNT promote the formation of crystallization nuclei for PA6. In addition, the range of crystallization temperature of all composites is wider than for PA6 matrix. This behavior of PA6 matrix in the presence of CNT has been reported [167, 233, 257] and two different interpretations of the formation of a double crystallization peak were provided. One of them describes the surface of the CNT as inducing a specific type of crystallite growth, perpendicular to the CNT axis, known as transcrystallinity [233, 278], while away the CNT crystal growth occurs as in the bulk polymer. The other interpretation is based on a two-step crystallization of α-phase only, and was proposed by Phang et al. [257].

The effect of μIM on the degree of crystallinity is shown in Table 5.1. It was observed that the μIM process does not affect considerably the overall degree of crystallinity of the nanocomposites, in agreement with other results reported in the literature [164, 273].

Figure 5.4 depicts the second heating of the PA6 and its nanocomposites. The PA6 matrix presents two crystallization peaks, although not fully resolved. The peak at about 215-217° C was attributed to the melting of γ-phase, while the 220-221°C peak may be due to the thermodynamically stable α-phase of PA6 [163]. The addition of CNT induce the merging of the two peaks into a wide one with the maximum near 220°C. The amount of CNT does not seem to affect the peak shape and intensity.

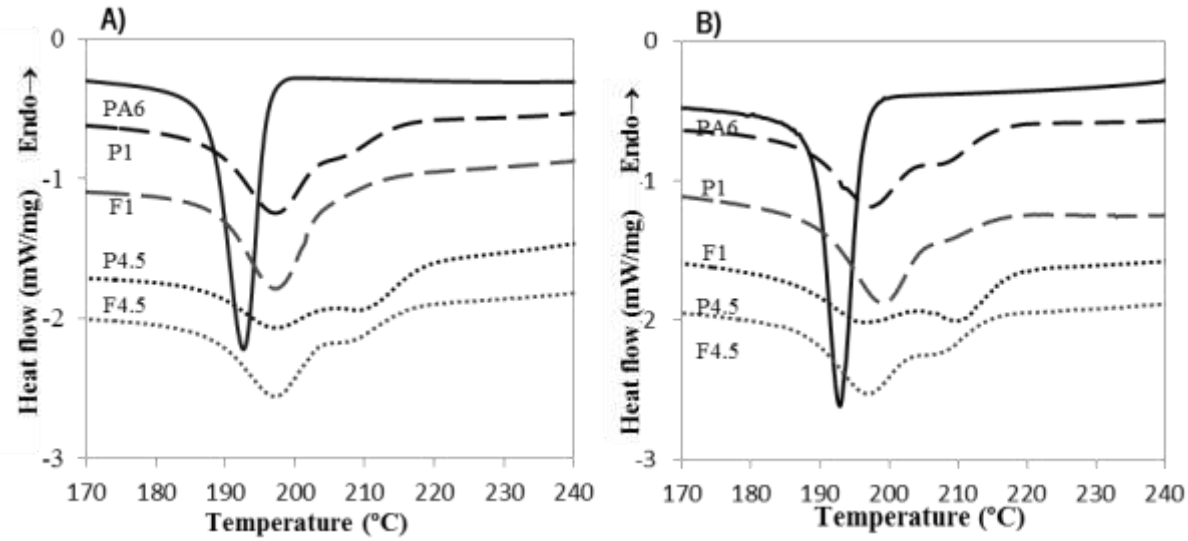

Figure 5.3 - DSC cooling curves of PA6 and PA6 with p-CNT and f-CNT for A) – extruded and B) - μIM nanocomposites

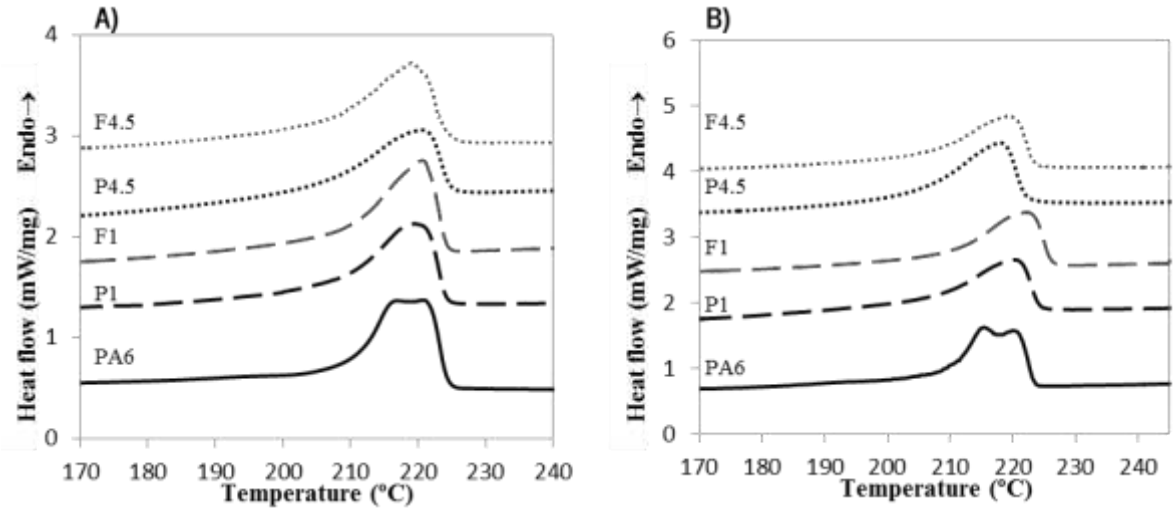

Figure 5.4 -DSC second heating curves of PA6 and PA6 with p-CNT and f-CNT for A) – extruded and B) - μIM nanocomposites.

According to Figure 5.4 and the results presented in Table 5.1, the effect of CNT addition on the overall degree of crystallinity is not significant [273].

5.3.3. Wide angle X-ray diffraction

Diffraction patterns and the integrated intensity profiles of the μIP are presented in Figure 5.5 and Figure 5.6.

The integrated intensity profiles clearly show that the γ crystalline form predominates in the μIP of pure PA6, while the α crystalline form predominate in all other samples.

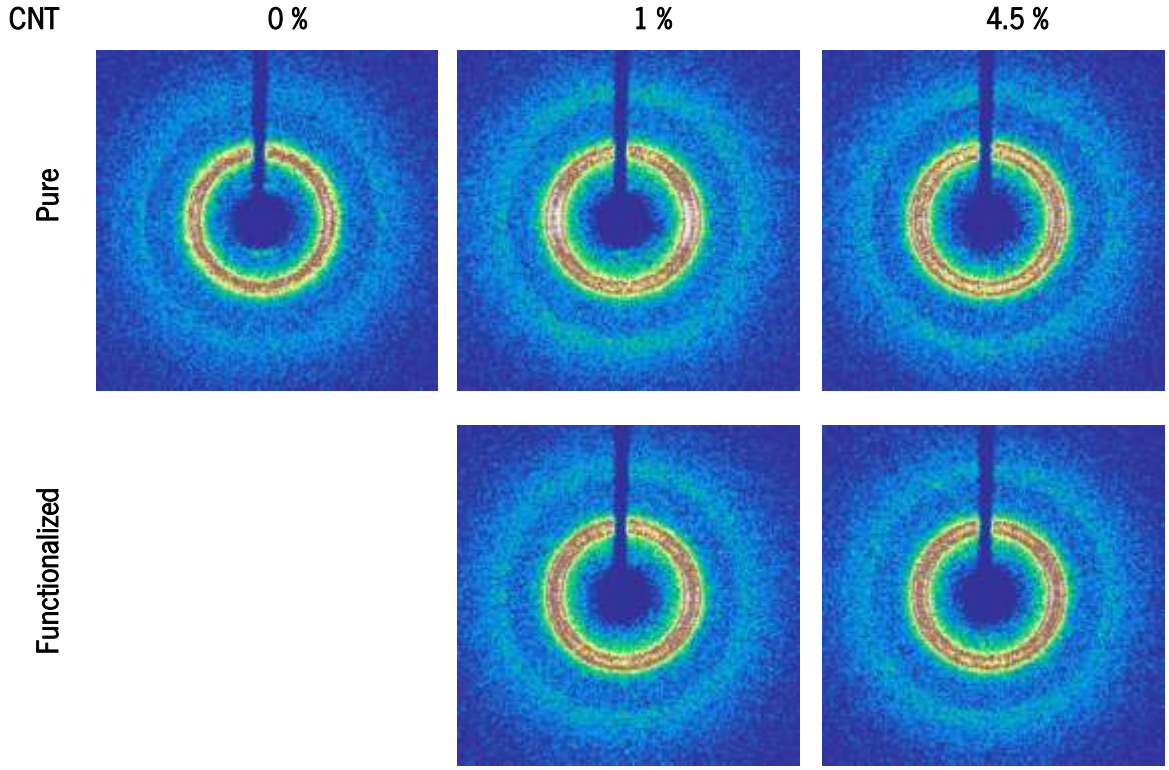

Figure 5.5 - WAXD patterns of μP. For the scattering patterns, the flow direction corresponds to the perpendicular direction to the page.

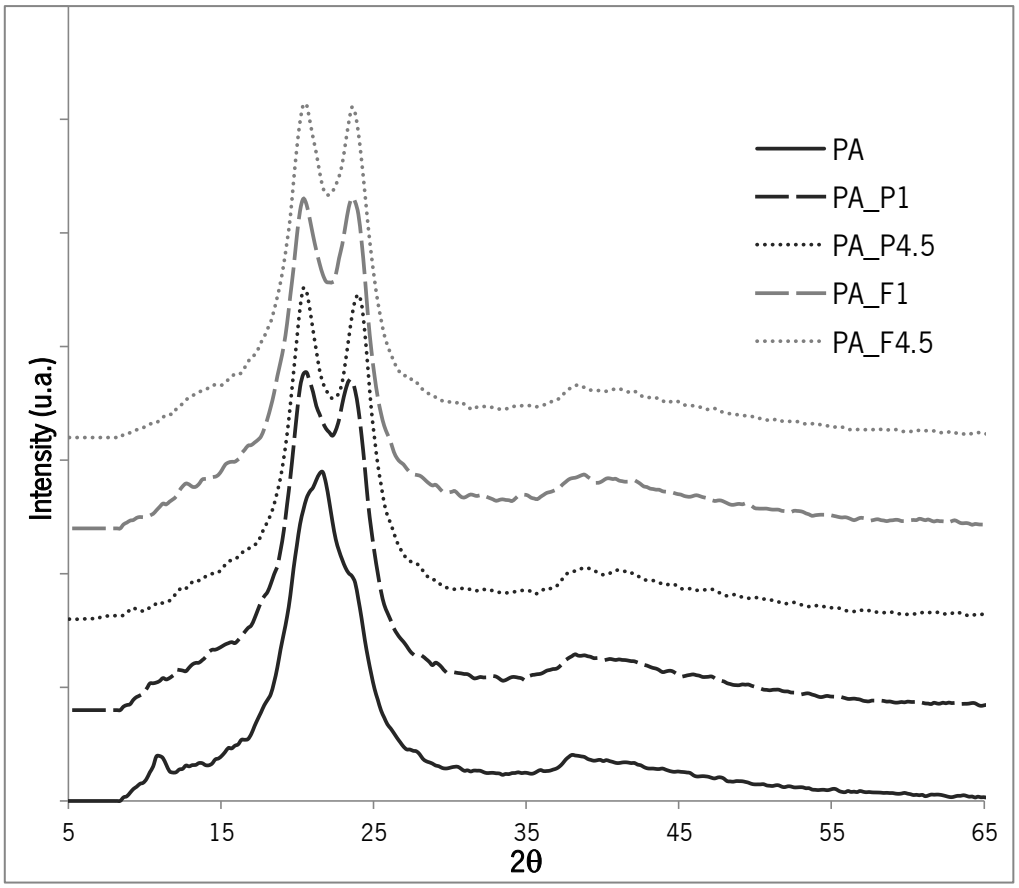

Figure 5.6 - Integrated intensity profiles of the μIP samples.

Figure 5.7 presents the cristalinity evaluation from the fitting of the integrated intensity profiles by Gaussian functions. The overall cristalinity is lower in all composite samples compared to the pure PA6 sample. These results also show a marked difference in the γ and α phase relative amounts, the γ phase dominates in the pure PA6 sample while in all composites the α phase is more abundant. The composite with 1% pure CNT has a higher γ phase content than all the others that present about the same value, as can be observed in Figure 5.7.

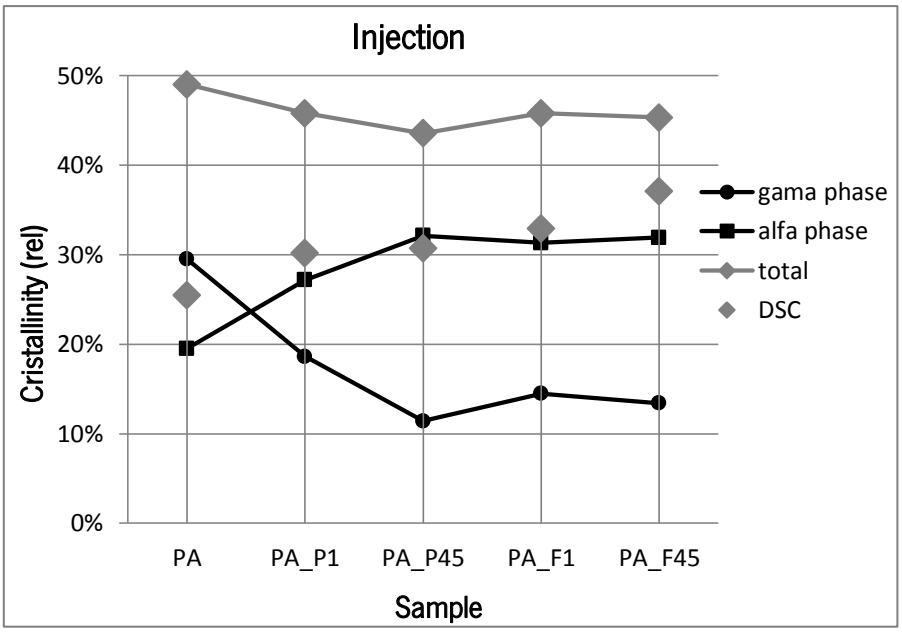

Figure 5.7 – Crystallinity and α and γ-phase content data obtained from fitting of WAXD patterns of μ-parts.

The crystallinity results for the core of the μIM samples, presented in Figure 5.8, also show that the γ phase content is larger in the pure PA6 samples compared to the composites. Among the latter there is no significant difference, both in total crystallinity and on the ratio of α to γ phase. The extruded samples, Figure 5.9, present lower cristalinity for the composites, as also observed in the μIM samples, but the relative amount of α and γ phases do not change.

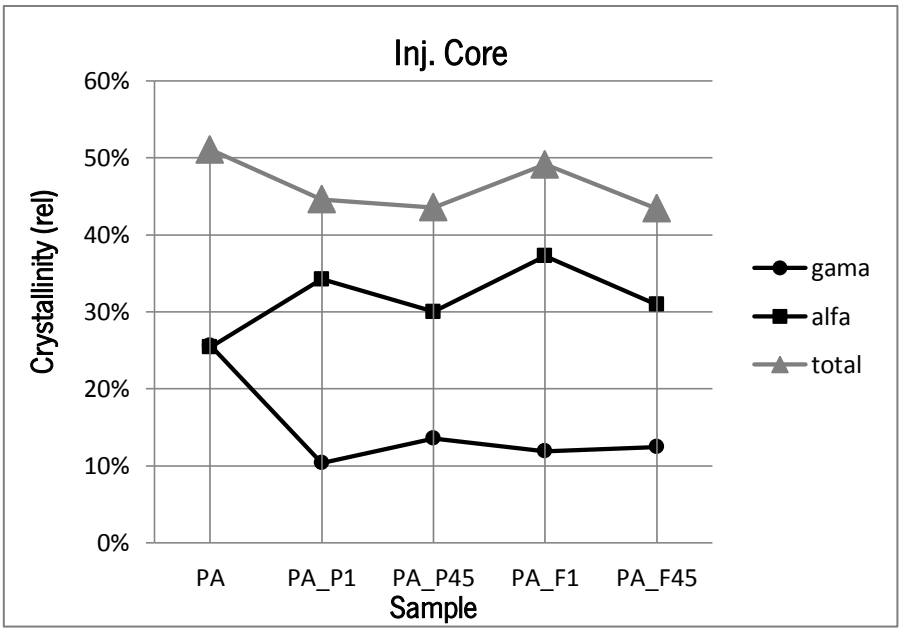

Figure 5.8 - Crystallinity and α and γ-phase content data obtained from fitting of WAXD patterns of core from μparts.

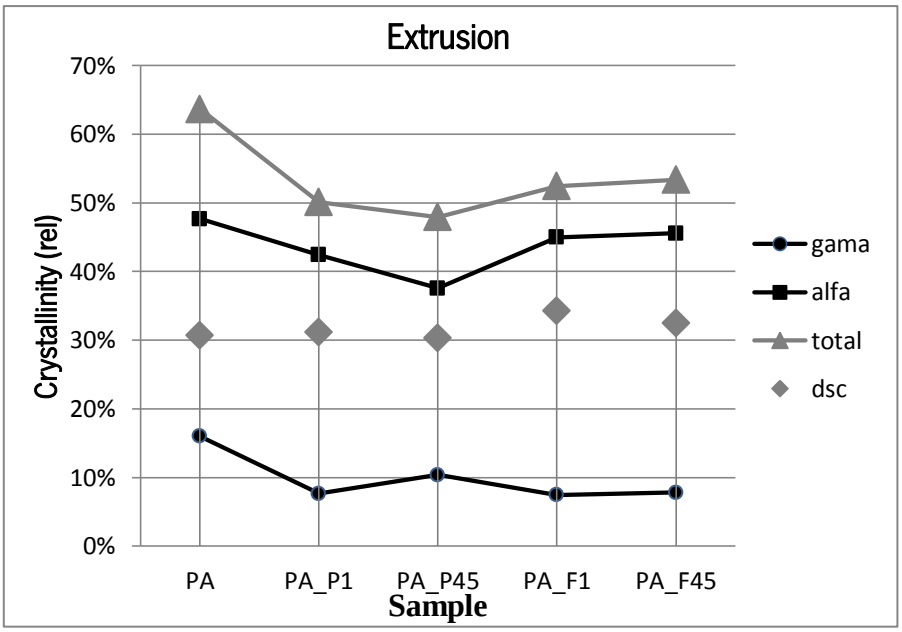

Figure 5.9 - Crystallinity and α and γ-phase content data obtained from fitting of WAXD patterns of extruded samples.

The orientation of the crystalline reflections was determined using POLAR software performing the analysis on the 2D intensity data. The measured intensities where decomposed in two components, one isotropic and another anisotropic. The Hermans orientation factors, f_z, [266], calculated on the anisotropic intensity component, are presented in Table 5.2 for the μP (injection), its core region (inj. core) and for the extruded sample (extrusion) of all conditions.

Table 5.2 - Hermans orientation factors calculated for μP and extruded PA6 samples.

Samples	Injection		Inj. Core		Extrusion	
PA	-0,2021 (γ2)		-0,1165(γ2)		-0,0695	0,0723
P1	-0,2425	-0,2794	-0,1854	-0,2288	0,1329	-0,095
P45	-0,2183	-0,2171	-0,1799	-0,1648	0,0196	0,0112
F1	-0,2081	-0,2047	-0,199	-0,1829	-0,0455	-0,0570
F45	-0,1815	-0,1651	-0,1643	-0,1958	-0,0162	0,1258

*The Hermans orientation factor ranges from -0.5 to 1.0, corresponding to fully oriented crystalline planes perpendicular and parallel to the reference axis, respectively. A value of zero corresponds to random orientation. Except otherwise indicated the orientations were calculated at the α_1 and α_2 peaks, 2θ =20.25 ° and 23.26°, respectively. The values marked as γ_2 were calculated using the γ_2 peak at 2θ =21.25°.

All μIM present some orientation that seems to decrease with the presence of the CNT and with the functionalization. Comparing the orientation of the complete sample and the core the results show that

the presence of the CNT reduces the difference between them. That is, the orientation effect of the μIM in the skin region is reduced when CNT are present, and even more when they are functionalized, but the orientation effects are observed throughout the sample.

5.4. Conclusion

The thermal property indicated that the CNT promote a faster crystallization of PA6; however, this does not reflect in an increase of crystallization degree.

Likewise, this study indicated that in the PA/CNT nanocomposites produced by μIM α-phase prevails while in μIM PA matrix is the γ-phase.

6. DISPERSION OF CNT IN PA6 FOR MICROINJECTION MOULDING

This chapter is based on the article:

Ferreira T, Paiva MC, Pontes A, Dispersion Of Carbon Nanotubes In Polyamide 6 For Microinjection Moulding, *J Polym Res* (2013) 20:301

6.1. Introduction

Among several potential applications proposed for CNT, polymer-based nanocomposites are particularly interesting, due to the ease of fabrication, the range of shapes that may be produced and the possibility of miniaturization [113].

The main challenge is to convey the excellent properties of CNT to the composites, to form electrically conductive materials with significantly enhanced mechanical properties, at low filler contents. The composite percolation threshold depends on several parameters such as the type of CNT, the matrix composition and morphology, and the filler dispersion state [2, 151].

Nanocomposite properties are limited by the ability to conveniently disperse the CNT in the polymer, forming a conductive network. The optimization of the composite's mechanical properties also depends on the ability to extensively disperse the CNT agglomerates, and to establish a strong CNT-polymer interface. The chemical inertia of the CNT surface and weak interactions between the CNT and most polymers are limitations to the preparation of nanocomposites with good mechanical properties. The chemical modification of the CNT surface to improve the compatibility with the polymer is a strategy that is proving to be efficient for the enhancement of the composite's properties. For example, Li et al [67] increased the compatibility and dispersion of multiwall CNT in PA6 by amino-functionalization. CNT functionalization may enhance their dispersion, but its main role is expected to be the establishment of efficient load transfer from the polymer to the nanotube network [86]. Liu et al. improved the elastic modulus and yield strength of PA6 composite prepared via melt mixing and compression moulding, attributing this to good dispersion and adhesion [163]. The improvement in mechanical properties and changes in the crystallization behaviour of the PA6 composites prepared by melt compounding and microinjection moulding were associated to CNT functionalization by amidation that improved wettability and dispersion [164].

The dispersion of CNT in the polymer to the exact level required for the establishment of a CNT network with the lower CNT content possible, together with a good CNT-polymer interface, appear to be the key factors for the formation of nanocomposites with good mechanical and electrical properties. Thus, the characterization of the CNT dispersion level is important for the understanding of the nanocomposite physical and mechanical properties. The study of the agglomerate dispersion mechanisms in melt mixing reported by G. R. Kasaliwal et al. [174] provides an interpretation based on agglomerate rupture and erosion mechanisms. The authors concluded that CNT agglomerate

dispersion by rupture mechanism requires less time and high shear stress, whereas at low shear stress the erosion mechanism dominates, requiring a longer time to act. Optical microscopy (OM) was used to investigate the CNT agglomerate morphology in the composites, to quantify CNT dispersion and distribution and to analyze the presence of remaining primary agglomerates, and may help to establish a relationship between structure, properties and process conditions [225].

Several processing methods such as solution mixing [279], in situ polymerization [280] and melt-mixing [105, 159, 161, 281, 282] have been tried to produce homogeneous dispersion of CNT in a polymer matrix. Among these, melt mixing with thermoplastic polymers is the more convenient given its compatibility with current industrial practices, higher yield and solvent free procedure. In this area, only a small number of studies report microinjection molding (μIM) as the method of shaping the conductive polymer composites, and its influence on the composite properties [205, 283].

The process of μIM is one of the most efficient and economic processes for the large-scale production of thermoplastic polymer microparts with high precision, with the ability to produce complicated 3D parts for the miniaturization of components. This is a global trend for application in many industrial sectors: automotive, aeronautics, telecommunications, electronics, biomedical, informatics [113]. Significant work on μIM was reported along the last decade, most of it concerning neat polymers [114, 121]. The complex thermomechanical history imposed on the polymer, extreme injection pressure, high shear, elongational flow, cooling rate and very short cycle time, influence the polymer morphology [284]. When forming nanocomposite parts, these processing conditions affect the establishment of a nanotube network, and thus the nanocomposite properties. For the composite electrical properties, it was reported that the percolation threshold is usually found to be higher for thermoplastic matrices. Abassi et al. [205] concluded that the shear flow in the μIM process could induce significant CNT alignment, decreasing CNT contact, and shifting the percolation threshold to higher filler contents. They reported a percolation threshold of 9 wt. % for μIM PC/MWNT composites, compared to 3 wt. % observed for compression moulded samples. For polyamide nanocomposites the reported values of the percolation threshold were found to be in the range of 2.5-7 wt. % for melt-mixed and compression moulded films [151] and 4-6 wt. % for injection moulded samples [159].

According to theoretical investigations using Monte Carlo simulations, a minimum resistivity occurs for a partially aligned rather than for a perfectly aligned nanotube film and, when the CNT are highly aligned, the resistivity strongly depends on the measurement direction, increasing two orders of magnitude when alignment and measurement directions are not similar [221]. Recently, Mahmoodi et al. compare the electrical resistivity in the flow and thickness directions for μIM samples with different

mold cavities and compression molding [220]. They concluded that μIM through an edge gate led to higher volume resistivity in the flow direction and lower in the thickness direction, compared to μIM through a fan gate.

In the present work μIM was used to produce nanocomposite specimens based on PA6 and CNT. The CNT and PA6 were melt blended by mini twin screw extrusion and processed by μIM to mold micro-size test bars. The CNT used were as received and chemically functionalized, using a non-aggressive chemical procedure that covalently bonds pyrrolidine groups to the CNT surface [76, 104]. This procedure modifies the CNT surface without breaking or oxidizing the CNT. The influence of the processing steps on the CNT dispersion state was analyzed by OM and scanning electron microscopy. The composites were characterized in terms of the electrical conductivity and tensile properties.

6.2. Experimental section

6.2.1. Carbon nanotube functionalization and characterization

The CNT used were NC7000 from Nanocyl, Belgium. They were chemically functionalized using the 1,3 – dipolar cycloaddition reaction of azomethine ylides using the experimental route described in [277].

The amino acid used was *N*-benzyloxycarbonylglycine (Z-gly-OH, 99%, from Aldrich). Paraformaldehyde (reagent grade from Sigma) was used to form formaldehyde by thermal decomposition. The reagents were blended in a 1:5 molar ratio. The mixture of reagents and CNT was suspended in a small volume of diethyl ether, sonicated during 3 min and heated in a round bottom flask until total evaporation of the solvent. Then, the mixture was heated for 3 h at 250°C. The resulting CNT were washed with ethanol, filtered and dried. The functionalized CNT were analyzed by thermogravimetric analysis (TGA) on a TA Q500, and by X-ray photoelectron spectroscopy (XPS), on an AxiS Ultra photoelectron spectrometer.

6.2.2. Preparation of carbon nanotube/polyamide 6 composites

The nanocomposites were prepared by melt mixing PA6 (Badamid®B70) with 1, 1.5, 3 and 4.5 wt. % of non functionalized CNT (p-CNT) and functionalized CNT (f-CNT) on a mini twin-screw extruder. The

operating variables were temperature, throughput and screw speed. The temperature profile selected was 245, 255, 255, 255 and 235 °C from feeding zone to die. The throughput was kept constant at 120 g/h with the screws rotating at 60 rpm.

The extruded nanocomposites were microinjection moulded using a Boy 12 A. The microinjection moulding machine has an injection screw of Ø14 mm (Dr Boy, Germany) that combines technical characteristics required for microinjection and affordability. The injection moulding cell also includes a mould temperature regulator and an external control unit for the cartridge heaters used in the temperature control system of the mould. The Boy 12 A machine is able to meter an injection volume of 0.1 cm^3 at a high flow rate, up to 15.6 $cm^3 s^{-1}$. The injection pressure is limited to 240 MPa.

µIM of the PA6/CNT nanocomposites was carried out at a temperature profile in the injection unit ranging from 210, 220, 230, 235, 245 to 270 °C, under a pressure of 100 bar, while the speed was kept constant at 240 mm/s. The mold temperature was optimized and kept at ~100°C.

The tensile specimens were produced using a mold with the dog-bone shape cavity and dimensions described in Figure 6.1 A; the parallelepipedic specimens were produced using the mold shape and dimensions described in Figure 6.1 B.

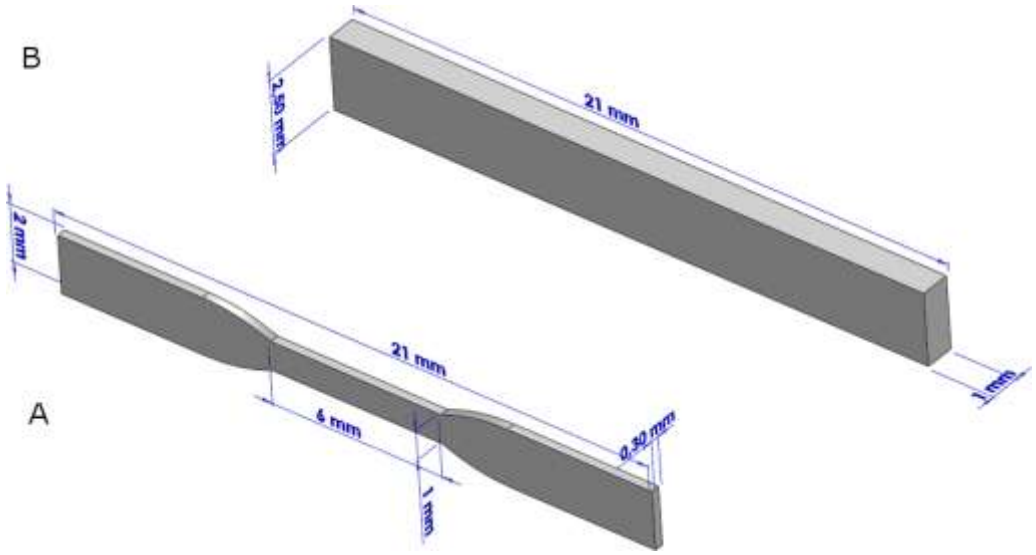

Figure 6.1 - Nominal dimensions of tensile (A) and parallelepipedic (B) specimens.

6.2.3. Composite characterization

6.2.3.1. Morphology

The composite morphology was analyzed by optical and scanning electron microscopy (OM and SEM, respectively). OM observations were carried out on 5µm thickness microtomed sections of the

composites, obtained with a Leitz 1401 microtome. The microtomed sections of the extruded strands were obtained perpendicular to the extrusion direction, the μIM tensile specimens were obtained along the flow direction, and the parallelepipedic specimens were obtained parallel and perpendicularly to the flow direction. The morphology of the CNT agglomerate dispersion was analyzed using an Olympus BH2 optical microscope in transmission mode. Images were acquired with a digital camera Leica DFC 280 coupled to the microscope. The CNT agglomerate area, total micrograph area and number of agglomerates were measured using the software Leica Qwin Pro. At least six micrographs of different thin sections were analysed to provide statistically significant data.

The extruded, parallelepipedic and tensile μIM samples were cryo-fractured, sputter-coated with a thin layer of palladium-gold and observed by SEM, on a FEI Quanta 400 FEG ESEM.

6.2.3.2. Electrical resistivity

The electrical resistivity of the composites was measured by the DC resistance in the flow direction, for the extruded and μIM samples. The measurements on the μIM samples were performed along the flow direction, and also across the thickness for the parallelepipedic samples. For the measurements in the flow direction, samples with approximately 2-3 mm length were cut from μIM parallelepiped samples and extruded strands, while for tensile specimens the surface was polished to remove the insulating thin layer of polymer previously observed by OM. The same procedure was used for the μIM parallelepiped samples, for resistance measurements across the thickness. The contact area was coated beforehand with a thin layer of silver lacquer (Agar Scientific Batch No. 0416) to ensure good contact of the sample surface with the electrodes.

The measurements were carried out at room temperature using a Picoamperimeter/voltage source Keythley 6487 equipped with a two probe test fixture. For each sample the *I-V* curves were obtained in the range of -10 V to 10 V, and the resistance was determined from the slope of the curve. The resistance was then converted to volume resistivity accounting for the sample geometry.

6.2.3.3. Mechanical properties

The tensile tests were performed on a Instron 4505 at room temperature, at a constant speed of 5 mm/min, 14 mm of gauge length, and using a load cell of 1 kN. The tensile strength, elongation at break and Young's modulus were measured. The reported values are an average over six tested specimens, for each composition and condition.

6.3. Results and Discussion

6.3.1. CNT functionalization and characterization

The 1,3-dipolar cycloaddition reaction was carried out using an α-amino acid and an aldeyde, under solvent free conditions, as described elsewhere [277]. The dipole formed may react with the CNT surface through cycloaddition, forming pyrrolidine groups at the CNT surface, as represented in Figure 6.2. The pyrrolidine groups may establish strong interactions with the amide groups of PA6, thus it is expected to improve the PA6/CNT interface, and the impregnation of the CNT agglomerates by the polymer. Thus, the functionalization is expected to improve the polymer/CNT interface and facilitate the CNT dispersion.

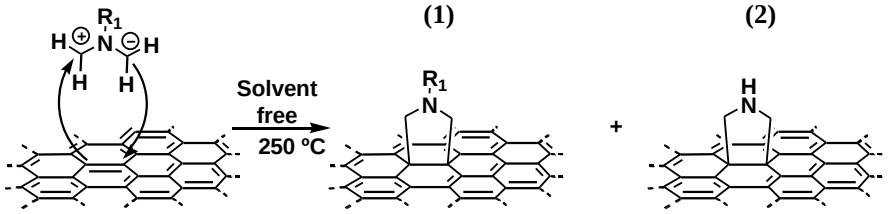

$R_1 = -COOCH_2Ph$

Figure 6.2 - Functionalization of the CNT surface using the 1,3-dipolar cycloaddition reaction.

Based on a previous study [76], it was observed that the reaction may yield two products: benzyl carbamate cycloadduct (1) and/or pyrrolidine (2) on the CNT surface.

According to XPS results for as received and functionalized CNT (Table 6.1) and considering that the increase in N concentration is attributed to groups 1 and 2, the degree of functionalization is 2.0% of functional groups relative to C atoms. Since the increase in oxygen concentration results from the O present in the protective group of the cyclic amine 1, the chemical composition of the functional groups was estimated to be approximately 15% of benzyl carbamate, 1, and 85% of pyrrolidine, 2.

Table 6.1 - Nitrogen and oxygen atomic composition of CNT obtained by XPS and weight loss results measured by TGA.

Sample	N (at%)	O (at%)	TGA weight loss (%)
p-CNT	-	0.8	1.6 ± 0.7
f-CNT	2.0	1.4	16.7 ± 1.2

The thermal stability of the f-CNT in dry conditions was investigated and compared to p-CNT. The corresponding TGA curves are depicted in Figure 6.3 and the weight loss presented in Table 6.1.

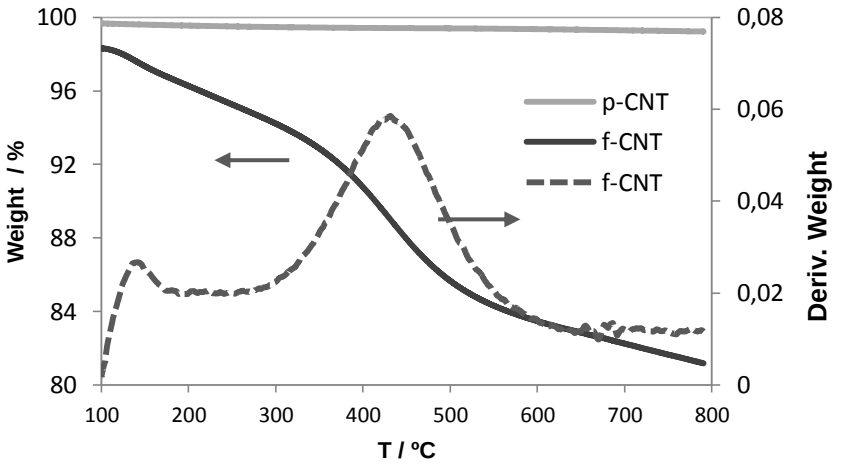

Figure 6.3 - Thermogravimetric analysis plots for as received and functionalized CNT, and the TGA curve derivative.

The as received and functionalized CNT were observed by SEM. Figure 6.4 shows representative images at two magnification levels. Higher magnifications, Figure 6.4C and D reveals long entangled CNT bundles, for p-CNT and f-CNT, demonstrating the mild nature of the functionalization route.

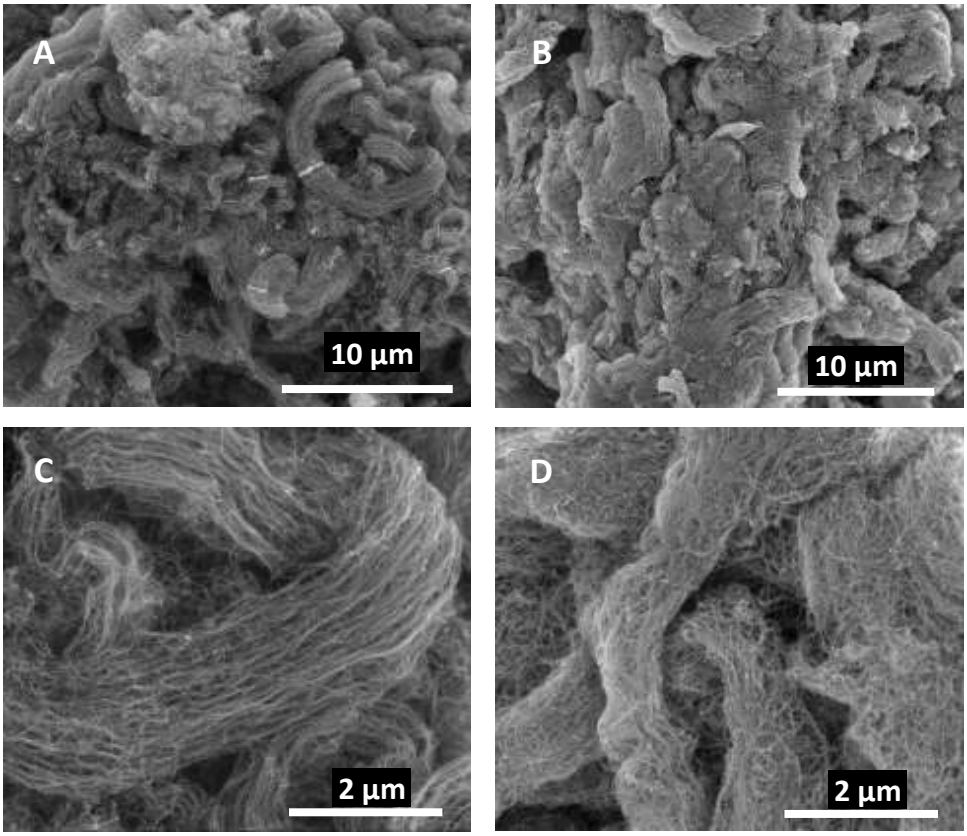

Figure 6.4 - SEM micrographs of as received (A and C) and functionalized (B and D) CNT.

6.3.2. Study of carbon nanotube dispersion

OM was used to measure the area of the CNT agglomerates observed on composite sections and to assess their distribution in the polymer. The micrographs obtained by OM were analyzed, and all the CNT agglomerates with area greater than 5 μm² were measured. The average agglomerate area, number of agglomerates per unit area, and agglomerate area ratio defined as the ratio of the total area covered by agglomerates to the total composite area analyzed, A_R, were determined. The variation of the cumulative agglomerate area ratio distribution, *F*, with the area of the agglomerates, illustrates the major characteristics of the non-dispersed CNT fraction, as explained elsewhere [104]. This representation is obtained by ranking the agglomerate areas measured, A_i, in increasing order of magnitude and plotting their cumulative area (the sum of the agglomerate areas $\sum_{i=1}^{j} A_i$, from the smaller to the jth agglomerate, divided by the total agglomerate area, $A = \sum_{i=1}^{n} A_i$) as a function of the agglomerate areas A_j. This is represented in Figure 6.5 for the composites with 1, 1.5, 3 and 4.5 wt. % of p-CNT and f-CNT. The plots highlight the fraction of agglomerates with areas smaller than 250 μm² present in each composite. The results show that the composites obtained after extrusion under the current processing conditions presented the larger CNT agglomerates, while after μIM the fraction of small agglomerates increased considerably. The effect of CNT functionalization was, for most of the composites, to reduce the size of the CNT agglomerates.

Figure 6.5E compares the cumulative agglomerate area ratio for μIM composites obtained with tensile and parallelepipedic specimen molds. It was observed that the shape of the μI mold affected the CNT agglomerate size, the mold with smaller thickness (Figure 6.1A) leading to the composites with smaller CNT agglomerates.

While the cumulative area ratio distributions obtained compare the morphology of the CNT agglomerates formed under the different composite processing conditions, it does not provide information about the CNT fraction that was effectively dispersed during the process. The latter may be assessed by the A_R, that is inversely proportional to the dispersion level: the smaller the composite area covered with CNT agglomerates, the larger the fraction of CNTs that were effectively dispersed. Figure 6.6 illustrates how the different processing steps and CNT functionalization affected the A_R.

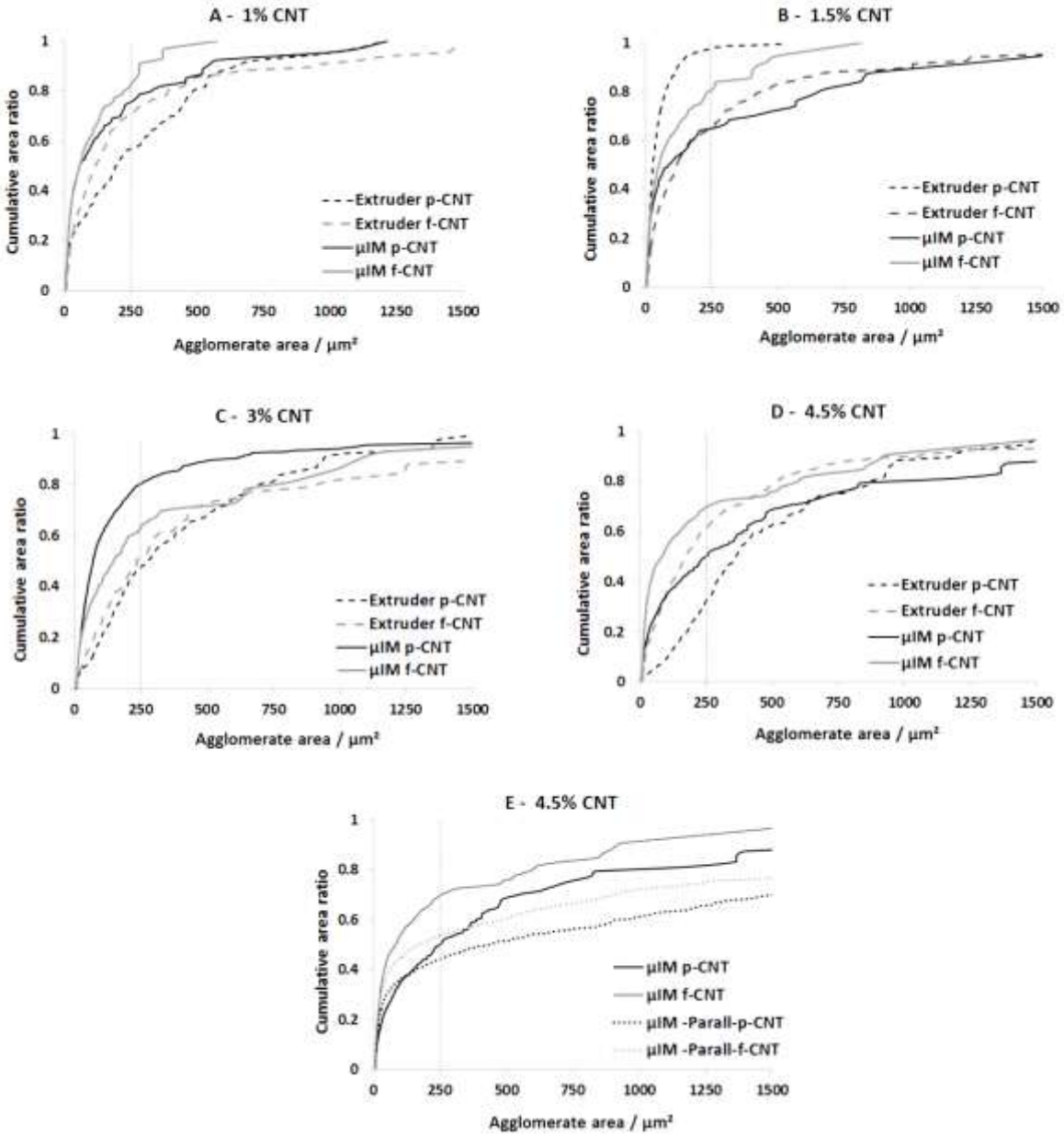

Figure 6.5 - A to D represent the cumulative area ratio for the composites prepared by extrusion (dashed line) and µIM tensile (continuous line); E compares the cumulative area ratio for the composites obtained from µIM tensile (continuous line) and parallelepipedic specimens (dotted line).

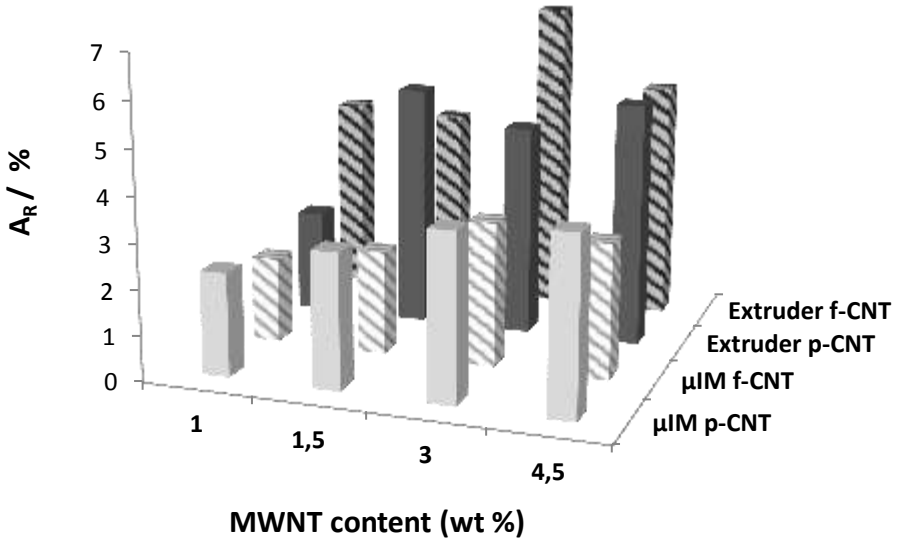

Figure 6.6 - Total agglomerate area ratios obtained for the composites with different CNT content.

Figure 6.6 shows that, except for the lower p-CNT composition, A_R was always larger for the extruded composites. Thus, the µIM step performed after composite extrusion improved the level of CNT dispersion. Functionalization enhanced CNT dispersion for the µIM composites, but this effect was not systematically observed for the extruded composites. For all compositions, µIM composites presented the lowest A_R values.

Optical micrographs of the nanocomposites with 4.5 wt.% of f-CNT or p-CNT revealed differences in the CNT agglomerate size, shape and number, as illustrated in Figure 6.7.

The CNT agglomerates in the extruded nanocomposites show a circular shape while the agglomerates in µIM samples present an elongated shape in the flow direction.

The cryo-fractured composites were observed by SEM, to monitor the dispersion of the non-agglomerated CNT. The cross-sections of the extruded and µIM composites, and in the latter case, the tensile and parallelepipedic bars, formed with p-CNT and f-CNT, were observed perpendicularly to the flow direction as illustrated in Figure 6.7.

The SEM micrographs showed that all the composites presented a large concentration of CNT outside the agglomerates with good CNT distribution. Comparison of the p-CNT and f-CNT composites shows that the latter have a better interface with the polymer, as evidenced by the longer p-CNT pull-out length, revealing a lower p-CNT/PA interaction.

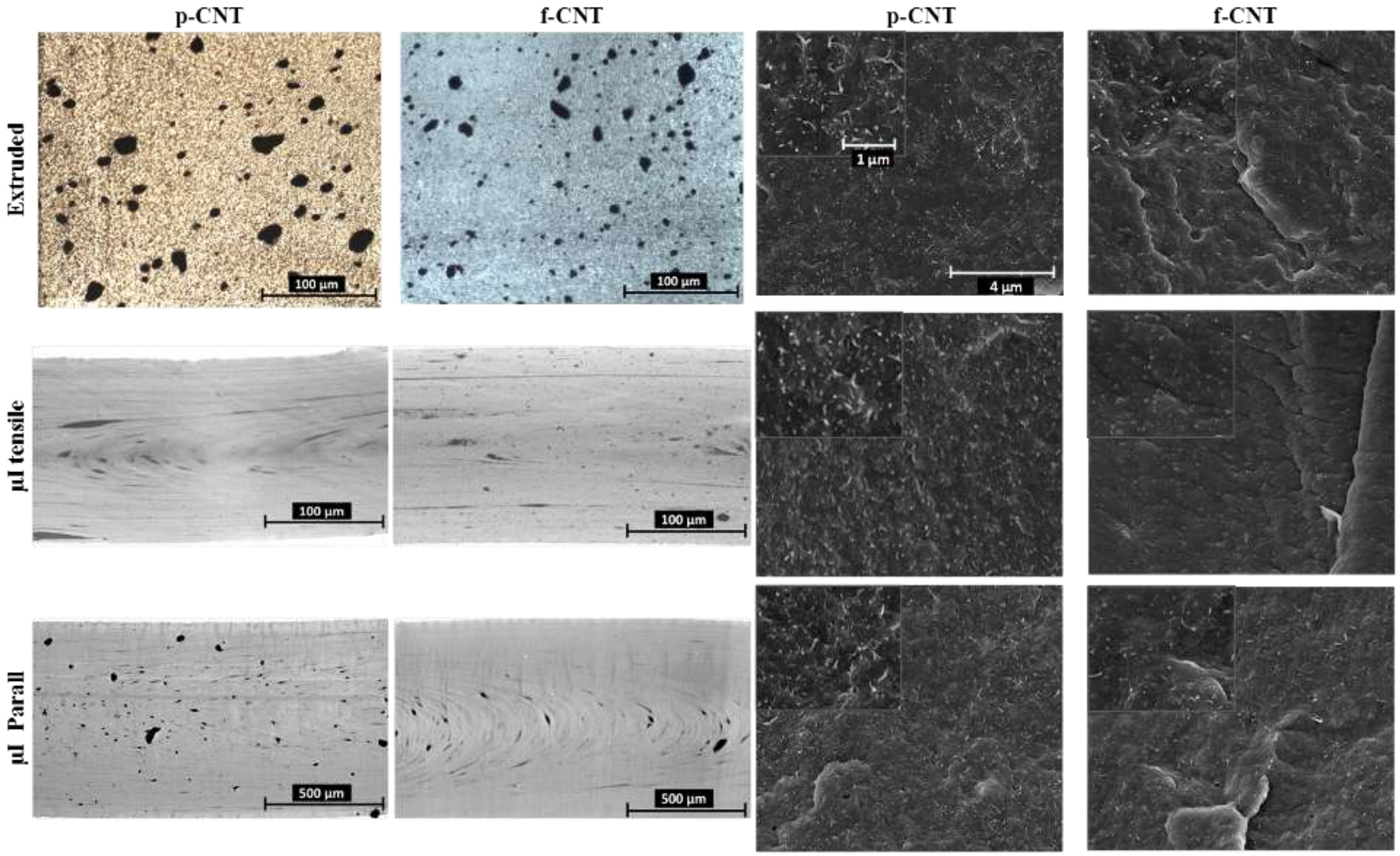

Figure 6.7 - OM (left) and SEM (right) micrographs of the composites with 4.5 wt.% CNT, obtained after extrusion and µIM (for tensile and parallelepipedic specimens). OM illustrates the influence of µIM on the CNT agglomerate size and shape. SEM micrographs show the CNT dispersed fraction, presenting an insert with a higher magnification image. All the SEM images have the same scale as the first.

The CNT agglomerate characterization depicted in Figure 6.5 and Figure 6.6, and Table 6.2, provide important information about the differences in the dispersion mechanisms of f-CNT and p-CNT in PA 6. The extrusion process generally induced higher CNT agglomerate rupture for the f-CNT composites compared to p-CNT, generating smaller agglomerates in the former, but without considerably affecting the overall dispersed CNT fraction, leading to similar A_R (Table 6.2). The higher shear flow developed during μIM (relative to extrusion) lead to further enhancement of the agglomerate rupture for p- and f-CNT composites, with a greater effect on the f-CNT agglomerates. The CNT agglomerate size distribution in the polymer considerably varied with the flow geometry. The tensile bars with smaller thickness induce higher shear in the polymer melt, which enhanced the dispersion of the f-CNT and reduced their agglomerate size.

6.3.3. Electrical properties

The percolation threshold for PA/CNT composites is in the range of 4-6 wt. % for μIM samples [159], thus this step of our study will focus only on the 4.5% composition.

The electrical resistivity was measured for the composites prepared by extrusion and μIM, in tensile and parallelepipedic test specimens. The measurements were performed in the direction of the flow (L) for all composites, and the parallelepipedic μIM samples were also analyzed in the perpendicular direction to the polymer flow (T). The results obtained are presented in Table 6.2 and Figure 6.8.

Table 6.2 - Optical microscopy and electrical resistivity characterization of the composites with 4.5% p-CNT and f-CNT

Sample	Processing method	Average agglomerate area (μm²)	Number of agglomerates/μm²	A_R	Electrical resistivity (Ω.m)
PA+4.5% p-CNT	μIM-tensile	45	8.6×10^{-4}	3.9	$7.4\text{x}10^{5}$
	μIM-parall	39	7.2×10^{-4}	2.9	$3.9\text{x}10^{2}$
	Extrusion	146	3.7×10^{-4}	5.4	4.9
PA+4.5% f-CNT	μIM-tensile	29	1.1×10^{-3}	3.0	$2.6\text{x}10^{6}$
	μIM-parall	29	1.5×10^{-3}	4.3	$1.1\text{x}10^{6}$
	Extrusion	55	9.7×10^{-4}	5.3	$3.4\text{x}10^{8}$

It was observed that the extruded p-CNT composites were electrically conductive, but the μIM process considerably increased the electrical resistivity of the composites, in spite of their larger fraction of dispersed CNT. Thus, it is possible that p-CNT orientation was induced by the high shear acting on the

polymer melt during μIM, disrupting the CNT conductive network generated during the extrusion process. The tensile-shaped μIM specimens showed a larger increase in electrical resistivity, probably due to greater CNT orientation induced by higher polymer shear flow rate. The parallelepipedic specimens, whose electrical resistivity was measured in the L and T directions, showed lower resistivity along the flow direction (L) compared to the thickness direction (T). This type of observation is compatible with CNT alignment effects, and was described by A. Behnam et al. [221] that reported the influence of the measurement angle on the electrical resistivity of composites with aligned CNT. The improved dispersion observed for the μIM composites with p-CNT, traduced by the lower A_R and smaller agglomerates obtained compared to the extruded material, resulted in higher composite electrical resistivity.

A remarkable difference was observed for the electrical response of the composites with p-CNT and f-CNT, the former always presenting lower electrical resistivity, irrespective of the processing method. Since the functionalization alone does not affect the f-CNT electrical properties (it was demonstrated before that the electrical conductivity of f-CNT pellets was similar to that of pure CNT pellets [104]) this effect may be due to the insulating action of the large polymer/f-CNT interphase formed. Nevertheless, the composites presenting higher A_R and larger agglomerate areas also show higher electrical resistivity, in opposition to what was observed for the composites with p-CNT. The electrical resistivity decreased for the μIM p-CNT composites, presenting the lower values for the parallelepipedic specimens, in the L direction. Figure 6.8 depicts the tendency for increase in electrical resistivity from extruded to μIM p-CNT composites, and the electrical behavior observed for the composites with f-CNT, that do not show a clear variation with the processing method.

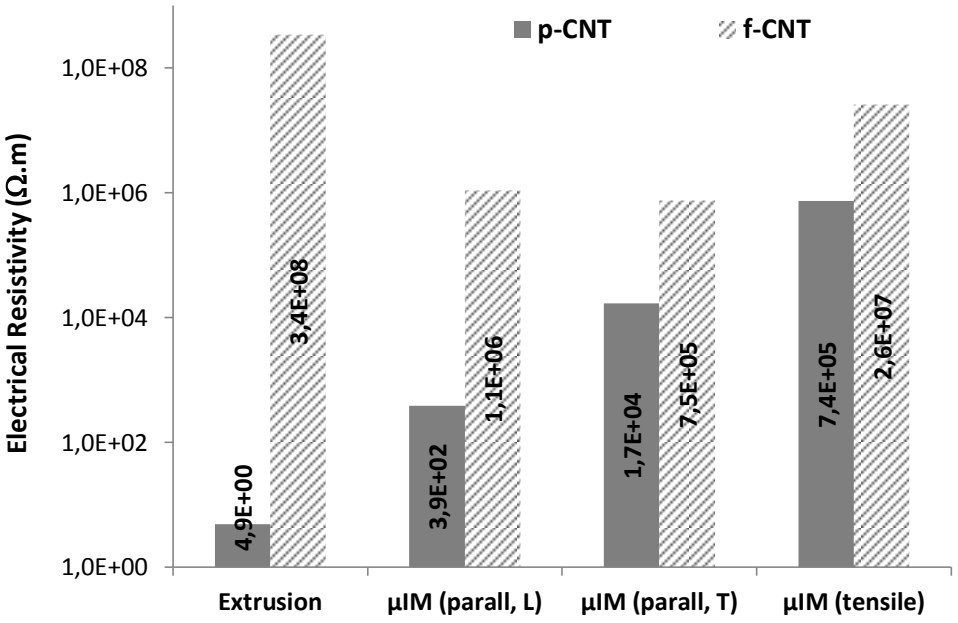

Figure 6.8 - Electrical resistivity of the composites prepared by the different processing methods and with different µIM molds.

6.3.4. Mechanical properties

Typical stress-strain curves of PA6 and all compositions of PA6/CNT µIM nanocomposites are shown in Figure 6.9.

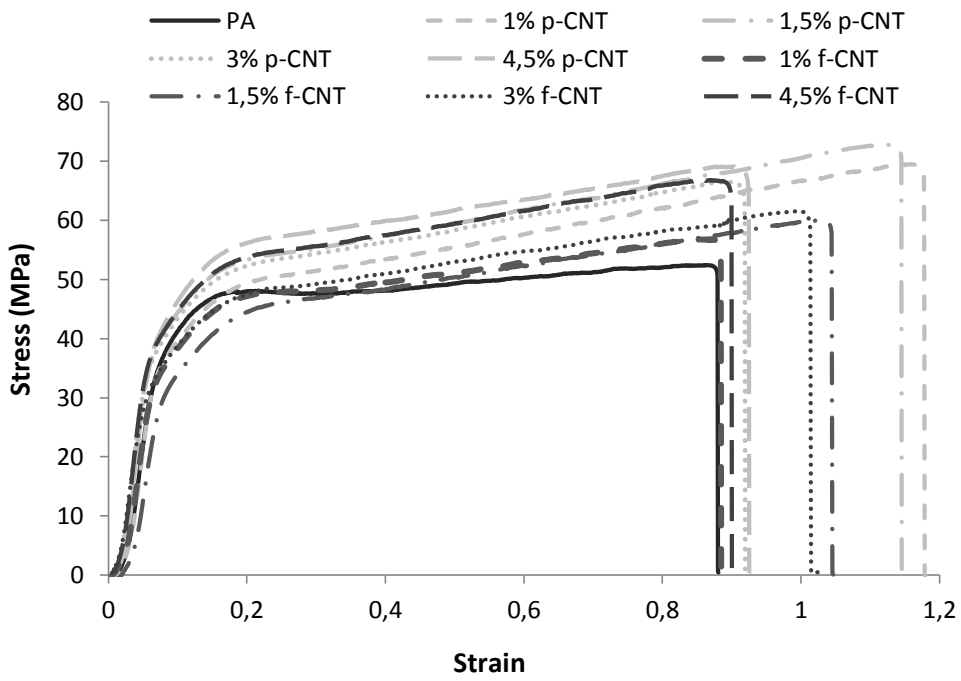

Figure 6.9 - Typical stress-strain curves obtained for PA6 and PA6/CNT composites.

The elongation at break of PA increases with the incorporation of CNT (pure or functionalized), becoming much larger than the PA matrix. This result is confirmed in Figure 6.10B.

Figure 6.10A shows that the tensile strength of the nanocomposites is always greater than that of neat PA6, presenting higher values for the p-CNT composites.

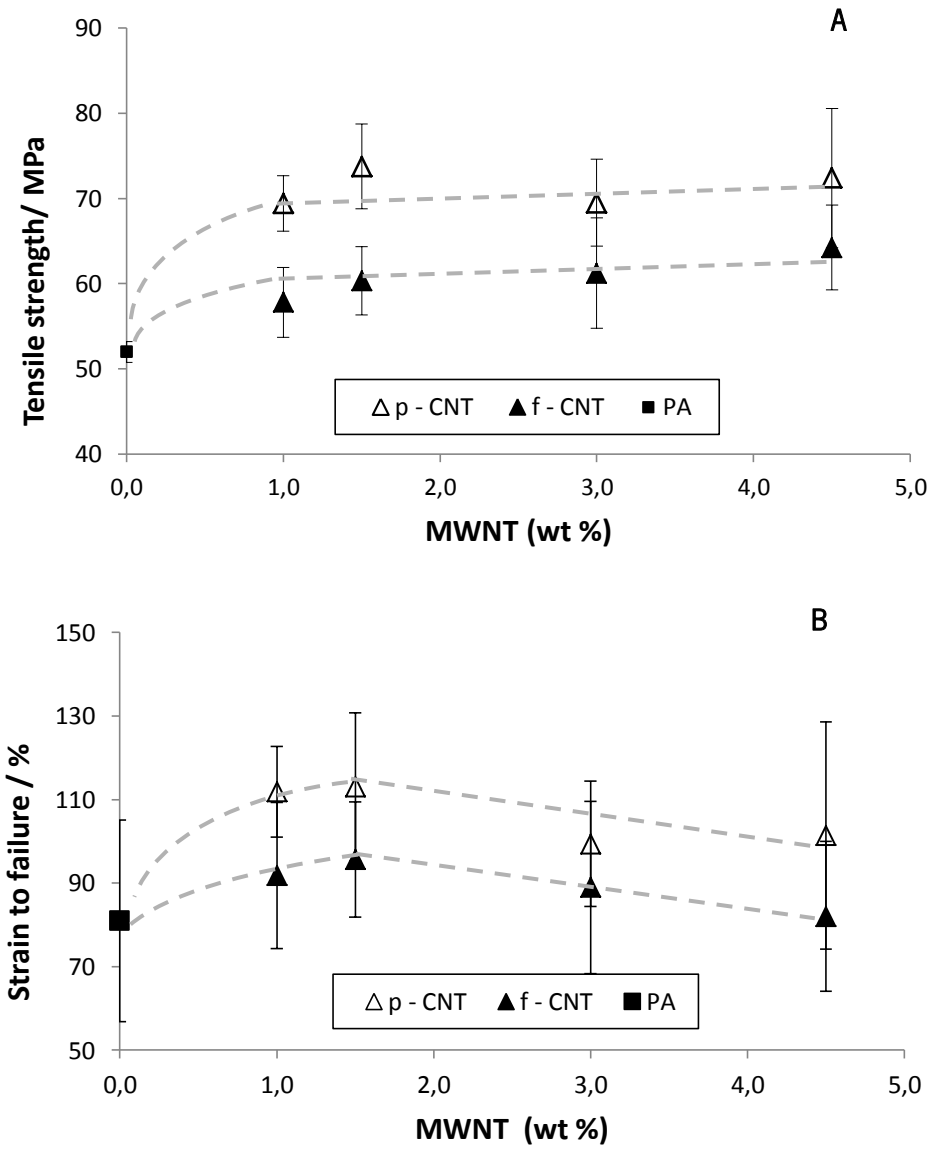

Figure 6.10 -Tensile strength (A) and strain to failure (B) of μIM tensile-shaped specimens of PA6 and PA6/CNT samples with p-CNT and f-CNT.

Figure 6.10 and Figure 6.11 present the tensile properties of PA6 and PA6/CNT composites, illustrating the improvement induced by the incorporation of p-CNTs and f-CNTs. The composites with p-CNT presented the best tensile properties, leading to an increase in 43% for the modulus, relative to PA6, for the 4.5 wt.% p-CNT composites. It should be noticed that the incorporation of 1% p-CNT

increased the modulus by 26% and the tensile strength by 33%, the latter showing a similar improvement to that obtained with 4.5 wt.% of p-CNT. As reported in other works, our results also showed that the optimum tensile properties are achieved at low CNT loadings [285]. The composites with f-CNTs also presented improved tensile properties compared to PA6, but they were proportionally lower than those obtained for the corresponding p-CNT composites. This result was surprising, considering the good f-CNT wetting by PA6 observed by SEM. It may be due to the formation of thermal degradation products at the PA6/CNT interface, since the composites were prepared at a higher temperature than the CNT functionalization temperature (270 °C versus 250 °C), or to other structural or morphological differences between p- and f-CNT composites, requiring further investigation.

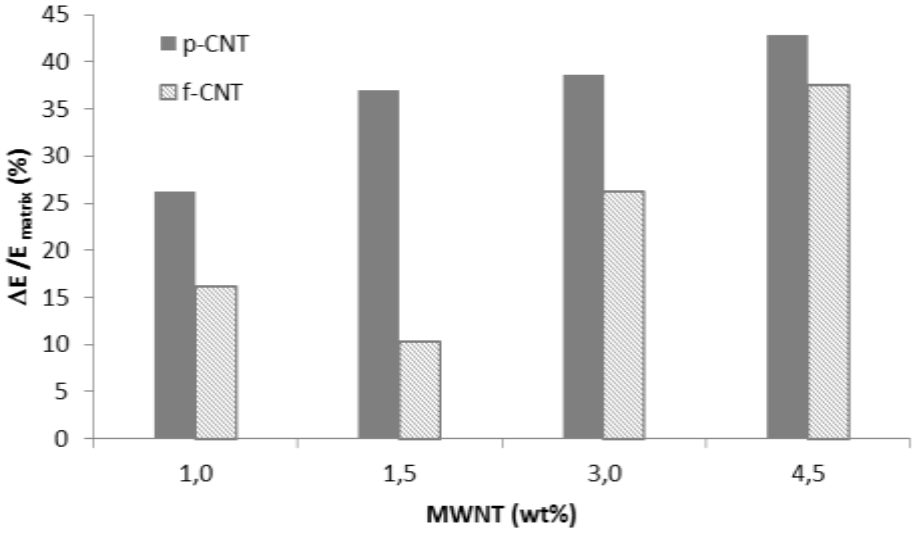

Figure 6.11 - Young's moduli variation for PA6/CNT composites relative to the neat polymer.

6.4. Conclusions

PA6 composites with CNT, as received and functionalized, were prepared by melt blending on a mini twin-screw extruder and small specimens were produced by μIM.

The composites obtained after extrusion and μIM were characterized in terms of their morphology, measuring the CNT agglomerates size and number and observing the dispersed CNT, to contribute to the interpretation of the electrical resistivity and tensile properties results.

The composites with p-CNT showed, in general, a smaller number of larger agglomerates compared to f-CNT.

The tensile strength, elongation at break and modulus of the nanocomposites were significantly improved by the addition of CNT. The type of processing strongly affected the electrical conductivity of the nanocomposites. The specimens produced presented electrical conductivity in the semiconductor range.

7. CONCLUSIONS

This thesis aimed to relate the properties of microinjected PA6/CNT nanocomposites and the development of a non-aggressive functionalization method in order to increase the CNT reactivity, improving the CNT/polymer interface and helping their dispersion into the polyamide matrix.

The modification of CNT using the 1,3-dipolar cycloaddition of an azomethine ylide to CNT was described in Chapter 3. The reaction was successful achieved even after a short reaction time and a relatively low reaction temperature under solvent-free conditions.

The concentration of the two products, namely a cyclic benzyl carbamate and a pyrrolidine and the reaction yield varied with reaction temperature and time.

This simple, solvent-free chemical procedure yields CNT with fine-tuned surface functionality.

This approach is promising towards the modification of CNT with reactive groups and is compatible with current industrial processes.

In the Chapter 4, the morphology and structure of samples produced by melt extrusion and μIM of PA6 was compared. α- and γ-phases were found in PA6 samples prepared by both processing methods. The γ-phase was dominant in the skin of the microinjection moulded part, with larger contribution for these samples compared to extruded samples. The conditions used in microinjection molding lead to considerable orientation at the skin region, decreasing towards the core, while the extruded samples showed almost no orientation. The degree of crystallinity of the μIM part was lower compared to the extruded sample.

Chapter 5 describes the effect of CNT addition and microinjection molding on the thermal property of PA6. With CNT incorporation, the crystallization of PA6 becomes faster. However, this does not reflect in an increase of crystallization degree.

Furthermore, CNT promotes α-phase in the PA6/CNT nanocomposites produced by μIM while in μIM PA6 matrix the γ-phase prevails.

The orientation effect induced by μIM, mainly in the skin region for PA6, is reduced with the CNT incorporation even more when they are functionalized. However all samples produced by μIM presents some orientation that is observed throughout the sample.

Finally, the chapter 6 describes the effect of functionalization, extrusion and μIM on the CNT dispersion in PA6 and the influence on the properties of PA6/CNT nanocomposites. Initially, composites with as-received (p-CNT) or chemically functionalized CNT (f-CNT) were extruded and processed by μIM.

It was found that the microinjected composites with f-CNT presented improved dispersion, with smaller CNT agglomerate area ratio compared to the composites with p-CNT. The f-CNT showed better adhesion to PA6 compared to p-CNT. The tensile strength, elongation at break and modulus of the nanocomposites were significantly improved by the addition of CNT. The experiments showed that the moulding geometry and processing conditions significantly affected electrical resistivity. The specimens produced presented electrical conductivity in the semiconductor range. The highest electrical conductivity was found for tensile specimens in the flow direction.

In summary, the functionalization of CNT can effectively enhance the interface between the CNT and PA6, as well as improve the CNT dispersion through the matrix improving the mechanical properties of the nanocomposites.

This study also provides a fundamental understanding of μIM effect imposed on PA6 and PA6/CNT nanocomposites.

REFERENCES

1. Iijima S. Helical microtubules of graphitic carbon. *Nature*, 1991, 354 (6348), 56-8.
2. Shaffer MSP, Sandler JKW. Chapter 1-Carbon Nanotube/Nanofibre Polymer Composites In: Advani SG (ed) Processing and properties of nanocomposites, World Scientific Publishing Company, USA 2006.
3. Guo T, Nikolaev P, Thess A, Colbert DT, Smalley RE. Catalytic growth of single-walled nanotubes by laser vaporization. *Chem Phys Lett* 1995, 243, 49–54.
4. Kong J, Cassell AM, Dai H. Chemical vapor deposition of methane for single-walled carbon nanotubes. *Chemical Physics Letters* 1998, 292, 567–574.
5. Huang SM, Woodson M, Smalley RE, Liu J. Growth mechanism of oriented long single walled carbon nanotubes using fast-heating chemical vapor deposition process. *Nano Lett* 2004, 4, 1025–8.
6. Nikolaev P, Bronikowski MJ, Bradley RK, Rohmund F, Colbert DT, Smith KA, Smalley RE. Gas-phase catalytic growth of single-walled carbon nanotubes from carbon monoxide. *Chem Phys Lett* 1999, 313, 91–7.
7. Iijima S, Ichihashi T. Single-shell carbon nanotubes of 1nm diameter. *Nature* 1993, 363, 603-605.
8. Bethune DS, Kiang CH, de Vries MS, Gorman G, Savoy R, Vazquez J, Beyers R. Cobalt-catalysed growth of carbon nanotubes with single-atomic-layer walls. *Nature* 1993, 363, 605-607.
9. Tasis D, Tagmatarchis N, Georgakilas V, Prato M. Soluble Carbon Nanotubes. *Chem. Eur. J.* 2003, 9, 4000-4008.
10. Thess A, Lee R, Nikolaev P, Dai H, Petit P, Robert J, Xu C, Lee YH, Kim SG, Rinzler AG, Colbert DT, Scuseria GE, Tománek D, Fischer JE, Smalley RE. Crystalline ropes of metallic carbon nanotubes. *Science* 1996, 273, 483-487.
11. Singh I, Rehni AK, Kumar P, Kumar M, Aboul-Enein HY. Carbon Nanotubes: Synthesis, Properties and Pharmaceutical Applications. *Fullerenes, Nanotubes and Carbon Nanostructures*, 17: 361–377, 2009.
12. Balasubramanian K, Burghard M. Chemically Functionalized Carbon Nanotubes. *Small* 2005, 1(2), 180–192.

13. Saito R, Fujita M, Dresselhaus G, Dresselhaus MS. Electronic structure of chiral graphene tubules. *Appl. Phys. Lett*. 1992, 60(18), 2204–2206.
14. Tanaka K, Aoki H, Ago H, Yamabe T, Okahara K. Interlayer interaction of two graphene sheets as a model of double-layer carbon nanotubes. *Carbon* 1997, 35(1), 121–125.
15. Nardelli MB, Yakobson BI, Bernholc J. Mechanism of strain release in carbon nanotubes. *Phys. Rev. B* 1998, 57, 4277–4280.
16. Charlier JC. Defects in Carbon Nanotubes *Acc. Chem. Res.* 2002, 35, 1063-1069.
17. Fischer JE, Dai H, Thess A, Lee R, Hanjani NM, Dehaas DL, Smalley RE. Metallic resistivity in crystalline ropes of single-wall carbon nanotubes. *Phys. Rev. B* 1997, 55(8), 4921–4924.
18. Ebbesen TW, Lezec HJ, Hiura H, Bennett JW, Ghaemie HF, Thio T. Electrical conductivity of individual carbon nanotubes. *Nature* 1996, 382, 54–56.
19. Odom TW, Huang JL, Kim P, Lieber CM. Atomic structure and electronic properties of single-walled carbon nanotubes. *Nature* 1998, 391, 62–64.
20. Kim P, Shi L, Majumdar A, McEuen PL. Thermal transport measurements of individual multiwalled nanotubes. *Phys. Rev. Lett.* 2001, 87, 215502.
21. Berber S, Kwon YK, Tománek D. Unusually High Thermal Conductivity of Carbon Nanotubes, *Phys. Rev. Lett.* 84, 2000, 4613–4616.
22. Treacy MMJ, Ebbesen TW, Gibson JM., Exceptionally high Young's modulus observed for individual carbon nanotubes, Nature 381, 1996, 678–680.
23. Yu MF, Files BS, Arepalli S, Ruoff RS. Tensile Loading of Ropes of Single Wall Carbon Nanotubes and their Mechanical Properties. *Phys Rev Lett* 2000, 84, 5552-5555.
24. Krishnan A, Dujardin E, Ebbesen TW, Yianilos PN, Treacy MMJ. Young's modulus of single-walled nanotubes. *Phys. Rev. B* 1998, 58(20), 14013–14019.
25. Yu MF, Lourie O, Dyer MJ, Moloni K, Kelly TF, Ruoff RS. Strength and breaking mechanism of multiwalled carbon nanotubes under tensile load. *Science* 2000, 287, 637-640.
26. Sahoo NG, Rana S, Cho JW, Li L, Chan SH. Polymer nanocomposites based on functionalized carbon nanotubes. *Progress in Polymer Science* 2010, 35, 837–867.
27. Iijima S, Brabec C, Maiti A, Bernholc J. Structural flexibility of carbon nanotubes. *J. Chem. Phys.* 1996, 104 (5), 2089-2092.
28. Nanocyl. Data sheet Nanocyl 7000. Sambreville, Belgium, 2009.
29. Bayer MaterialScience AG. Data sheet Baytubes_ C150P.Edition 2009-02-24; 2009.
30. FutureCarbon. Productinformation; 2009.

31. Arkema. Technical Data Sheet Graphistrength_ C100; September 2008 – Rev.4.
32. Zhao Q, Gan Z, Zhuang Q. Electrochemical Sensors Based on Carbon Nanotubes. *Electroanalysis* 2002, 14, 23, 1609-1613.
33. Gao B, Kleinhammes A, Tang XP, Bower C, Fleming L, Wu Y, Zhou O. Electrochemical intercalation of single-walled carbon nanotubes with lithium. *Chem Phys Lett* 1999, 307, 153–157
34. Endo M, Hayashi T, Kim YA, Terrones M, Dresselhaus MS. Applications of carbon nanotubes in the twenty-first century. *Phil. Trans. R. Soc. Lond. A* 2004, 362, 2223–2238.
35. Martel R, Schmidt T, Shea HR, Hertel T, Avouris Ph. Single- and multi-wall carbon nanotube field-effect transistors, *Appl. Phys. Lett*. 1998, 73, 2447-2449.
36. Tans SJ, Verschueren ARM, Dekker C. *Nature* 1998, Room-temperature transistor based on a single carbon nanotube, 393, 49-52.
37. Anantram MP, Léonard F, Physics of carbon nanotube electronic devices, *Rep. Prog. Phys.* 2006, 69, 507–561.
38. Leea NS, Chungb DS, Hana IT, Kangb JH, Choib YS, Kim HY, Parkb SH, Jina YW, Yib WK, Yunb MJ, Jungb JE, Leec CJ, You JH, Joc SH, Leec CG, Kim JM. Application of carbon nanotubes to field emission displays. *Diamond and Related Materials* 2001, 10, 265-270.
39. Baughman RH, Zakhidov AA, Heer WA. Carbon Nanotubes—the Route Toward Applications, *Science* 2002, 297, 787-792.
40. Oriňakova R, Oriňak A. Recent applications of carbon nanotubes in hydrogen production and storage. *Fuel* 2011, 90, 3123–3140.
41. Kong NR, Franklin C, Zhou MC, Chapline S, Peng K, Cho HD. Nanotube Molecular Wires as Chemical Sensors. *Science* 2000, 287(622), 406–415.
42. Ajayan P, Zhou O. In: Mildred S. Dresselhaus MS, Dresselhaus G, Avouris P (ed) Carbon Nanotubes Synthesis, Structure, Properties, Springer 2001, 391–425.
43. Endo M, Strano MS, Ajayan PM. In: Jorio A, Dresselhaus G, Dresselhaus MS (Eds.): Carbon Nanotubes- Advanced Topics in the Synthesis, Structure, Properties and Applications, Springer-Verlag Berlin Heidelberg 2008111, 13–62
44. Endo M, Koyama S, Matsuda Y, Hayashi T, Kim YA. Thrombogenicity and blood coagulation of a micro-catheter prepared from carbon nanotubenylon based composite. *Nano Lett*. 2005, 5, 101–106.

45. Ma PC, Kim JK (ed). Carbon Nanotubes for Polymer Reinforcement, CRC Press, Taylor and Francis Group, 2011.

46. Roya N, Senguptaa R, Bhowmick AK, Modifications of carbon for polymer composites and nanocomposites. *Progress in Polymer Science* 2012, 37 (6), 781-819.

47. Hirsch A, Vostrowsky O. In: Schlüter AD (ed), Functional Molecular Nanostructures, Springer 2005, 193–237.

48. Bahr JL, Tour JM. Covalent chemistry of single-wall carbon nanotubes. *J.Mater. Chem*. 2002, 12, 1952-1958.

49. Tasis D, Tagmatarchis N, Bianco A, Prato M. Chemistry of carbon nanotubes. *Chem. Rev*. 2006, 106, 1105-1136.

50. Ma PC, Siddiqui NA, Marom G, Kim JK. Dispersion and functionalization of carbon nanotubes for polymer-based nanocomposites: A review. *Composites: Part A* 2010, 41, 1345–1367.

51. Mickelson ET, Huffman CB, Rinzler AG, Smalley RE, Hauge RH, Margrave JL. Fluorination of single-wall carbon nanotubes. *Chem Phys Lett* 1998, 296, 188–194.

52. Stevens JL, Huang AY, Peng H, Chiang IW, Valery N. Khabashesku VN, Margrave JL. Sidewall amino-functionalization of SWNT through fluorination and subsequent reactions with terminal diamines. *Nano Lett* 2003, 3, 331–336.

53. Delgado JL, Cruz P, Langa F, Urbina A, Casado J, Navarrete JTL. Microwave-assisted sidewall functionalization of single-wall carbon nanotubes by Diels–Alder cycloaddition. *Chem. Commun*. 2004, 1734–1735.

54. Holzinger M, Vostrowsky O, Hirsch A, Hennrich F, Kappes M, Weiss R, Jellen F. Sidewall Functionalization of Carbon Nanotubes *Angew. Chem. Int. Ed*. 2001, 40, 4002-4005.

55. Holzinger M, Abraham J, Whelan P, Graupner R, Ley L, Hennrich F, Kappes M, Hirsch A. Functionalization of Single-Walled Carbon Nanotubes with (R-) Oxycarbonyl Nitrenes *J. Am. Chem. Soc.* 2003, 125, 8566–8580.

56. Georgakilas V, Kordatos K, Prato M, Guldi DM, Holzinger M, Hirsch A. Organic Functionalization of Carbon Nanotubes. *J Am Chem Soc* 2002, 124 (5),760-761.

57. Liu P. Modifications of carbon nanotubes with polymers. *Eur Polym J* 2005, 41, 2693–703.

58. Qin S, Qin D, Ford WT, Resasco DE, Herrera JE. Functionalization of Single-Walled Carbon Nanotubes with Polystyrene via Grafting to and Grafting from Methods. *Macromolecules* 2004, 37, 752-757.

59. Hwang GL, Shieh YT, Hwang KC. Efficient Load Transfer to Polymer-Grafted Multiwalled Carbon-Nanotubes in Polymer Composites. *Adv. Funct. Mater*. 2004, 14, 487-491.

60. Kong H, Gao C, Yan D. Controlled Functionalization of Multiwalled Carbon Nanotubes by in Situ Atom Transfer Radical Polymerization. *J. Am. Chem. Soc*. 2004, 126, 412-413

61. Lou X, Detrembleur C, Sciannamea V, Pagnoulle C, Jerome R. Grafting of alkoxyamine end-capped (co) polymers onto multi-walled carbon nanotubes. *Polymer* 2004, 45, 6097-6102.

62. Esumi K, Ishigami M, Nakajima A, Sawada k, Honda H. Chemical treatment of carbon nanotubes. *Carbon* 1996, 34, 279–81.

63. Yu R, Chen L, Liu Q, Lin J, Tan KL, Ng SC, Chan HSO, Xu GQ, Andy Hor TS. Platinum deposition on carbon nanotubes via chemical modification. *Chem Mater* 1998, 10, 718–22.

64. Sham ML, Kim JK. Surface functionalities of multi-wall carbon nanotubes after UV/ozone and TETA treatments. *Carbon* 2006, 44, 768–77.

65. Ma PC, Kim JK, Tang BZ. Functionalization of carbon nanotubes using a silane coupling agent. *Carbon* 2006, 44, 3232–8.

66. Hamon MA, Hui H, Bhowmik P. Ester-functionalized soluble single-walled carbon nanotubes. *Appl Phys A* 2002, 74, 333–8.

67. Li J, Fang Z, Tong L, Gu A, Liu F. Improving Dispersion of Multiwalled Carbon Nanotubes in Polyamide 6 Composites Through Amino-Functionalization. *J Appl Polym Sci* 2007, 106, 2898–2906.

68. Lin Y, Rao AM, Sadanadan B, Kenik EA, Sun YP. Functionalizing Multiple-Walled Carbon Nanotubes with Aminopolymers. *J. Phys. Chem. B* 2002, 106, 1294-1298.

69. Liu J, Rinzler AG, Dai HJ, Hafner JH, Bradley RK, Boul PJ, Lu A, Iverson T, Shelimov K, Huffman CB, Macias FR, Shon YS, Lee TR, Colbert DT, Smalley RE. Fullerene pipes. *Science* 1998, 280, 1253–6.

70. Stephenson JJ, Sadana AK, Higginbotham AL, Tour JM. Highly functionalized and soluble multiwalled carbon nanotubes by reductive alkylation and arylation: the billups reaction. *Chem Mater* 2006, 18, 4658–61.

71. Osorio AG, Silveira ICL, Bueno VL, Bergmann CP, H_2SO_4/HNO_3/HCl—Functionalization and its effect on dispersion of carbon nanotubes in aqueous media, *Applied Surface Science* 2008, 255, 2485–2489.

72. Zhang J, Zou H, Qing Q, Yang Y, Li Q, Liu Z, Guo X, Du Z. Effect of Chemical Oxidation on the Structure of Single-Walled Carbon Nanotubes. *J. Phys. Chem. B* 2003, 107, 3712-3718.

73. Tagmatarchis N, Prato M. Functionalization of carbon nanotubes via 1,3-dipolar cycloadditions *J. Mater. Chem*. 2004, 14, 437-439.

74. Campidelli S, Sooambar C, Diz EL, Elhi C, Guldi DM, Prato M. Dendrimer-Functionalized Single-Wall Carbon Nanotubes: Synthesis, Characterization, and Photoinduced Electron Transfer. *J. Am. Chem. Soc.*2006, 128, 12544-12552.

75. Brunetti FG, Herrero MA, Munoz JM, Giordani S, Diaz-Ortiz A, Filippone S, Ruaro G, Meneghetti M, Prato M, Vazquez E. Reversible microwave-assisted cycloaddition of aziridines to carbon nanotubes. *J. Am. Chem. Soc*. 2007, 129, 14580–14581.

76. Araújo R, Paiva MC, Proença MF, Silva CJR. Functionalization of carbon nanofibers by 1,3-dipolar cycloaddition reactions and its effect on composite properties. *Composite Science and Technology* 2007, 67, 806-810.

77. Paiva MC, Novais RM, Araújo RF, Pederson KK, Proença MF, Silva CJR, Costa CM, Lanceros-Méndez S. Organic functionalization of carbon nanofibers for composite applications. *Polymer Composites* 2010, 31, 369–376.

78. Star A, Stoddart JF, Steuerman D, Diehl M, Boukai A, Wong EW, Yang X, Chung SW, Choi H, Heath JR. Preparation and properties of polymer-wrapped single-walled carbon nanotubes. *Angew Chem Int Ed* 2001, 40, 1721–5.

79. Hill DE, Lin Y, Rao AM, Allard LF, Sun YP. Functionalization of carbon nanotubes with polystyrene. *Macromolecules* 2002, 35, 9466–71.

80. Gong X, Liu J, Baskaran S, Voise RD, Young JS. Surfactant-assisted processing of carbon nanotube/polymer composites. *Chem Mater* 2000, 12, 1049–52.

81. Yu J, Grossiord N, Koning CE, Loos J. Controlling the dispersion of multi-wall carbon nanotubes, in aqueous surfactant solution. *Carbon* 2007, 45, 618–23.

82. Tan Y, Resasco DE. Dispersion of single-walled carbon nanotubes of narrow diameter distribution. *J Phys Chem B* 2005, 109, 14454–60.

83. Islam MF, Rojas E, Bergey DM, Johnson AT, Yodh AG. High weight fraction surfactant solubilization of single-wall carbon nanotubes in water. *Nano Lett* 2003, 3, 269–73.

84. Georgakilas V, Gournis D, Tzitzios V, Pasquato L, Guldi DM, Prato M. Decorating carbon nanotubes with metal or semiconductor nanoparticles. *J Mater Chem* 2007, 17, 2679–94.

85. Davis JJ, Green MLH, Hill OAH, Leung YC, Sadler PJ, Sloan J, Xavier AV, Tsang SC. The immobilisation of proteins in carbon nanotubes. *Inorg.Chim.Acta* 1998, 272, 261.

86. Coleman JN, Khan U, Blau W, Gun'ko Y. Small but strong: A review of the mechanical properties of carbon nanotube–polymer composites. *Carbon* 2006, 44 1624–1652.

87. Spitalsky Z, Tasis D, Papagelis K, Galiotis C. Carbon nanotube–polymer composites: Chemistry, processing,mechanical and electrical properties. *Progress in Polymer Science* 2010, 35, 357–401.

88. Park SJ, Cho MS, Lim ST, Choi HJ, Jhon MS. Synthesis and Dispersion Characteristics of Multi-Walled Carbon Nanotube Composites with Poly(methyl methacrylate) Prepared by In-Situ Bulk Polymerization. *Macromol. Rapid Commun.* 2003, 24, 1070–1073.

89. Funck A, Kaminsky W. Polypropylene carbon nanotube composites by in situ polymerization, *Composites Science and Technology* 2007, 67, 906–915.

90. Zhao C, Hu G, Justice R, Schaefer DW, Zhang S, Yang M, Han CC. Synthesis and characterization of multi-walled carbon nanotubes reinforced polyamide 6 via in situ polymerization. *Polymer* 2005, 46(14), 5125–32.

91. Yanga M, Hana CC. Synthesis and characterization of multi-walled carbon nanotubes reinforced polyamide 6 via in situ polymerization, *Polymer* 2005, 46, 5125–5132.

92. Park C, Ounaies Z, Watson KA, Crooks RE, Smith J, Lowther SE, Connell JW, Siochi EJ, Harrison JS, Clair TLS, Dispersion of single wall carbon nanotubes by in situ polymerization under sonication, *Chemical Physics Letters* 2002, 364, 303–308.

93. Moore VC, Strano MS, Haroz EH, Hauge RH, Smalley RE, Schmidt J, Talmon Y. Individually suspended single-walled carbon nanotubes in various surfactants. *Nano Lett* 2003, 3, 1379–82.

94. Li C, Pang XJ, Qu MZ, Zhang QT, Wang B, Zhang BL, Yu ZL. Fabrication and characterization of polycarbonate/carbon nanotubes composites. *Compos Part A* 2005, 37,1485–9.

95. Kearns JC, Shambaugh RL. Polypropylene fibers reinforced with carbon nanotubes. *J Appl Polym Sci* 2002, 86, 2079–84.

96. Sahoo NG, Jung YC, Yoo HJ, Cho JW. Effect of functionalized carbon nanotubes on molecular interaction and properties of polyurethane composites. *Macromol Chem Phys* 2006, 207, 1773–80.

97. Safadi B, Andrews R, Grulke EA. Multiwalled Carbon Nanotube Polymer Composites: Synthesis and Characterization of Thin Films. *J. Appl. Polym.Sci.*2002*,* 84, 2660.

98. Geng H, Rosen R, Zheng B, Shimoda H, Fleming L, Liu J, Zhou O. Fabrication and properties of composites of poly(ethylene oxide) and functionalized carbon nanotubes. *Adv Mater* 2002, 14, 1387–90.

99. Du F, Fischer JE, Winey KI. Coagulation method for preparing single walled carbon nanotube/poly(methyl methacrylate) composites and their modulus, electrical conductivity, and thermal stability. *J Polym Sci B* 2003, 41, 3333–8.
100. Sundararaj U, Macosko CW, Nakayama A, Inoue T. Milligrams to kilograms: an evaluation of mixers for reactive polymer blending. *Polym Eng Sci* 1995, 35(1), 100-114.
101. Lin B, Sundararaj U, Pötschke P. Melt mixing of polycarbonate with multi-walled carbon nanotubes in miniature mixers. *Macromol Mater Eng* 2006, 291, 227-238.
102. Maric M, Macosko CW. Improving polymer dispersions in mini-mixers. *Polym Eng Sci* 2001, 41(1), 118-130.
103. Gale M. Compounding with single screw extruders. *Adv. Poly. Tech.* 1997, 16(4), 251-262.
104. Novais RM, Covas JA, aiva MC. The effect of flow type and chemical functionalization on the dispersion of carbon nanofiber agglomerates in polypropylene. *Composites: Part A* 2012, 43, 833–841.
105. Zhang WD, Shen L, Phang IY, Liu T. Carbon nanotubes reinforced nylon-6 composite prepared by simple melt-compounding. *Macromolecules* 2004, 37, 256–9.
106. Villmow T, Pötschke P, Pegel S, Häussler L, Kretzschmar B, Influence of twin-screw extrusion conditions on the dispersion of multi-walled carbon nanotubes in a poly(lactic acid) matrix, *Polymer* 2008, 49, 3500–3509.
107. Villmow T, Kretzschmar B, Pötschke P. Influence of screw configuration, residence time, and specific mechanical energy in twin-screw extrusion of polycaprolactone/multi-walled carbon nanotube composites. *Compos Sci Technol* 2010, 70(14),2045–55.
108. Kasaliwal GR, Göldel A, Pötschke P, Heinrich G. Influences of polymer matrix melt viscosity and molecular weight on MWNT agglomerate dispersion. *Polymer* 2011, 52, 1027-1036.
109. Andrews R, Jacques D, Qian D, Rantell T. Multiwall Carbon Nanotubes: Synthesis and Application. *Acc. Chem. Res*. 2002, 35, 1008-1017.
110. Haggenmueller R, Gommans HH, Rinzler AG, Fischer JE, Winey KI. Aligned single-wall carbon nanotubes in composites by melt processing methods. *Chemical Physics Letters* 2000, 330, 219-225.
111. King JA, Tucker KW, Meyers JD, Weber EH, Clingerman ML, Ambrosius KR. Factorial Design Approach Applied to Electrically and Thermally Conductive Nylon 6,6. *Polym. Compos.*, 2001, 22, 142.

112. Piotter V, Mueller K, Plewa K, Ruprecht R, Hausselt J. Performance and simulation of thermoplastic microinjection molding. *Microsyst. Technol*. 2002, 8, 387–90.

113. Tosello G, Hansen HN In: Qin Y (ed), Micro-Manufacturing Engineering and Technology 1st edn, Elsevier, United Kingdom, 2010 90-113.

114. Sha B, Dimov S, Griffiths C, Packianather MS. Investigation of micro-injection moulding: Factors affecting the replication quality, *J. Mater. Process. Technol.* 2007, 183, 284–296.

115. Whiteside BR, Martyn MT, Coates PD, Allan PS, Hornsby PR, Greenway G. Micromoulding: process characteristics and product properties. *Plast. Rubber Compos.* 2003 32 231–9.

116. Ruprecht R, Gietzelt T, Müller K, Piotter V, Haußelt J. Injection molding of microstructured components from plastics, metals and ceramics. *Microsystem Technologies* 2002, 8, 351-358.

117. Heckele M, Bacher W, Müller KD. Hot embossing-The molding technique for plastic microstructures, *Microsystem Technologies* 1998, 4, 122-124.

118. Truckenmüller R, Giselbrecht S, Rivron N, Gottwald E, Saile V, Berg A, Blitterswijk MWC, Thermoforming of Film-Based Biomedical Microdevices. *Adv. Mater*. 2011, 23, 1311–1329.

119. Yao D, Kim B. Injection molding high aspect ratio microfeatures. *J Inject Molding Technol* 2002, 6(1), 11–17.

120. Attia UM, Marson S, Alcock JR. Micro-injection moulding of polymer microfluidic devices. *Microfluid Nanofluid* 2009, 7:1–28.

121. Julien G, Copponnex T, Mélé P. Microinjection molding of thermoplastic polymers: morphological comparison with conventional injection molding. *J. Micromech. Microeng*. 2009, 19, 025023.

122. Yao D. In: Thomas S, Weimin Y. (ed) Advances in polymer processing: from macro to nano, Woodhead Publishing 2009, 17, 552.

123. Lei Xie, Gerhard Ziegmann, A visual mold with variotherm system for weld line study in micro injection molding, Microsyst Technol (2008) 14:809–814.

124. Fu G, Loh N H, Tor S B, Tay B Y, Murakoshi Y and Maeda R 2005 A variotherm mold for micro metal injection molding Microsyst. Technol. 11 1267–71.

125. Julien G, Copponnex T, Mélé P. Microinjection molding of thermoplastic polymers: a review. *J. Micromech. Microeng*. 2007, 17, R96–R109.

126. Yao D, Pratapkumar N, Li L, Allen Y. A strategy for rapid thermal cycling of molds in thermoplastic processing. *J Manuf Sci Eng* 2006,128, 4, 837-843.

127. Yao D, Kim B. Scaling issues in miniaturization of injection molded parts, *J Manuf. Sci. Eng*. 2004, 126, 733–739.

128. Su YC, Shah J, Lin LW. Implementation and analysis of polymeric microstructure replication by micro injection molding. *J. Micromech. Microeng.* 2004, 14, 415–422.
129. Trotta G, Surace R, Modica F, Spina R, Fassi I. Micro Injection Moulding of Polymeric Components, *AIP Conf. Proc.* 2011, 1315, 1273.
130. Pirskanen J, Immonen J, Kalima V, Pietarinen J, Siitonen S, Kuittinen M, Mönkkönen K, Pakkanen T, Suvanto M, Pääkkönen EJ. Replication of sub-micrometre features using microsystems technology. *Plast Rubber Compos* 2005, 34, 222–226.
131. Ong NS, Koh YH. Experimental Investigation Into Micro Injection Molding Of Plastic Parts. *Materials and Manufacturing Processes* 2005, 20: 245–253.
132. boy.ltd.uk
133. Chena SC, Wanga YC, Liua SC, Cina JC. Mold temperature variation for assisting micro-molding of DVD micro-featured substrate and dummy using pulsed cooling. *Sensors and Actuators A* 2009, 151, 87–93.
134. Tseng SC, Chen YC, Kuo CL, Shew BY. A study of integration of LIGA and m-EDM technology on the microinjection molding of ink-jet printers' nozzle plates. *Microsyst. Technol.* 2005, 12 116–9.
135. Ong NS, Koh YH, Fu YQ. Microlens array produced using hot embossing process. Microelectron. Eng. 2002, 60, 365–9.
136. Lehmacher S, Neyer A, Mederer F. Polymer optical waveguides integrated in printed circuit boards Proc. 27th European Conf. Optical Communication, 2001, 3, 302–3.
137. Yu PC, Li QF, Fuh JYH, Li T, Ho PW. Micro injection molding of micro gear using nano-sized zirconia powder. *Microsyst Technol* 2009, 15, 401–406.
138. Krabe D, Scheel W. Optical interconnects by hot embossing for module and PCB technology—the EOB approach- Proc. 49th Electronic Components and Technology Conference 1999, 1164–6.
139. Kurosawa M, Haga S, Yamasato H, Kobayashi I, Suzuki S. PET emboss membrane switch Fujikura *Tech. Rev.* 1995, 24 97–100.
140. Heckele M, Schomburg WK. Review on micro molding of thermoplastic polymers. *J. Micromech. Microeng.* 2004, 14 R1–R14.
141. www.micromanufacturing.net/
142. Celzard A, McRae E, Deleuze C, Dufort M, Furdin G, Mareche JF. Critical concentration in percolating systems containing a high-aspect-ratio filler. *Physical Review B: Condensed Matter* 1996, 53, 6209–14.

143. Munson-McGee SH. Estimation of the critical concentration in an anisotropic percolation network *Physical Review B: Condensed Matter* 1991, 43,3331–6.

144. Bryning MB, Islam MF, Kikkawa JM, Yodh AG. Very Low Conductivity Threshold in Bulk Isotropic Single-Walled Carbon Nanotube–Epoxy *Composites Advanced Materials* 2005, 17,1186–91.

145. Sandler JKW, Kirk JE, Kinloch IA, Shaffer MSP, Windle AH. Ultra-low electrical percolation threshold in carbon-nanotube-epoxy composites. *Polymer* 2003, 44, 5893–9.

146. Sanjinés R, Abad MD, Vâju Cr, Smajda R, Mionić M, Magrez A. Electrical properties and applications of carbon based nanocomposite materials: An overview. *Surface & Coatings Technology* 2011, 206 727–733.

147. Pötschke P, Fornes TD, Paul DR, Rheological behavior of multiwalled carbon nanotube/polycarbonate composites. *Polymer* 2002, 43, 3247.

148. Bin Y, Mine M, Ai K, Jiang X, Masaru M. Morphology and mechanical and electrical properties of oriented PVA–VGCF and PVA–MWNT composites. *Polymer* 2006, 47, 1308–17.

149. Al-Saleh MH, Sundararaj U. A review of vapor grown carbon nanofiber/polymer conductive composites. *Carbon* 2009, 47, 2-22.

150. Li J, Ma PC, Chow WS, To CK, Tang BZ, Kim JK. Correlations between percolation threshold, dispersion state, and aspect ratio of carbon nanotubes. *Adv Funct Mater* 2007,17, 3207–15.

151. Bauhofer W, Kovacs JZ. A review and analysis of electrical percolation in carbon nanotube polymer composites. *Compos Sci Technol* 2009, 69, 1486–98.

152. Ramasubramaniam R, Chen J, Liu H. Homogeneous carbon nanotube/ polymer composites for electrical applications. *Appl Phys Lett* 2003, 83, 2928–30.

153. Yan KY, Xue QZ, Zheng QB, Hao LZ. The interface effect of the effective electrical conductivity of carbon nanotube composites. *Nanotechnology* 2007, 18(25), 255705.

154. Coleman JN, Curran S, Dalton AB, Davey AP, McCarthy B, Blau W, Barklie RC. Percolation-dominated conductivity in a conjugated-polymer–carbon nanotube composite. *Phys Rev B* 1998, 58(12), R7492–5.

155. Hornbostel B, Pötschke P, Kotz J, Roth S. Single-walled carbon nanotubes/polycarbonate composites: basic electrical and mechanical properties. *Phys. Stat. Sol. (b)* 2006, 243, 13, 3445–3451.

156. Gorrasi J, Sarno M, Di Bartolomeo A, Sannino D, Ciambelli P, Vittoria V. Incorporation of carbon nanotubes into polyethylene by high energy ball milling: morphology and physical properties. *J Polym Sci B* 2007, 45, 597–606.

157. Mičušik M, Omastova M, Krupa I, Prokeš J, Pissis P, Logakis E, Pandis C, Pötschke P, Pionteck J. A comparative study on the electrical and mechanical behaviour of multi-walled carbon nanotube composites prepared by diluting a masterbatch with various types of polypropylene. *J Appl Polym Sci* 2009, 113, 2536–51.

158. Kodgire PV, Bhattacharyya AR, Bose S, Gupta N, Kulkarni AR, Misra A. Control of multiwall carbon nanotubes dispersion in polyamide 6 matrix: an assessment through electrical conductivity. *Chem Phys Lett* 2006, 432, 480–5.

159. Meincke O, Kaempfer D, Weickmann H, Friedrich C, Vathauer M, Warth H. Mechanical properties and electrical conductivity of carbon-nanotube filled polyamide-6 and its blends with acrylonitrile/butadiene/styrene. *Polymer* 2004, 45, 739–748.

160. Krause B, Pötschke P, Hauser L. Influence of small scale melt mixing conditions on electrical resistivity of carbon nanotube–polyamide composites. *Compos Sci Technol* 2009, 69, 1505–15.

161. Manchado MAL, Valentini L, Biagiotti J, Kenny JM. Thermal and mechanical properties of single-walled carbon nanotubes-polypropylene composites prepared by melt processing. *Carbon* 2005, 43(7), 1499–505.

162. Thostenson ET, Chou TW. Aligned multi-walled carbon nanotube-reinforced composites: processing and mechanical characterization. *J. Phys. D: Appl. Phys.* 2002, 35, L77-L80.

163. Liu T, Phang I, Shen L, Chow S, Zhang W. Morphology and Mechanical Properties of Multiwalled Carbon Nanotubes Reinforced Nylon-6 Composites. *Macromolecules* 2004, 37, 7214-7222.

164. Liu H, Wang X, Fang P, Wang S, Qi X, Pan C, Xie G, Liew KM. Functionalization of multi-walled carbon nanotubes grafted with self-generated functional groups and their polyamide 6 composites. *Carbon* 2010, 48 721 –729

165. Biercuk MJ, Llaguno MC, Radosavljevic M, Hyun JK, Johnson AT. Carbon nanotube composites for thermal management. *Appl. Phys. Lett*. 2002, 80, 2767.

166. Cadek M, Coleman JN, Barron V, Hedicke K, Blau WJ. Morphological and mechanical properties of carbon-nanotube-reinforced semicrystalline and amorphous polymer composites. *Appl. Phys. Lett*., 2002, 81, 5123.

167. Liu XQ, Yang W, Xie BH, Yang MB. Influence of multiwall carbon nanotubes on the morphology, melting, crystallization and mechanical properties of polyamide 6/acrylonitrile–butadiene–styrene blends. *Materials and Design* 2012, 34, 355–362.

168. Wood JR, Zhao Q, Frogley MD, Meurs ER, Prins AD, Peijs T, Dunstan DJ, Wagner HD. Carbon nanotubes: from molecular to macroscopic sensors. *Phys. Rev. B*. 2000, 62, 7571.

169. Chen P, Kim HS, Jin HJ. Preparation, Properties and Application of Polyamide/Carbon Nanotube Nanocomposites. *Macromolecular Research* 2009, 17, 4, 207-217.
170. Thostenson ET, Chou TW. Processing-structure-multi-functional property relationship in carbon nanotube/epoxy composites. *Carbon* 2006, 44, 3022-3029.
171. ImageJ is a public domain available http://rsb.info.nih.gov/ij/download.html.
172. Le HH, Kasaliwal G, Ilisch S, Radusch HJ. Online measured electrical conductance. *Testing and Measuring* 2009, 326-333.
173. Kasaliwal G, Göldel A, Pötschke P. Influence of processing conditions in small-scale melt mixing and compression molding on the resistivity and morphology ofpolycarbonate–MWNT composites. *J Appl Polym Sci* 2009,112, 3494–3509.
174. Kasaliwal GR, Pegel S, Göldel A, Pötschke P, Heinrich G. Analysis of agglomerate dispersion mechanism of multiwalled carbon nanotubes during melt mixing in polycarbonate. *Polymer* 2010, 51, 2708-2720.
175. Pötschke P, Bhattacharyya AR, Janke A. Melt mixing of polycarbonate with multiwalled carbon nanotubes: microscopic studies on the state of dispersion. *Eur. Polym. J.* 2004, 40, 137–148.
176. Rastogi R, Kaushal R, Tripathi SK, Sharma AL, Kaur I, Bharadwaj LM. Comparative study of carbon nanotube dispersion using surfactants. *J Colloid Interface Sci* 2008, 328, 421–8.
177. Pötschke P, Bhattacharyya AR, Janke A. Carbon nanotube-filled polycarbonate composites produced by melt mixing and their use in blends with polyethylene. *Carbon* 2004, 42, 965-969.
178. Bellayer S, Gilman JW, Eidelman N, Bourbigot S, Flambard X, Fox DM, De Long HC, Trulove PC. Preparation of homogeneously dispersed multiwalled carbon nanotube/polystyrene nanocomposites via melt extrusion using trialkyl imidazolium compatibilizer, *Adv. Funct. Mater.* 2005, 15, 910–916.
179. Stoyan D, Kendall WS, Mecke J. Stochastic geometry and its applications. Chichester [U.A.]: Wiley; second edition, 1987.
180. Krause B, Boldt R, Pötschke P. A method for determination of length distributions of multiwalled carbon nanotubes before and after melt processing. *Carbon* 2011, 49,1243–1247.
181. Pegel S, Pötschke P, Villmow T, Stoyan D, Heinrich G. Spatial statistics of carbon nanotube polymer composites. *Polymer* 2009, 50, 2123–2132.
182. Haslam MD, Raeymaekers B. A composite index to quantify dispersion of carbon nanotubes in polymer-based composite materials. *Composites: Part B* 2013, 55, 16–21.

183. Eken AE, Tozzi EJ, Klingenberg DJ, Bauhofer W. A simulation study on the effects of shear flow on the microstructure and electrical properties of carbon nanotube/polymer composites. *Polymer* 2011, 52(22), 5178-5185.

184. Logakis E, Pandis Ch, Kyritsis A, Pissis P, Mičušik M, Omastova M, Pionteck J. Indirect methods for the determination of optimal processing conditions in conductive polypropylene/carbon nanotubes composites. Chem. Phys. Lett. 2010, 498, 125–128.

185. Kashiwagi T, Fagan J, Douglas JF, Yamamoto K, Heckert AN, Leigh SD, Obrzut J, Du F, Gibson SL, Mu M, Winey KI, Haggenmueller R. Relationship between dispersion metric and properties of PMMA/SWNT nanocomposites. *Polymer* 2007, 48, 4855-4866.

186. Shiga S, Furuta M. Processability of EPR in an internal mixter (II)-Morphological changes of carbon black agglomerates during mixing. Rubber Chem. Technol. 1985, 58(1),1-22.

187. Alig I, Pötschke P, Lellinger D, Skipa T, Pegel S, Kasaliwal GR, Villmow T. Establishment, morphology and properties of carbon nanotube networks in polymer melts, *Polymer* 2012, 53, 4-28

188. Kasaliwal GR, Göldel A, Pötschke P. Influence of Processing Conditions in Small-Scale Melt, Mixing and Compression Molding on the Resistivity and Morphology of Polycarbonate–MWNT Composites, *J Appl Polym Sci* 2009, 112, 3494–3509.

189. Hansen S, Khakhars DV, Ottino JM. Dispersion of solids in nonhomogeneous viscous flows, *Chem. Eng. Sci.* 1998, 53, 10, 1803-1817.

190. Barber AH, Cohen SR, Wagner HD. External and internal wetting of carbon nanotubes with organic liquids, Phys. Rev. B 2005, 71, 115443.

191. Pegel S, Pötschke P, Petzold G, Alig I, Dudkin SM, Lellinger D. Dispersion, agglomeration, and network formation of multiwalled carbon nanotubes in polycarbonate melts *Polymer* 2008, 49, 974-984.

192. Wu M, Shaw L. Electrical and Mechanical Behaviors of Carbon Nanotube-Filled Polymer Blends *J. Appl. Polym. Sci.* 2006, 99, 477.

193. Pötschke P, Pegel S, Claes M, Bonduel D. A Novel Strategy to Incorporate Carbon Nanotubes into Thermoplastic Matrices Macromol. *Rapid Commun*. 2008, 29, 244–251.

194. Andrews R, Jacques D, Minot M, Rantell T. Fabrication of carbon multiwall nanotube/polymer composites by shear mixing. *Macromol Mater Eng* 2002, 287(6), 395–403.

195. Müller MT, Krause B, Kretzschmar B, Pötschke P. Influence of feeding conditions in twin-screw extrusion of PP/MWNT composites on electrical and mechanical properties, *Compos. Sci. Technol.* 2011, 71, 1535–1542.

196. Tambe PB, Bhattacharyya AR, Kulkarni AR. The Influence of Melt-Mixing Process Conditions on Electrical Conductivity of Polypropylene/Multiwall Carbon Nanotubes Composites. *J. Appl. Polym. Sci*. 2013, 127, 1017–102.

197. Alig I, Skipa T, Lellinger D, Bierdel M, Meyer H. Destruction and formation of a carbon nanotube network in polymer melts: Rheology and conductivity spectroscopy. *Phys Status Solidi B* 2008, 245, 10, 2264-7.

198. Alig I, Skipa T, Lellinger D, Bierdel M, Meyer H. Dynamic percolation of carbon nanotube agglomerates in a polymer matrix: comparison of different model approaches. *Phys Status Solidi B* 2008, 245, 10, 2264–2267.

199. Bauhofer W, Schulz SC, Eken AE, Skipa T, Lellinger D, Alig I, Tozzi EJ, Klingenberg DJ. Shear - controlled electrical conductivity of carbon nanotubes networks suspended in low and high molecular weight liquids. *Polymer* 2010, 51(22), 5024-7.

200. Pan Y, Cheng HKF, Li L, Chan SH, Zhao J, Juay YK. Annealing induced electrical conductivity jump of multi-walled carbon nanotube/polypropylene composites and influence of molecular weight of polypropylene. *J Polym Sci Part B: Polym Phys* 2010, 48(21), 2238–47.

201. Tiusanen J, Vlasveld D, Vuorinen J. Review on the effects of injection moulding parameters on the electrical resistivity of carbon nanotube filled polymer parts. *Compos. Sci. Technol.* 2012, 72, 1741–1752

202. Alig I, Lellinger D, Engel M, Skipa T, Pötschke P. Destruction and formation of a conductive carbon nanotube network in polymer melts: in-line experiments. *Polymer* 2008, 49(7),1902–9.

203. Ma PC, Mo SY, Tang BZ, Kim JK. Dispersion, interfacial interaction and re-agglomeration of functionalized carbon nanotubes in epoxy composites. *Carbon* 2010, 48, 1824–1834.

204. Pujari S, Rahatekar SS, Gilman JW, Koziol KK, Windle AH, Burghardt WR. Orientation dynamics in multiwalled carbon nanotube dispersions under shear flow, *J. Chem. Phys*. 2009, 130, 214903.

205. Abbasi S, Carreau PJ, Derdouri A. Flow induced orientation of multiwalled carbon nanotubes in polycarbonate nanocomposites: rheology, conductivity and mechanical properties. *Polymer* 2010, 51(4), 922–35

206. Abbasi S, Derdouri A, Carreau PJ. Properties of Microinjection Molding of Polymer Multiwalled Carbon Nanotube Conducting Composites. *Polym. Eng. Sci.* 2011, 51, 992-1003.

207. Guo C, Liu FH, Wu X, Liu H, Zhang J. Morphological Evolution of HDPE Parts in the Microinjection Molding: Comparison with Conventional Injection Molding, *J. Appl. Polym. Sci.*, 2012, 126, 452–462.

208. Liu F, Guo C, Wu X, Qian X, Liu H, Zhang J. Morphological comparison of isotactic polypropylene parts prepared by micro-injection molding and conventional injection molding. *Polym. Adv. Technol.* 2012, 23 686–694.

209. Jorio A, Dresselhaus G, Dresselhaus MS. In: illustrated, editor. Carbon nanotubes: advanced topics in the synthesis, structure, properties and applications. Springer; 2008.

210. Rao AM, Jorio A, Pimenta MA, Dantas MSS, Saito R, Dresselhaus G, Dresselhaus MS. Polarized Raman Study of Aligned Multiwalled Carbon Nanotubes *Phys. Rev. Lett*. 2000, 84, 1820–1823.

211. Sandler JKW, Pegel S, Cadek M, Gojny F, Es M, Ohmar J, Blau WJ, Schulte K, Windle AH, Shaffer MSP. A comparative study of melt spun polyamide-12 fibres reinforced with carbon nanotubes and nanofibres. *Polymer* 2004, 45, 2001–2015

212. Endo M, Kim YA, Fukai Y, Hayashi T, Terrones M, Terrones H, Dresselhaus MS. Comparison study of semi-crystalline and highly crystalline multiwalled carbon nanotubes. *Appl Phys Lett* 2001, 79(10),1531–3.

213. Villmow T, Pegel S, Potschke P, Wagenknecht U. Influence of injection molding parameters on the electrical resistivity of polycarbonate filled with multi-walled carbon nanotubes. *Compos Sci Technol* 2008, 68 (3–4),777–89.

214. Chandra A, Kramschuster AJ, Hu X, Turng LS. Effect of injection molding parameters on the electrical conductivity of polycarbonate/carbon nanotube nanocomposites. *SPEANTEC Tech*; 2007, 2184–8.

215. Lellinger D, Xu D, Ohneiser A, Skipa T, Alig I. Influence of the injection moulding conditions on the in-line measured electrical conductivity of polymer–carbon nanotube composites. *Phys. Stat. Sol. (b)* 2008, 245,10, 2268–2271.

216. Enomoto K, Yasuhara T, Ohtake N, Kato K. Injection molding of polystyrene matrix composites filled with vapor grown carbon fiber. *JSME Int J Ser A* 2003,46(3),353–8.

217. Du FM, Fischer JE, Winey KI. Effect of nanotube alignment on percolation conductivity in carbon nanotube/polymer composites. *Phys Rev B* 2005, 72(12),121404

218. Kharchenko SB, Douglas JF, Obrzut J, Grulke EA, Migler KB. Flow-induced properties of nanotube-filled polymer materials. *Nature Mater* 2004;3(8), 564–8.

219. Weber M, Kamal MR. Estimation of the Volume Resistivity of Electrically Conductive Composites *Polymer Compos* 1997,18(6), 711–25.

220. Mahmoodi M, Arjmand M, Sundararaj U, Park S. The electrical conductivity and electromagnetic interference shielding of injection molded multi-walled carbon nanotube/polystyrene composites, *Carbon* 2012, 50, 1455-1464.

221. Behnam A, Guo J, Ural A. Effects of nanotube alignment and measurement direction on percolation in single-wall carbon nanotube films. *J Appl Phys* 2007, 102(4), 44313, 1–7.

222. Krause B, Mende M, Pötschke P, Petzold G. Dispersability and particle size distribution of CNT in an aqueous surfactant dispersion as a function of ultrasonic treatment time. *Carbon* 2010, 48, 2746–2754

223. Socher R, Krause B, Boldt R, Hermasch S, Wursche R, Pötschke P. Melt mixed nano composites of PA12 with MWNT: Influence of MWNT and matrix properties on macrodispersion and electrical properties. *Comp Sci Tech* 2011, 71(3), 306-14

224. Krause B, Petzold G, Pegel S, Pötschke P. Correlation of carbon nanotube dispersability in aqueous surfactant solutions and polymers. *Carbon* 2009, 47, 602–612.

225. Kasaliwal G, Villmow T, Pegel S, Pötsche P. In: McNally T, Pötschke P (ed) Polymer-carbon nanotube composites: preparation, properties and applications. Oxford, WP, Woodhead Publ.; 2011, 92-132.

226. Carponcin D, Dantras E, Aridon G, Levallois F, Cadiergues L, Lacabanne C. Evolution of dispersion of carbon nanotubes in Polyamide 11 matrix composites as determined by DC conductivity. *Compos Sci Technol* 2012, 72, 515–520.

227. Gorrasi G, Bredeau S, Candia CD, Patimo G, Pasquale S, Dubois P. Electroconductive Polyamide 6/MWNT Nanocomposites: Effect of Nanotube Surface-Coating by in situ Catalyzed Polymerization. *Macromol. Mater. Eng.* 2011, 296, 408–413.

228. Brosse AC, Tencé-Girault S, Piccione PM, Leibler L. Effect of multi-walled carbon nanotubes on the lamellae morphology of polyamide 6. *Polymer* 2008, 49(21), 4680–6.

229. Deng H, Skipa T, Zhang R, Lellinger D, Bilotti E, Alig I, Peijs T. Effect of melting and crystallization on the conductive network in conductive polymer composites. *Polymer* 2009, 50, 3747–3754.

230. Tjong SC, Liang GD, Bao SP. Effects of Crystallization on Dispersion of Carbon Nanofibers and Electrical Properties of Polymer Nanocomposites. *Polym Eng Sci* 2008, 48, 177-183

231. Jeon K, Warnock S, Ruiz-Orta C, Kismarahardja A, Brooks J, Alamo RG. Role of Matrix Crystallinity in Carbon Nanotube Dispersion and Electrical Conductivity of iPP-Based Nanocomposites. *J Polym Sci: Part B: Polym Phys* 2010, 48, 2084–2096.

232. Gao J, Itkis ME, Yu A, Bekyarova E, Zhao B, Haddon RC. Continuous spinning of a single-walled carbon nanotube-nylon composite fiber. *J Am Chem Soc* 2005,127, 3847–54.

233. Logakis E, Pandis C, Peoglos V, Pissis P, Stergiou C, Pionteck J, Pötschke P, Mičušík M, Omastová M. Sucture–Property Relationships in Polyamide6/Multi-Walled Carbon Nanotubes Nanocomposites, *J Polym Sci: Part B: Polym Phy* 2009, 47, 764–774.

234. Li J, Fang Z, Tong L, Gu A, Liu F. Polymorphism of Nylon-6 in Multiwalled Carbon Nanotubes/Nylon-6 Composites, J. Polym. Sci., Part B: Polym. Phys. 2006, 44, 1499–1512.

235. Heer WA. Recent developments in carbon nanotubes. *Curr. Opin. Solid Std. Mater. Sci.* 1999, 4, 355–359.

236. Hafner JH, Cheung CL, Woolley AT, Lieber CM. Structural and functional imaging with carbon nanotube AFM probes. *Prog. Biophys. Mol. Bio*. 2001, 77, 73–110.

237. Mamalis AG, Vogtländer LOG, Markopoulos A. Nanotechnology and nanostructured materials: trends in carbon nanotubes. *Precis. Eng*. 2004, 28, 16–30.

238. Trojanowicz, M. Analytical applications of carbon nanotubes: a review. *Trends Anal. Chem*. 2006, 25, 480-489.

239. Lin Y, Zhou B, Fernando KAS, Liu P, Allard LF, Sun YP. Polymeric carbon nanocomposites from carbon nanotubes functionalized with matrix polymer. *Macromolecules* 2003, 36, 7199-7204.

240. Brunetti FG, Herrero MA, Munoz JM, Diaz-Ortiz A, Alfonso J, Meneghetti M, Prato M, Vazquez E. Microwave-induced multiple functionalization of carbon nanotubes. *J. Am. Chem. Soc*. 2008, 130, 8094-8100.

241. Vázquez E, Prato M. Carbon nanotubes and microwaves: Interactions, responses, and applications. *ACS Nano* 2009, 3, 3819-3824

242. Shirley DA. High-Resolution X-ray Photoemission Spectrum of the Valence Bands of Gold. *Phys. Rev. B* 1972, B5, 4709–4714.

243. Lægsgaard E, Österlund L, Thostrup P, Rosmussen PB, Stensgaard I, Besenbacher FA. High-Pressure Scanning Tunneling Microscope. *Rev. Sci. Instrum.* 2001, 72, 3537–3542.

244. Paiva MC, Xu W, Proença MF, Novais RM, Lægsgaard E, Besenbacher F. Unzipping of Functionalized Multiwall Carbon Nanotubes Induced by STM. *Nano Lett.* 2010, 10, 1764–1768.
245. Hahn M, Pleul D, Nitschke M, Frens G, Bundel G, Prause S, Simon F. Plasma modification of diamond surfaces. *J. Adhes. Sci. Technol*. 2005, 19, 1039-1052.
246. Beamson G, Briggs D. High resolution of organic polymers. In The Scienta ESCA 300 Database, J. Wiley & Sons, Chichester, New York, Brisbane, Toronto, Singapore, 1992; appendix 4.
247. Zhao J, Mayes RH, Chen G, Xie H, Chan PS. Effects of process parameters on the micro molding process. *Polym. Eng. Sci.* 2003, 43, 1542.
248. Viana JC. Development of the skin layer in injection moulding: phenomenological model. *Polymer* 2004, 45, 993–1005
249. Kumaraswamy G. Crystallization of polymers from stressed melts. *Polym. Rev.* 2005, 45, 375–397.
250. Tadmor Z, Gogos CG. Principles of polymer processing. New York: Wiley; 2006, 2nd edition.
251. Lu Z, Zhang KF. Crystal distribution and molecule orientation of micro injection molded polypropylene microstructured parts. *Polym. Eng. Sci.* 2009, 49 (8), 1661–1665.
252. Ito H, Kazama K, Kikutani T. Effects of Process Conditions on Surface Replication and Higher-Order Structure Formation in Micromolding. *Macromol. Symp*. 2007, 628–634.
253. Healy J, Edward G H and Knott R B. Residual orientation in injection micro-molded samples *Physica* B. 2006, 385–386, 620–2.
254. Meister S, Drummer D. Influence of manufacturing conditions on measurement of mechanical material properties on thermoplastic micro tensile bars. *Polym Test* 32 (2013) 432–437.
255. Lin X, Caton-Rose F, Ren D, Wang K. Coates, Shear-induced crystallization morphology and mechanical property of high density polyethylene in micro-injection molding. *J Polym Res* 2013, 20, 122.
256. Ito M, Mizuochi K, Kanamoto T. Effects of crystalline forms on the deformation behaviour of nylon-6. *Polymer*, 1998, 39, 4593–4598.
257. Phang IY, Ma J, Shen L, Liu T, Zhang WD. Crystallization and melting behavior of multi-walled carbon nanotube-reinforced nylon-6 composites. *Polym Int* 2006, 55:71–79.
258. Fornes TD, Paul DR. Crystallization behavior of nylon 6 nanocomposites, Polymer 2003, 44, 3945–3961.
259. X ray data analysis software manual. Stonybrook Technology and Applied Research, Inc, NY, USA, v 1.04.

260. Jungmeier A, Ehrenstein GW, Drummer D. New aspects of process induced properties of microinjection moulded parts. *Plast. Rubber Compos. Process. Appl*. 2010, 39, 7, 308-314.

261. S. T. Correale, N. S. Murthy. Secondary Crystallization and Premelting Endo- and Exotherms in Oriented Polymers. *J. Appl. Polym. Sci*. 2006, 101, 447–454.

262. Xie S, Séguéla R, Lefebvre JM, Gloaguen JM. A Re-Examination of the Sub-Tm Exotherm in Polyamide 6:The Roles of Thermal History, Water and Clay. *J Polym Sci Part B: Polym Phy* 2009, 47, 2385–2393.

263. Mehta RH. Physical Constants of Various Polyamides, J. Brandrup, E. H. Immergut and E. A. Grulke, Polymer Handbook, fourth edition, 1998.

264. Li J, Fang Z, Tong L, Gu A, Liu F. Polymorphism of Nylon-6 in Multiwalled Carbon Nanotubes/Nylon-6 Composites, *J Polym Sci Part B: Polym Phy* 2006, 44, 1499–1512.

265. Cavallo D, Gardella L, Alfonso GC, Portale G, Balzano L, Androsch R. Effect of cooling rate on the crystal/mesophase polymorphism of polyamide 6*. Colloid Polym Sci* 2011, 289:1073–1079.

266. Alexander LE. X ray Diffraction Methods in Polymer Science. Wiley-Interscience. New York, 1969.

267. Paradise M, Goswami T. Carbon nanotubes – Production and industrial applications. *Mater. Des.* 2007, 28, 1477–1489.

268. Murthy NS. Hydrogen bonding, mobility, and structural transitions in aliphatic polyamides *J Polym Sci Part B: Polym Phy* 2006, 44 13, 1763–1782.

269. Lincoln DM, Vaia RA, Wang ZG, Hsiao BS. Secondary structure and elevated temperature crystallite morphology of nylon-6/layered silicate nanocomposites. *Polymer* 2001, 42, 1621.

270. Ha H, Kim SC. Morphology and Properties of polyamide/Multi-walled Carbon Nanotube Composites, *Macromolecular Research* 2010, 18, 7,660-667.

271. Coleman JN, Cadek M, Ryan KP, Fonseca A, Nagy JB, Blau WJ, Ferreira MS. Reinforcement of polymers with carbon nanotubes. The role of an ordered polymer interfacial region. Experiment and modeling. *Polymer* 2006, 47, 8556–8561.

272. Li J, Ke C, Fang K, Fan X, Guo Z, Fang Z. Crystallization and Rheological Behaviors of Amino-functionalized Multiwalled Carbon Nanotubes Filled Polyamide 6 Composites. *J. Macromol. Sci. Part B: Phy*, 2010, 49, 405–418.

273. Meng H, Sui GX, Fang PF, Yang R. Effects of acid- and diamine-modified MWNTs on the mechanical properties and crystallization behavior of polyamide 6. *Polymer* 2008, 49, 610.

274. Zhang J, Zhang L, Liu H, Liu F, Guo C. Study of Micro-Injection Moulding: Factors Affecting the Content of the β-phase in Isotactic Polypropylene with β-nucleating Agent. *Polym. Plast. Technol. Eng*. 2012, 51, 1032–1037.

275. Ferreira T, Lopes PEC, Pontes AJ, Paiva MC. Microinjection Moulding of Polyamide 6 - submitted to *J. Appl. Polym. Sci.*

276. Ferreira T, Paiva MC, Pontes A, Dispersion Of Carbon Nanotubes In Polyamide 6 For Microinjection Moulding, *J Polym Res* 2013, 20, 301.

277. Paiva M, Simon F, Novais R, Ferreira T, Proença M, Xu W, Besenbacher F. *ACS Nano* 2010, 4 (12), 7379-7386.

278. Zhang S, Minu, LM, Zhu L, Wong CP, Kumar S. Polymer transcrystallinity induced by carbon nanotubes. *Polymer* 2008, 49, 1356–1364.

279. Qian D, Dickey EC, Andrews R, Rantell T. Load Transfer and deformation mechanisms in carbon nanotube polystyrene composites. *Appl Phys Lett* 2000, 76, (20): 2868-70.

280. Yoo HJ, Jung YC, Sahoo NG, Cho JW. Polyurethane-Carbon Nanotube Nanocomposites Prepared by In-Situ Polymerization with Electroactive Shape Memory *J Macromol Sci Part B Phys* 2006, 45, 441–451.

281. Schartel B, Pötschke P, Knoll U, Abdel-Goad M. Fire behaviour of polyamide 6/multiwall carbon nanotube nanocomposites. *Eur. Polym. J.* 2005, 41(5), 1061–70.

282. Pötschke P, Bhattacharyya AR, Janke A, Pegel S, Leonhardt A, Täschner C, Ritschel M, Roth S, Hornbostel B, Cech J. Melt Mixing as Method to Disperse Carbon Nanotubes into Thermoplastic Polymers. *Fullerenes, Nanotubes, and Carbon Nanostructures* 2005, 13, 211–224.

283. Abbasi S, Derdouri A, Carreau PJ. Effect of nanotube alignment on the morphology and properties of polycarbonate/MWCNT nanocomposites. Proceedings of the 8th World Congress of Chemical Engineering, 2009, 2009-08

284. Pontes AJ, Sepúlveda AT, Sampaio M, Cortez J, Cunha AM Proceedings of 24th (2008) annual meeting of the Polymer Processing Society: 2008-06

285. Shen J, Huang W, Wu L, Hu Y, Ye M. The reinforcement role of different amino-functionalized multi-walled carbon nanotubes in epoxy nanocomposites Compos. Sci. Technol. 2007, 67, 3041–3050.